GPU ACCELERATED LATTICE BOLTZMANN ANALYSIS FOR DYNAMICS OF GLOBAL BUBBLE COALESCENCE IN MICROCHANNELS

A Dissertation

Submitted to the Faculty

of

Purdue University

by

Chen Rou

In Partial Fulfillment of the

Requirements for the Degree

of

Doctor of Philosophy

August 2019

Purdue University

West Lafayette, Indiana

THE PURDUE UNIVERSITY GRADUATE SCHOOL
STATEMENT OF COMMITTEE APPROVAL

Dr. Huidan(Whitney) Yu, Co-Chair

Department of Mechanical and Energy Engineering

Dr. Pavlos Vlachos, Co-Chair

School of Mechanical Engineering

Dr. Arezoo M. Ardekani

School of Mechanical Engineering

Dr. Likun Zhu

Department of Mechanical and Energy Engineering

Dr. Luoding Zhu

Department of Mathematical Sciences

Approved by:

Dr. Jie Chen

Head of the Graduate Program

For my parents and friends

ACKNOWLEDGMENTS

First, I would like to express my sincere gratitude to Prof. Huidan (Whitney) Yu, my supervisor and the committee co-chair. She provided the opportunity for me to pursue a Ph.D. and gave supports during my Ph.D. program academically and financially. Many thanks to her for the guidance, encouragement, and insight recommendations through these years. Without her persistent help, this dissertation couldn't be finished.

My sincere thanks also go to my co-chair Prof. Pavlos Vlachos for his suggestions let me be an eligible Ph.D. I also would like to thank my committee members, Prof. Likun Zhu, Prof. Luoding Zhu, and Prof. Arezoon M. Ardekani for taking the time to work with me to fulfill all the requirements of the doctoral program. Prof. Likun Zhu provided helpful discussions and insightful recommendations for my project of Ph.D. Prof. Luoding Zhu offered the computational resource that assists performance test of some cases. Meanwhile, my veneration goes to Prof.Taehun Lee for his help in understanding the methodology applied in my dissertation.

I thank my fellow mates of Computational Fluid Lab: Xi Chen, Senyou An, Monusral Khan, Anurag Deb, Xiaoyu Zhang, Xin Jin, and Yan Gu. They supported me through academic discussions and created a positive and highly motivated working environment.

I also thank Dr. Cynthina Jesudason, Mrs.Choi-hai Huang, and Linda Swigart for their care, advice, and help.

Last but not least, thanks to my parents, for giving me life and endless love.

TABLE OF CONTENTS

Page

Page

LIST OF TABLES

Table Page

LIST OF FIGURES

Figure Page

Figure Page

Figure Page

Figure Page

Figure Page

Figure Page

SYMBOLS

A_0	Prefactor of power-law scaling
c	Lattice velocity in LBM
C	Composition
d	Separation distance
D	Numerical interface thickness
D_x	Distances between the bubble edge and the mass center in the horizontal direction
D_y	Distances between the bubble edge and the mass center in the vertical direction
e_α	Discretized velocity in LBM
E_0	Bulk energy
$\mathbf{F}$	Intermolecular force
f	Particle distribution function
g_α	Particle distribution function which is used to recover momentum and pressure evolution equation
g_α^{eq}	Equilibrium distribution function of g_α
$\bar{g}_\alpha$	Modified particle distribution function of g_α
$\bar{g}_\alpha^{eq}$	Modified equilibrium distribution function of g_α
h_α	Particle distribution function which is used to recover Cahn-Hilliard evolution equation
h_α^{eq}	Equilibrium distribution function of h_α
$\bar{h}_\alpha$	Modified particle distribution function of h_α
$\bar{h}_\alpha^{eq}$	Modified equilibrium distribution function of h_α
$\mathbf{j}$	Volumetric diffusive flux

K_δ	Curvature of meniscus
K_r	Curvature of neck bridge
L	Length
M	Mobility
Oh	Ohnesorge number
p	Total pressure
P	Mechanical pressure pressure
p_0	Thermodynamic pressure
p_1	Dynamic pressure
r	Neck bridge radius
r_0	Initial neck bridge radius
R_0	Bubble radius
r_F	Radius of father bubble
r_M	Radius of mother bubble
t	Time
T	Coalesced time
t_i	Timescale in the inertial regime
t_v	Timescale in the viscous regime
$\boldsymbol{u}$	Velocity of fluid
w_α	Weight in the particle distribution function
$\mathbf{x_f}$	Position of node in the fluid
$\mathbf{x_s}$	Position of node on the boundary
β	Constant in the classical part of the chemical potential
γ	Radius ratio
γ_d	The ratio of separation distance and bubble radius
γ_r	The ratio of initial neck bridge radius and bubble radius
Γ_β	Particle distribution function
δ	Diameter of meniscus
δt	Lattice time unit

δx	Lattice length unit
Δx	Shape factor
κ	Gradient parameter
μ	Local dynamic viscosity
μ_c	Chemical potential
μ_{c0}	Classical part of the chemical potential
ν	Local kinematic viscosity
ξ	Molecular velocity
ρ	Local density
σ	Surface tension
τ	Non-dimensional relaxation time
ϕ	Macroscopic variables
χ	Relative distance ratio
Ψ	Free surface energy
∇^{CD}	Central difference approximation
∇^{MD}	Mixed difference approximation

Subscript

g	Parameters with lattice unit
h	Heavy fluid
l	Light fluid
p	Characteristic variables

Supscript

$*$	Normalized variables

ABBREVIATIONS

AoS	Array of Structures
API	Application Programming Interface
CFD	Computational Fluid Dynamic
CIMD	Coalescence Induced Microbubble Detachment
CSoA	Collected SoA
DF	Distribution Function
FE	Free Energy
FSI	Fluid-Structure Interaction
GPU	Graphic processing unit
LBM	Lattice Boltzmann Method
MLUPS	Million Lattice Updates Per Second
MPI	Message Passing Interface
SoA	Structure of Array
SC	Shan–Chen

ABSTRACT

Rou, Chen Ph.D., Purdue University, August 2019. GPU accelerated lattice Boltzmann analysis for dynamics of global bubble coalescence in microchannels. Major Professor: Huidan(Whitney) Yu and Pavlos Vlachos.

Underlying physics in bubble coalescence is critical for understanding bubble transportation. It is one of the major mechanisms of microfluidics. Understanding the mechanism has benefits in the design, development, and optimization of microfluidics for various applications. The underlying physics in bubble coalescence is investigated numerically using the free energy-based lattice Boltzmann method by massive parametrization and classification.

Firstly, comprehensive GPU (Graphics Processing Unit) parallelization, convergence check, and validation are carried out to ensure the computational efficiency and physical accuracy for the numerical simulations.

Then, the liquid-gas system is characterized by an Ohnesorge number $Oh \equiv (\mu_h/\sqrt{\rho_h \sigma r_F})$. Two distinct coalescence phenomena with and without oscillation, are separated by a critical $Oh(\approx 0.477)$ number. For the oscillation cases($Oh < 0.477$), the mechanism of damped oscillation in microbubble coalescence is explored in terms of the competition between driving and resisting forces. Through an analogy to the conventional damped harmonic oscillator, the saddle-point trajectory over the entire oscillation can be well predicted analytically. Without oscillation in the range of $0.5 < Oh < 1.0$, we derive and validate a general temporal power-law scaling correlating the normalized global coalescence time (T^*) from initial to steady state, versus size inequality γ, the radius ratio of two initial parent bubbles $T^* = A_0 \gamma^{-n}$.

After that, the liquid-gas-solid interface is taken into consideration in the liquid-gas system. Six cases based on the experiment set-ups are simulated first for validation of the

computational results. Based on these, a hypothesis is established about critical factors to determine if coalescence-induced microbubble detachment (CIMD) will occur. From the eighteen experimental and computational cases, we conclude that when the radius ratio is close to 1 and the father bubble is larger, then it will lead to CIMD.

Lastly, the effects of initial conditions on the coalescence of two equal-sized air microbubbles (R_0) in water are investigated. In both initial scenarios, the neck bridge evolution exhibits a half power-law scaling, $r/R_0 = A_0(t/t_i)^{1/2}$ after development time. The development time is caused by the significant bias between the capillary forces contributed by the meniscus curvature and the neck bridge curvature. Meanwhile, the physical mechanism behind each behavior has been explored.

1. INTRODUCTION

Microfluidic systems, with dimensions ranging from tens to hundreds of micrometers [1], attract increasing attention in a myriad of applications [2] in advanced clinical procedures [3, 4], biology [5, 6], and chemistry [7, 8]. Typically in microfluidic systems fluids are manipulated to transport [9], mix [10, 11], and separate [12, 13]. Microfluidic systems also enable the manipulation of living matter at microscales [14, 15]. Over the last decade, there has been a significant process towards the development of control and detection of chemical and biological reactions in microfluidic systems [16]. Unique features of microfluidic systems include small quantities of sample, low cost, reduced exposure of dangerous substances, and short time analysis thus they are useful in Point-of-care Testing [17], DNA analysis [18, 19], and cell separation [20, 21]. In industry, the common applications of microfluidic systems are ink-jet print-heads [22], micro-propulsion [23], hydrogenation [24, 25] and electrochemical cells including solar water splitting cells [26–28] and microbial electrolysis cells [29–31]. Controlling bubble transportation, including size and motion of air bubbles, can impact the behavior of flow within microfluidic systems [32].

Bubble coalescence is one of the fundamental phenomena in the microfluidic systems. It is the process during which two or more parent bubbles, with their diameters from $1\mu m - 1mm$, merge toward a single child bubble until a minimal surface area is reached. For the purpose of controlling gas/liquid dynamics, the coalescence in some systems needs to be prevented or suppressed to maintain a stable mixing condition between the gas and liquid phase. For example, mass transfer processes in a rising bubble, bubble columns [33], gas-liquid contactor [34], avoiding clogging in the microchannel [35], etc., whereas in other systems, efficient coalescence might be desirable to enhance the phase separation process [36]. Therefore, it is important to study the dynamics of microbubble coalescence under various influences and understand its underlying physics for effective control of gas-liquid systems.

1.1 Literature Review

1.1.1 Microbubble coalescence dynamics

From two parent bubbles separated with a short distance, i.e., $10^{-6} - 10^{-5}m$, to eventually a single coalesced child bubble, a bubble coalescence mainly consists of the following five phenomena:

- **Bubble collision** Generally speaking, coalescence is the consequence of bubble–bubble collision [37,38], which can be caused by a variety of mechanisms comprising turbulence, eddy capture, velocity gradient in the mean flow, body forces and wake entrainment. When a bubble is placed in a flowing liquid, it will experience destroying stress, which acts to deform and break it. On the other hand, a restoring force provided by surface tension will prescribe a critical value that is required for a break-up event to occur. Once the destroying stress exceeds the critical one, the bubble will break up [39]. Otherwise, bubble collision traps a small amount of liquid between them. This liquid then drains until the liquid film separating the bubbles reaches a critical thickness. This behavior corresponds to Figure 1.1(a).

- **Liquid film thinning and rupture** When two parent bubbles are apart within a short distance, i.e., $10 - 200nm$ [40], the intermolecular force of the gas molecules will attract them to approach, causing the liquid film thinning. A tangible touch of two bubbles are rather unstable, and a small perturbation would cause a rupture of the liquid film, see Figure 1.1(b)

- **Growth of neck bridge** When the liquid film is ruptured, the earliest neck bridge is formed, and the merging of the two bubbles starts. The neck bridge growth is governed by both resisting force (inertial force and viscous force) and driving force (capillarity force) characterized by Ohnesorge number (viscous force versus inertial and capillarity forces). $Oh(\equiv \mu_h/\sqrt{\rho_h \sigma L})$ where L, μ, ρ, σ are the characteristic length, e.g. droplet/bubble radius R_0, viscosity, density, and surface tension respectively. The subscript h means the heavier fluid. This stage is shown in Figure 1.1(c)

- **Shape oscillation** Depending on the physical properties of the fluids and composition of the interface, the coalescing bubble may exhibit shape oscillation shifting the major/minor axis between horizontal and vertical directions. As seen in Figure 1.1(d), this oscillation is damping. It has been found that correspond to different Oh number, the shape oscillation can be under damping, over damping (literally meaning no oscillation), and critical damping.

- **Single coalesced bubble** The neck bridges grow rapidly toward a single coalesced bubble until the surface area is minimized (Figure 1.1(e)).

These five phenomena can be characterized as three stages in terms of the coalescence process: pre-coalescence (collision and liquid film thinning and rupture), early stage (growth of neck bridge), post-coalescence (toward a child bubble with a minimal surface area with or without shape oscillation).

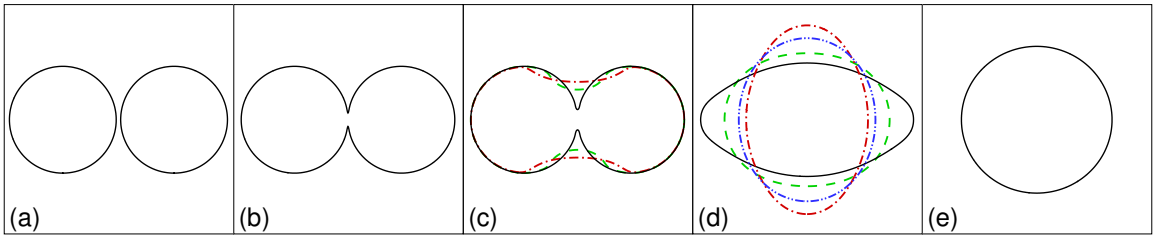

Figure 1.1: Five phenomena of microbubble coalescence: (a) bubble collision, (b) liquid film thinning and rupture, (c) growth of neck bridge (d) shape oscillation, and (e) single coalesced bubble.

There have been considerable efforts to explore the dynamics of pre-coalescence of bubble coalescence and good understanding has been achieved. Many studies were on various factors affecting the coalescence time through experiments, simulations, and the combination of both. Experimental studies [41–43] focused on the coalescence of multiple bubbles aiming to determine bubble size distribution, gas holdup, interfacial area, and bubble rise velocity in different solutes and electrolytes in order to control the formation and performance of bubbles in bubble columns and the distillation tower. For example, it has been found that the coalescence time, defined as the approaching time of two bubbles from a

distance of $10^{-6} - 10^{-5}m$ to a contact, increases with solute concentration and/or surface tension gradient [44, 45].

For the early stage of bubble coalescence, recent efforts have focused on the formation and growth of neck bridge via numerical, experimental, and theoretical studies. It has been found that when viscous effect is negligible (i.e., $Oh \ll 1$), the coalescence of two identical droplets with radius R_0 is dominated by inertial force with a coalescence timescale $t_i = \sqrt{\rho_h R_0^3/\sigma}$ (i.e., in the inertial regime) [46]. In this regime, it has been analytically [47, 48], experimentally, [49, 50] and numerically [51–53] found that the time evolution of the neck bridge radius r follows a power-law, $r/R_0 \propto (t/t_i)^{1/2}$. On the other hand, when the viscous effect becomes significant (i.e., $Oh > 1$), the coalescence timescale is characterized by $t_v = \mu R_0/\sigma$ (i.e., in the viscous regime). Neck bridge evolution is found $r/R_0 \propto t/t_v ln(t/t_v)$ [47]. Paulsen, *et al* [54] analytically predicted that the neck bridge evolution of bubble coalescence follow the same half power-law scaling, i.e., $r/R_0 \propto (t/t_c)^{1/2}$, in the inertial and viscous regimes where the characteristic time t_c corresponds to t_i and t_v respectively. This prediction was confirmed by their experiment results as well. Meanwhile, they sophisticatedly studied the effect of dense surrounding fluid on the coalescence of bubbles based on the formation of an infinitesimal neck bridge. They discovered that outer fluid has a marginal effect on coalescence dynamics. A phase diagram was developed, suggesting that the viscosity of the outer fluid may significantly affect the coalescence dynamics.

For the post-coalescence, a few attempts were made on the phenomenon called damped oscillation, switching the major axis of the coalescing bubble between horizontal and vertical direction with reducing the amplitude of the major/minor axis ratio. The majority of studies were on forced oscillation, specifically induced by various external sources such as electrostatic force [55], acoustic trap [56], and laser light [57] for the purpose of controlling bubble size and collapse in different engineering and biomedical systems [58, 59]. Whereas self-oscillation, driven by imbalance between the driven and resistant forces, has been rarely addressed. In the self-oscillation, the driving is from the surface tension at the gas-liquid interface and the resistance is co-contributed by inertial and viscous effects in

the liquid side. Understanding the mechanism of self-oscillation [60, 61] is critically important in the design and development of forced oscillation required in many real-world applications. Rayleigh [62] was the pioneer to study small-amplitude self-oscillation of an inviscid droplet from a pure mathematical point of view in 1879. Since then, Rayleigh's work has been extended toward physical environments by exploring the density effects of the surrounding fluid [63], the viscous effects [64], and the initial condition effects [65] on the oscillation. A relationship between Ohnesorge number (Oh, a dimensionless number that relates the viscous forces to inertial and surface tension forces) and critical damping (corresponding to the shortest coalescence time) for a droplet, i.e., $0.71 < Oh < 0.76$ was found [66] in the early 1990s.

In the literature, most of the research focused on the individual stages of coalescence. The global process of coalescence from the touch of two parent bubbles to a single child bubble with minimal area surface has not focused. Important attempts through experimental [67, 68] and radiological measurements [69] have been on the fundamentals of coalescence dynamics associated with hydrodynamics and mass transport for the global process of bubble coalescence, including the spatial scales. For the puzzling tendency of the coalesced child bubble to be preferentially located closer to the larger of its two parent bubbles, named coalescence preference, was observed in experimentation [69, 70]. It has been found that the location of the merged bubble is linked by the parent bubble size ratio with a power-law relationship. Stover *et. al* [71] were the first to experimentally study the microbubble oscillation and showed the effects of liquid viscosity and surface tension on the decay of the damped oscillation. Recently, a benchmark study [72] showed the different morphological evolution in the global coalescence from two equal-sized spherical droplets to a stable single droplet with minimal surface energy when the viscosity ratio of two-fluids is either low or high.

In this dissertation, we investigation bubble coalescence in the microchannel, focusing on the global process, corresponding to Figure 1.1(c) to (e). Due to the delicate and ephemeral nature of microbubble coalescence, experimental exploration of the coalescence mechanism is exceptionally challenging whereas numerical simulation provides a unique

and powerful alternative for parameterization to reveal fundamental physics of bubble coalescence with physical and computational advantages. It makes investigating possible in the spatial and temporal characteristics of microbubble coalescence, which has not been understood.

1.1.2 Lattice Boltzmann method for multiphase flows

Historically, lattice Boltzmann Method (LBM) was originated from lattice gas automata (LGA) [73, 74]. The LGA is a simple computation model, in which space, time, and particle velocities are all discrete, for simulating fluid flows. Later it was rigorously proved that the LBM is closely associated with Boltzmann equation. After an approximation of the collision operator such as BGK model [75], the formulation of LBM can be derived through a coherent discretization of the molecular phase space and time from the Boltzmann equation [76, 77]. In LBM, microscopic fluid physics is simplified to retain only the essential elements (the local conservation laws and related symmetries) needed to guarantee accurate macroscopic behavior. Same as the Boltzmann equation, the LBM recovers NS equation in the limit of continuum flow regime [78].

The LBM is based on kinetic theory sometimes termed mesoscopic CFD. It was developed rapidly in the past decades and is widely used as a powerful numerical tool for solving various complex flow systems [79, 80]. The LBM is second-order accurate in time and space and has advantages of good parallel performance, distinct physical image, simple programming, and easy handling of complex geometries. The most attractive advantages of the LBM for this research are its amenability for modeling the intermolecular interactions at the two-phase interface without demanding computation cost for recovering the appropriate multi-phase dynamics and the suitability for scalable GPU (Graphic Processing Unit) parallelization.

In the past three decades, several multi-phase models using LBM have been developed, including the color fluid model [81], the pseudo-potential model [82, 83], the mean-field model *et al.* [84, 85], the phase-field model [86, 87], and the entropic LBM [88]. These

methods have been continuously refined and applied to simulate many multiphase flow problems, see both general LBM reviews [79, 80] and specific multi-phase LBM reviews [89, 90], and therein references. In spite of efforts and successful applications in various flow systems, simulation of multiphase flows with large density and viscosity ratios between two fluids, as the current application targets.

When a multiphase flow involves large density ratio of liquid vs. gas, as well as the solid-liquid-gas interface, is also developing in recent years. The major challenge is to overcome the numerical instability due to the occurrence of parasitic current, a small-amplitude artificial/nonphysical velocity field arising from an imbalance of discretized forces across the interface. In general, to pursue low parasitic current, either the accuracy of the contact angle in a certain region or the density ratio between two fluids have to be compromised. For examples, insufficient accuracy at small, medium, and large contact angles have been reported when the pseudo-potential model [91–93], the color fluid model [94], and the free-energy-based model [95,96] were employed respectively. The interface tracking model can cover the full range of the contact angle but is limited to a low-density ratio of two fluids [97, 98]. Detail discussions about these models are referred to Huang's book [99]. To overcome the drawbacks, the Lee group integrated the interface tracking and free energy models with the cubic polynomial boundary conditions [100]. This approach has been continuously developed and refined in the last 10 years [101–104], and it has been demonstrated that this approach has eliminated the parasitic current without a compromise of inaccurate contact angle [100, 104], which well fits the need of the current study.

1.1.3 GPU parallelization for Lattice Boltzmann method

The GPU acceleration for LBM has a short history but it develops rapidly due to the increasing demands from computation of complex flows, especially when complex geometry, multi-scale, multiphase, and massive parametric study are involved. The first work applying GPU acceleration for LBM [105] was in 2003. Li *et al* performed computations, in which textures and render buffers were used. Based on this approach, Zhu *et al* devel-

oped GPU parallelism for two miscible fluids system and achieved speed three times faster than serial CPU executions. In 2006, a parallel computing platform and application programming interface (API) model created by NVIDIA [106] called CUDA was launched. The first parallel implementation of D3Q19 on CUDA was done in 2008 [107], a sequential code (470.lbm) parallelized from the SPEC CPU2006 [108] on CUDA . After that, the GPU acceleration for LBM in the stage of general purpose GPU (GPGPU) implementations and optimization with CUDA. Optimization of GPU acceleration for LBM has been developed in three aspects: memory access patterns, register utilization, and overlap of memory transfer and arithmetic operations.

Memory access pattern attracts the most attention in the literature through propagation schemes, data layout, and memory addressing. *Propagation schemes:* GPU parallelization of LBM mainly consists of two parts in each iteration: collision and streaming. Since the collision occurs at the local nodes but steaming requires information from neighbouring nodes, the efforts on the fast access to the memory have been on the development of propagation schemes [109] for the streaming part. Shift algorithm with shared memory [110, 111] was applied at the beginning to avoid misaligned accessing at the expense of adding an extra kernel to exchange data through GeForce 8800 Ultra. The propagation scheme of the A-A pattern (only one set of distribution functions (DFs) in memory) based on the shift algorithm with shared memory was developed [112] in 2009. The A-A pattern reduced GPU memory by 50% comparing with the A–B pattern (two sets of DFs in memory). Shortly after, split propagation scheme (misaligned write), and reversed propagation (pull) scheme (misaligned read) [113] were developed which have a 15% improvement compared with a shared memory scheme with the GTX 295. *Data layout*: Two popular schemes of data layout include array of structure (AoS) and structure of array (SoA). SoA switches from AoS for the optimization of GPU parallelism [107]. It has 7-10 times speed increasing with Tesla Kepler K20 [114]. Herschlag *et al* [115] applied more complex data layouts, i.e., collected SoA in the GPU architectures and accelerated computational speed by 5-20% compared with SoA layout. *Memory addressing*: Indirect addressing and semi-addressing are two

common patterns of memory addressing that are original approach for CPUs. Compared with direct address [115], they have 4-5 times acceleration for complex geometry problems.

Two other aspects are much less addressed. Accessing register memory consumes zero clock cycles per instruction comparing to 400-600 cycles for global memory. Whereas, the amount of register is limited. An NVIDIA compiler provides a flag to limit the register usages for register utilization [116]. Meanwhile, there are two strategies for overlap of memory transfer and arithmetic operations including tiling the 3D lattice grid into smaller 3D blocks and branch divergence removal [114].

In the case of multiphase flows, similar approaches of optimization are applied in different models. As reviewed [117]. the performance of LEE model [118], SC model [119], and FE model [119] are 125.1, 210, 238 (MLUPS) respectively with C2050 GPU cards in the float precision, where million lattice update per seconds (MLUPS) indicates the performance of lattice Boltzmann simulations. If one uses double precision, the MLUPS will be decreased about two times. Meanwhile, GPU hardware has been developed quickly. For example, MLUPSs have increased 1.3 times with Tesla Kepler K20 and 1.7 times with Tesla Kepler K40 respectively comparing with C2050 [119]. In the LEE model, Tesla P100 accelerated 10 and 680 times compared with Tesla M2070, serial CPU(i7-4930K) respectively [120].

Development of the paralleization combined with GPU, CPU, and network is popular in recent years to solve multi-scale, multi-physics research problems. The paralleization include multi-GPU [121, 122], LBM code with CUDA and OpenMP (API that supports multi-platform shared memory multiprocessing programming, i.e., CPU parallelism) for multi-GPU clusters [123], LBM with CUDA and MPI (a standard API for message passing through networks/multi-node computer clusters) [124], and a multi-node MPI/OpenMP LBM code with OpenACC (a programming standard that can simplify parallel programming of heterogeneous CPU/GPU systems) [125].

1.2 Research Objective

The objective of this dissertation is twofold :

- Unveil underlying physics of microbubble coalescence via massive parametrization and classification.

  1) To explore fundamental mechanisms of various phenomena global microbubble coalescence.

  2) To gain physical insights of various effects on the dynamics of global coalescence.

- Enhance computational skills through the realization of physically reliable and computationally efficient lattice Boltzmann simulations for multiphase flows with large density/viscosity ratio, focusing on GPU parallelization and optimization.

1.3 Outline of dissertation

The remainder of the dissertation is organized as follows: The methodology includes the LBM, the LBM model for multiphase flows, and its GPU parallelization that is presented in Chapter 2 and Chapter 3 respectively. The numerical results are presented in Chapters 4 through 6 for temporal/spatial behaviors of bubble coalescence, coalescence-induced detachment, and initial condition effects on the bubble coalescence respectively. Summary and future work are expressed in Chapters 7 and 8, respectively.

2. LATTICE BOLTZMANN METHOD FOR MULTIPHASE FLOWS

2.1 General description of lattice Boltzmann method

The lattice BGK model is the most widely used lattice Boltzmann models to date which can be obtained as

$$f(\mathbf{x_g} + \mathbf{e}_\alpha \Delta t, \mathbf{e}_\alpha, t_g + \Delta t) - f(\mathbf{x_g}, \mathbf{e}_\alpha, t_g) = -\frac{1}{\tau_0}(f(\mathbf{x_g}, \mathbf{e}_\alpha, t_g) - f^{eq}(\mathbf{x_g}, \mathbf{e}_\alpha, t_g)) \quad (2.1)$$

Among the LBGK models, the representative DnQb lattice model developed by Qian is the most popular, which denotes n dimensions and b lattice velocities. In DnQb lattice model, the equilibrium distribution function is shown as

$$f_\alpha^{eq} = w_\alpha \rho[1 + \frac{(\mathbf{e}_\alpha \cdot \mathbf{u})}{c_s^2} + \frac{(\mathbf{e}_\alpha \cdot \mathbf{u})^2}{2c_s^4} - \frac{u^2}{2c_s^2}] \quad (2.2)$$

where ω_α is the weight associated with a particular discretized velocity $\mathbf{e}_\alpha$, ρ and $\mathbf{u}$ are macroscopic density and velocity respectively, $c_s^2 = \sqrt{RT}$ is related to speed of sound, and $c = \delta x/\delta t = 1$ in lattice units (i.e., $\delta t = \delta x = 1$). Pressure $P_g = c_s^2 \rho_g$. There are several DnQb lattice models in common use listed as Figure 2.1 with discrete velocity distribution and weight coefficient.

2.1.1 The relationship between computational flow field based on LBM and physical flow field

The flow motion in practical engineering problems is complex in general. And numerical simulation is necessary to be applied when studying these problems. However, due to the computational cost and limitations, the size of the numerical model is generally different from the actual size. In order to compare the results of simulation with physics, the physical quantities need to be dimensionless according to the similarity criterion. In the similarity

D1Q3

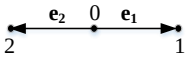

$\mathbf{e}_\alpha$ =c{0, 1, -1}

ω_α={2/3, 1/6, 1/6}

c_s=1/$\sqrt{3}$c

D1Q5

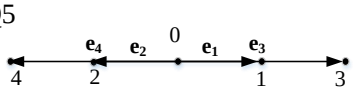

$\mathbf{e}_\alpha$ =c{0, 1, -1, 2, -2}

ω_α={1/2, 1/6, 1/6, 1/2, 1/2}

c_s=c

D2Q7

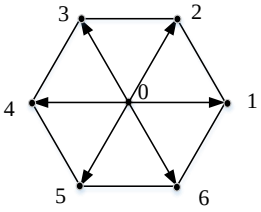

$\mathbf{e}_\alpha$ =c{(0, 0), (1, 0), (1/2, $\sqrt{3}$/2), (-1/2, $\sqrt{3}$/2), (1, 0), (1/2, $\sqrt{3}$/2), (-1/2,$\sqrt{3}$/2)}

ω_0=1/2, ω_α=1/12(α=1-6)

c_s=2c

D2Q9

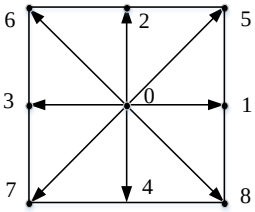

$\mathbf{e}_\alpha$ =c{(0, 0), (1, 0), (0, 1), (-1, 0), (0, -1), (1, 1), (-1, 1), (-1, -1), (1, -1)}

ω_0=4/9, ω_α=1/9(α=1-4), 1/36(α=5-8)

c_s=1/$\sqrt{3}$c

D3Q19

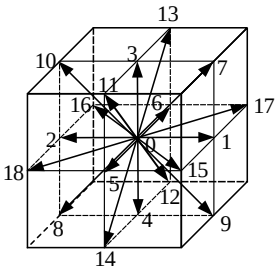

$\mathbf{e}_\alpha$ =c{(0, 0, 0), ±(1, 0, 0), ±(0, 1, 0), ±(0, 0, 1), ±(1, 1, 0), ±(1, -1, 0), ±(1, 0, 1), ±(1, 0, -1), ±(0, 1, 1), ±(0, 1, -1)}

ω_0=1/3, ω_α=1/18(α=1-6), 1/36(α=7-18)

c_s=1/$\sqrt{3}$c

D3Q27

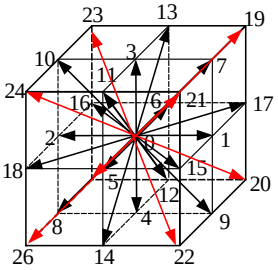

$\mathbf{e}_\alpha$ =c{(0, 0, 0), ±(1, 0, 0), ±(0, 1, 0), ±(0, 0, 1), ±(1, 1, 0), ±(1, -1, 0), ±(1, 0, 1), ±(1, 0, -1), ±(0, 1, 1), ±(0, 1, -1), (±1, ±1, ±1)}

ω_0=8/27, ω_α=2/27(α=1-6), 1/54(α=1-18), 1/216(α=19-26)

c_s=1/$\sqrt{3}$c

Figure 2.1: DnQb lattice models with discrete velocity directions and weight coefficients.

principle, comprehensive mechanical similarity refers to geometric similarity, kinematic similarity, dynamic similarity, and similar initial and boundary conditions.

To describe flow field, there are five essential variables: $\mathbf{x}$, $\mathbf{u}$, P, ρ, μ which stands for space, velocity, pressure, density, and dynamic viscosity respectively. Here select constant characteristic propertied appropriate to the flow: L_p, U_p, P_p are make physical variables dimensionless. Hence, the dimensionless variables denotes them by an asterisk $t^* = tU_p/L_p$, $x^* = \mathbf{x}/L_p$, $\mathbf{U}^* = \mathbf{u}/U_p$, $P^* = (P - P_p)/\rho U_p^2$. Based on the dimensionless variables, the dimensionless governing equations ignoring external forces for viscous incompressible flow can be obtained as following:

$$\nabla \cdot \mathbf{U}^* = 0 \tag{2.3}$$

$$\frac{\partial \mathbf{U}^*}{\partial t^*} + (\mathbf{U}^* \cdot \nabla^*)\mathbf{U}^* = -\nabla^* P^* + \frac{1}{Re}\nabla^{*2}\mathbf{U}^* \tag{2.4}$$

Different kind of dimensionless number will be applied in different study cases. It is based on the main contradiction in the study problems. There are several similarity criteria in multiphase flow as following:

- Gravitational similarity criterion (Froude modeling)

  It is mainly applied to the problems in which gravity plays a leading role rather than viscous force, such as hydraulic engineering, including ship movement, open channel flow, etc. The corresponding dimensionless number Froude denotes is $Fr = U_p/\sqrt{gL_p} = \sqrt{\rho U_p^2 L_p^2/(\rho g L_p^3)} = \sqrt{\text{inertial force/gravity force}}$

- Viscous force similarity criterion (Reynolds modeling method)

  It is an important physical parameter in the study of pipeline flow, hydraulic fluid, fluid machinery, and boundary layer flow. Its corresponding dimensionless number Reynolds is expressed as $Re = U_p L_p/\mu = \sqrt{\rho U_p^2 L_p^2/(\mu U_p L_p^3)}$ =inertial force/viscous force. If the viscous forces of the two flows are similar, their Reynolds Numbers must be equal, i.e., $Re = Re'$, and vice versa. In the channel flow, when the Reynolds number is less than 2300, the fluid motion remains regular and stable in the laminar flow state. When the Reynolds number is more than 4000, the fluid motion becomes extremely unstable and irregular.

- Surface tension similarity criterion

  It is suitable for problems in which surface tension plays a major role, such as coalescence, boiling, and condensation. There are several dimensionless numbers applied in the multiphase flow.The dimensionless Weber number denotes as $We = \rho U_p^2 L_p/\sigma = \rho U_p^2 L_p^2/\sigma L_p$ =inertial force/surface tension force. It is especially for the multiphase flow with a strongly curved surface. In the dynamics of capillary flow, Capillary number $Ca = \mu U_p/\sigma$ =viscous force/surface tension force plays an important role. Ohnesorge number $Oh = \mu/\sqrt{\rho\sigma L_p}$ =viscous force/$\sqrt{\text{inertia} \cdot \text{surface tension}}$ is often used in the cases related to free surface fluid dynamics such as dispersion, spray and coalescence. Additionally, there is a dimensionless number that is used to characterize the shape of bubbles/droplets moving in the surrounding liquid: Bond number $Bo = \Delta g L_p^2 \sigma$ =gravitational force/surface tension force.

Based on the similarity principle of fluids, in order to ensure the similarity between the numerical and physical flow field, the Reynolds, Froude, and Ohnesoge numbers must be equal. This is the way connect the physical unit with the lattice unit used in the simulation based on the LBM. The characteristic length, velocity, time, dynamic viscosity, surface tension in lattice unit is taken as N_x, U_g, t_g, ν_g, σ_g respectively. So that the relationship between physical and lattice unit is shown as following:

$$l_0 = L_p/N_x \tag{2.5}$$

Velocity is out of consideration in the initial and boundary condition in the study cases of bubble coalescence, so that Ohnesorge number (Oh) is selected as the dimensionless number to do the unit transfer. From the definition of the kinematic viscosity in the LBM $\nu_g = (\tau_0 + 0.5)c_s^2\Delta t$ and $Oh = \nu\sqrt{\rho/\sigma L_p} = \nu_g\sqrt{\rho/\sigma N_x}$, the relaxation time for LBM can be derived as

$$\tau_0 = \frac{1}{2} + \frac{\nu_p}{c_s^2}\sqrt{\frac{\rho\sigma_g}{\rho_g\sigma}} \tag{2.6}$$

Meanwhile, from the relationship between physical and lattice unit of kinematic viscosity $\nu^p/\nu^l = l_0^2/t_0$, t_0 can be derived as

$$t_0 = l_0^2 c_s^2\sqrt{\frac{\rho\sigma_g}{\sigma l_0\rho_g}} \tag{2.7}$$

Because $U_p = L_p/t$ and $U_g = N_x/t_g$, U_0 can be obtained from t_0, l_0 as $U_0 = l_0/t_0$. And the relationship between pressure in lattice and physical unit is illustrated as

$$\frac{P - P_0}{\frac{1}{2}\rho U_p^2} = \frac{P_g - P_g^r}{\frac{1}{2}\rho_g U_g^2} \tag{2.8}$$

Here P_0 and P_g^r is the reference pressure in physical and lattice unit respectively. Meanwhile, in the lattice Boltzmann model $P_g = C_s^2\rho_g$, and $\rho_g^r = 1$ in general, so that the above equation can be re-write as

$$P - P_0 = c_s^2(\rho_g - \rho_g^r)\frac{\rho U_p^2}{\rho_g U_g^2} \tag{2.9}$$

2.1.2 Boundary conditions for LBM

One of the advantages of LBM is easy to handle complex boundaries with simple implementation. There are several common boundary conditions are listed as following. Here take D2Q9 lattice model as a sample for description.

- **Periodic boundary condition**

Periodic boundary [126] usually is applied when the study problems don't take the effects of boundary condition into consideration. It means that if fluid particles leave the flow field from one end boundary, the next time step it will enter the flow field from the other end boundary. As Figure 2.2 shows the particle distribution functions of the outlet points f_1, f_5 and f_8 flowing out to the inlet, and f_3, f_6 and f_7 flowing out of the inlet to outlet. The format can be expressed as

$$\begin{aligned} f_{1,5,8}(0, j) &= f_{1,5,8}(N_x, j) \\ f_{3,6,7}(N_x + 1, j) &= f_{3,6,7}(1, j) \end{aligned} \tag{2.10}$$

Here $f_{1,5,8}(0, j)$, $f_{3,6,7}(N_x + 1, j)$ are the distribution functions in the virtual fluid nodes (grey nodes in Figure 2.2), and $f_{1,5,8}(1, j)$, $f_{3,6,7}(N_x, j)$ are the distribution functions in the fluid nodes (black nodes in Figure 2.2).

- **Bounce-back boundary condition**

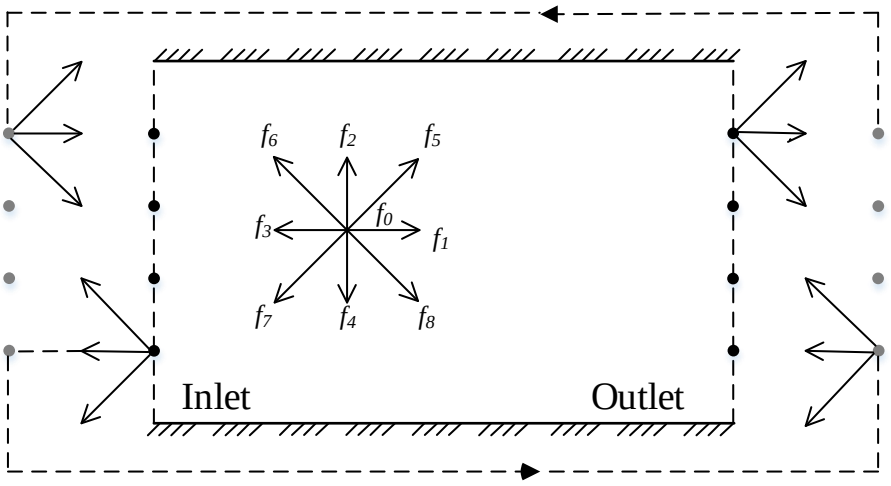

Figure 2.2: Periodic boundary condition

Standard bounce-back boundary condition [126] is usually applied in static no-slip walls. It assumes that particles on a fluid node reach the boundary node, and the next time step velocity bounces back along the original route, as shown in Figure 2.3. So that the distribution function after collision on the wall can be expressed as

$$f_{2,5,6}(i,1) = f_{4,7,8}(i,1) \tag{2.11}$$

$f_{4,7,8}(i,1)$ come from the distribution functions of near fluid nodes position i.e. $f_4(i,2)$, $f_7(i+1,2)$, $f_8(i-1,2)$ after streaming respectively.

- **Non-equilibrium extrapolation model for boundary condition**

Based on the extrapolation model of Chen [127] and Zou's non-equilibrium bounce-back model for boundary condition, Guo [128] *et al.* proposed a new boundary processing method, namely non-equilibrium extrapolation model in 2002. The basic idea is to decompose the unknown distribution function on the boundary lattice into two parts: equilibrium and non-equilibrium $f_\alpha = f_\alpha^{eq} + f_\alpha^{neq}$. The equilibrium part can be obtained by the given boundary condition, and the non-equilibrium part can be derived from the extrapolation model. Here take the velocity boundary condition as an example. As Figure 2.4 shows, the

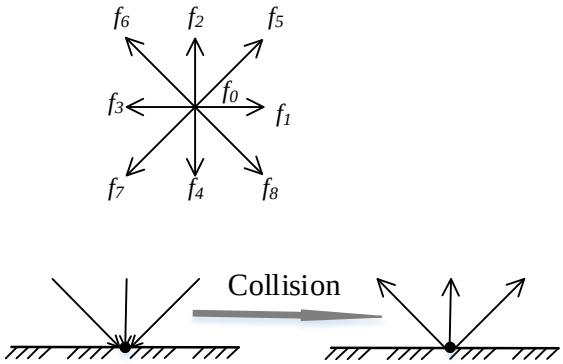

Figure 2.3: Bounce-back boundary condition

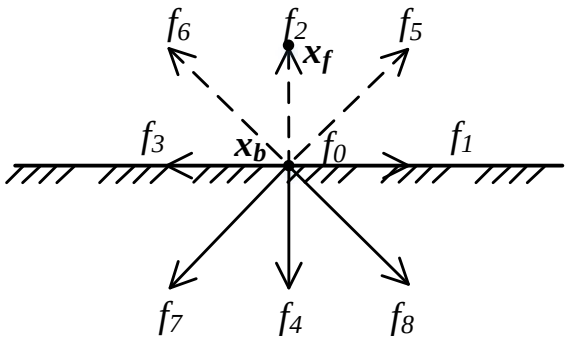

Figure 2.4: Non equilibrium extrapolation model

velocity of the solid node $\mathbf{x_b}$ is $\mathbf{U_b}$, and the density is unknown. The closet fluid node is set as $\mathbf{x_f}$, in this case,the non-equilibrium extrapolation model can be expressed as

$$f_\alpha(\mathbf{x_b}, t_g) = f_\alpha^{eq}(\rho(\mathbf{x_b}, t_g), \mathbf{U_b}) + [f_\alpha(\mathbf{x_f}, t_g) - f_\alpha^{eq}(\mathbf{x_f}, t_g)] \tag{2.12}$$

2.2 Lattice Boltzmann modeling and formulations for multiphase flows

In the current work, We employ the free-energy modeling approach that originated by He *et al.* [84, 85] based on the free-energy theory [129–131] first introduced by Swift *et al.* [86,87]. This model has been continuously developed and refined in the last 10 years by Lee's group [101–104] and it has been claimed that the parasitic current has been eliminated [104]. When the flow involves two fluids, the interfacial behavior arises as a result of microscopic long-range interactions among the constituent molecules of the system [132]. As a result, accounting for interfacial dynamics over a broad range of length and time scales is required in the modeling. There exists two critical issues in the modeling of multiphase flow. First, fluid-fluid interface is a contact discontinuity, where the density is discontinuous but the pressure and velocity are continuous across the interface. Thus, the state equation of ideal gas, used in the LBM modeling for single phase flow, is no longer valid. Non-ideal effects must be introduced through the intermolecular forces between fluids. Second, the

numerical instability caused by the density discontinuity across the interface would pose a severe obstacle when the density ratio is large. It has been well understood that a parasitic current introduced by a slight imbalance in the interfacial stresses due to truncation errors is the key to suppressing parasitic current in the modeling of intermolecular forces [90].

2.2.1 Governing equations for diffusive interface

Using a diffuse interface to separate phases is a popular technique in the modeling of multiphase flow. The advantages include the ease of implementation even for complex three-dimensional interfaces and the suitability to capture singular phenomena such as interface rupture, coalescence, or phase change. For a binary flow, the continuity equation for the species i of binary fluids can be written as

$$\partial\tilde{\rho}_i/\partial t + \nabla \cdot \tilde{\rho}_i \mathbf{u}_i = 0, \qquad i = 1, 2 \tag{2.13}$$

where $\tilde{\rho}_i$ and $\mathbf{u}_i$ denote the local density and velocity of species i. The total density, $\rho(= \tilde{\rho}_1 + \tilde{\rho}_2)$ is conserved in the entire domain. The local density $\tilde{\rho}_i$ and velocity $\mathbf{u}_i$ are linked to the volume averaged velocity $\mathbf{u}$, the bulk density value ρ_i, and the volumetric diffusive flux $\mathbf{j}_i$ of species i (rate of volume flow across a unit area) by

$$\rho_i \mathbf{j}_i = \tilde{\rho}_i(\mathbf{u}_i - \mathbf{u}), \qquad i = 1, 2 \tag{2.14}$$

If the diffusive flow rate is not related to the densities but instead to the local compositions of two species, $\mathbf{j}_1 = -\mathbf{j}_2 = \mathbf{j}$ can be assumed [133], yielding $\nabla \cdot \mathbf{u} = 0$. Furthermore, if $\mathbf{j}$ is assumed to be proportional to a thermodynamic driving force – proportional to the gradient of the chemical potential μ_c as $\mathbf{j} = -M\nabla\mu_c$ with $M > 0$ the mobility [134], and composition C is defined as $C = \tilde{\rho}_i/\rho_i$, Equation (2.13) becomes

$$\partial C/\partial t + \mathbf{u} \cdot \nabla C = \nabla \cdot (M \nabla \mu_c) \tag{2.15}$$

where μ_c is the chemical potential defined as

$$\mu_c = \mu_{c0} - \kappa_p \nabla^2 C \tag{2.16}$$

with μ_{c0} the classical part of the chemical potential. In the vicinity of the critical point, simplification of van der Waals EOS (equation of state) can be made [132] for the control of interface thickness and surface tension at equilibrium. In this case, we assume that the energy E_0 takes the following form [135] of $E_0 = \beta C^2(C-1)^2$ with β being a constant. As a result, $\mu_0 = \partial E_0/\partial C = 2\beta C(C-1)(2C-1))$. The equilibrium profile of C is determined such that the energy E_0 is minimized and reads $\mu_c = const$ in one dimension. In an interface at equilibrium, the interface profile is

$$C(z) = 0.5 + 0.5\tanh(2z/D) \tag{2.17}$$

where z is the distance normal to the interface and D is the interface thickness, which is chosen based on accuracy and stability. Given D and β, one can compute the gradient parameter $\kappa = \beta D^2/8$ and the surface tension force $\sigma = \sqrt{2\kappa\beta}/6$.

For a binary flow, we introduce the intermolecular force [103] as $\mathbf{F} = \frac{1}{3}\nabla\rho c^2 - \nabla p_1 - C\nabla\mu_c$ where p_1 is the hydrodynamic pressure, whereas the thermodynamic pressure p_0 is defined by $p_0 = C\partial E_0/\partial C - E_0 = \beta C^2(C-1)(3C-1)$. The total pressure is $p = p_0 + p_1 - \kappa C\nabla^2 C + \kappa|\nabla C|^2/2$. When Ma is low, $p_1/p_0 \sim O(Ma^2)$, and all thermodynamic quantities are independent of the hydrodynamic pressure [136], meaning that the density of the fluid does not depend on the hydrodynamic pressure. In the motionless flow, the contribution from the hydrodynamic pressure p_1 disappears, as do parasitic currents. The momentum and pressure evolution equation are as following

$$\partial p_1/\partial t + \rho c_s^2 \nabla\cdot\mathbf{u} = 0 \tag{2.18}$$

$$\rho(\partial\mathbf{u}/\partial t + \mathbf{u}\cdot\nabla\mathbf{u}) = -\nabla p_1 + \mu_c\nabla C + \nabla\cdot\mu(\nabla\mathbf{u} + (\nabla\mathbf{u})^T) \tag{2.19}$$

2.2.2 Lattice Boltzmann equations for binary flow

In the study cases of multiphase flow, the lattice Boltzmann equation (LBE) (before the time discretization) including the intermolecular force reads [84]

$$\partial f_\alpha/\partial t + \mathbf{e}_\alpha\cdot\nabla f_\alpha = -(f_\alpha - f_\alpha^{eq})/\lambda + \frac{1}{c_s^2}(\mathbf{e}_\alpha - \mathbf{u_g})\cdot\mathbf{F_g} f_\alpha^{eq} \tag{2.20}$$

where λ is the relaxation time is related to the kinematic viscosity $\nu_g = c_s^2\lambda$. The equilibrium distribution function is a function of local macroscopic density and velocity and is formulated up to $O(u^2)$ as Equation 2.2

In the single-phase LBM modeling, the particle distribution function is closely associated with fluid density and momentum. Thus, the variation of density across the interface will result in a variation of the particle distribution functions. When the density ratio of two fluids is large, the large variation of the particle distribution functions will cause servers numerical instability and jeopardize the simulation. To overcome this numerical problem, He *et al.* [85] creatively introduced an incompressible transformation to change the particle distribution function for density and momentum into that for pressure and momentum. As pressure is continuous across the interface, the high variation of the particle distribution function is avoided. Later, Lee and Lin [101] also adopted the same transformation technique and then Lee continuously refined it through a series of stable discretization schemes to enhance numerical stability [102–104].

Define a new particle distribution function

$$g_\alpha = f_\alpha c_s^2 + (p_{g1} - \rho_g c_s^2)\Gamma_\alpha^{eq}, \tag{2.21}$$

in which $\Gamma_\alpha(\mathbf{u_g}) = f_\alpha^{eq}/\rho_g$. Taking the total derivative $D_t = \partial_t + \mathbf{e}_\alpha \cdot \nabla$ of g_α results in

$$\partial g_\alpha/\partial t + \mathbf{e}_\alpha \cdot \nabla g_\alpha = -(g_\alpha - g_\alpha^{eq})/\lambda + (\mathbf{e}_\alpha - \mathbf{u_g}) \cdot [\nabla \rho_g c_s^2(\Gamma_\alpha - \Gamma_\alpha^{eq}) - C\nabla \mu_{gc}\Gamma_\alpha] \tag{2.22}$$

where the new equilibrium g_α^{eq} is

$$g_\alpha^{eq} = \omega_\alpha\Big[p_{g1} + \rho_g((\mathbf{e}\cdot\mathbf{u_g}) + (\mathbf{e}_\alpha \cdot \mathbf{u_g})^2/2c_s^2 - u_g^2)\Big] \tag{2.23}$$

Discretizing Equation (2.22) along characteristics over the time step δt, we obtain the LBE for g_α

$$\bar{g}_\alpha(\mathbf{x_g}+\mathbf{e}_\alpha\delta t, t_g+\delta t) = \bar{g}_\alpha(\mathbf{x_g}, t) - \frac{(\bar{g}_\alpha - \bar{g}_\alpha^{eq})|_{(\mathbf{x_g},t_g)}}{\tau+0.5} + (\mathbf{e}_\alpha - \mathbf{u_g})\cdot[\delta t\nabla^{MD}\rho_g c_s^2(\Gamma_\alpha(\mathbf{u_g}) - \Gamma_\alpha^{eq}) - C\delta t\nabla^{MD}\mu_{gc}\Gamma_\alpha]|_{(\mathbf{x_g},t_g)} \tag{2.24}$$

where ∇^{MD} means mixed difference approximation, and ∇^{CD} means central difference approximation [104] and the non-dimensional relaxation time $\tau = \lambda/\delta t$. In Equation (2.24), the modified particle distribution function $\bar{g}_\alpha$ and the equilibrium distribution function $\bar{g}_\alpha^{eq}$ are introduced to facilitate computation

$$\bar{g}_\alpha = g_\alpha + \frac{(g_\alpha - g_\alpha^{eq})}{2\tau} - \frac{\delta t}{2}(\mathbf{e}_\alpha - \mathbf{u_g}) \cdot \left[\nabla^{CD}\rho_g c_s^2 (\Gamma_\alpha(\mathbf{u}) - \Gamma_\alpha(0)) - C\nabla^{CD}\mu_{gc}\Gamma_\alpha\right] \quad (2.25)$$

$$\bar{g}_\alpha^{eq} = g_\alpha^{eq} - \frac{1}{2}\delta t (\mathbf{e}_\alpha - \mathbf{u_g}) \cdot \left[\nabla^{CD}\rho_g c_s^2 (\Gamma_\alpha(\mathbf{u_g}) - \Gamma_\alpha(0)) - C\nabla^{CD}\mu_{gc}\Gamma_\alpha\right] \quad (2.26)$$

The hydrodynamic pressure, and momentum can be computed by taking the zeroth and first moments of $\bar{g}_\alpha$

$$\rho_g u_g = \frac{1}{c_s^2}\sum \mathbf{e}_\alpha \bar{g}_\alpha - \frac{\delta t}{2} C\nabla^{CD}\mu_{gc} \quad (2.27)$$

$$p_{g1} = \sum \bar{g}_\alpha + \frac{\delta t}{2}\mathbf{u_g} \cdot \nabla^{CD}\rho_g c_s^2 \quad (2.28)$$

Thus the continuity equation is transformed into the constraint on the velocity field.

For the transformation of the composition C, a second distribution function is introduced in a simple format of $h_\alpha = (C/\rho_g) f_\alpha$ and $h_\alpha^{eq} = (C/\rho_g) f_\alpha^{eq}$. Similarly, taking the total derivative D_t of h_α and utilizing Equation (2.15) yield

$$\bar{h}_\alpha(\mathbf{x_g} + \mathbf{e}_\alpha\delta t,\, t_g + \delta t) = \bar{h}_\alpha(\mathbf{x_g},\, t) - \frac{\left(\bar{h}_\alpha - \bar{h}_\alpha^{eq}\right)|_{(\mathbf{x_g},\, t)}}{\tau + 0.5} + \delta t (\mathbf{e}_\alpha - \mathbf{u_g}) \cdot [\nabla^{MD} C - \frac{C}{\rho_g c_s^2} \left(\nabla^{MD} p_g + C\nabla^{MD}\mu_{gc}\right)]\Gamma_\alpha|_{(\mathbf{x_g},\, t)} + \delta t M \nabla^2 \mu_{gc}\, \Gamma_\alpha|_{(\mathbf{x_g},\, t)} \quad (2.29)$$

and the modified particle distribution function $\bar{h}_\alpha$ and $\bar{h}_\alpha^{eq}$ are defined as [104]

$$\bar{h}_\alpha = h_\alpha + \frac{1}{2\tau}(h_\alpha - h_\alpha^{eq}) - \frac{\delta t}{2}(\mathbf{e}_\alpha - \mathbf{u_g}) \cdot [\nabla^{CD} C - \frac{C}{\rho_g c_s^2}(\nabla^{CD} p_g + C\nabla^{CD}\mu_{gc})]\Gamma_\alpha \quad (2.30)$$

$$\bar{h}_\alpha^{eq} = h_\alpha^{eq} - \frac{\delta t}{2}(\mathbf{e}_\alpha - \mathbf{u_g}) \cdot [\nabla^{CD} C - \frac{C}{\rho_g c_s^2}(\nabla^{CD} p_g + C\nabla^{CD}\mu_{gc})]\Gamma_\alpha \quad (2.31)$$

The composition can be computed by taking the zeroth moment of $\bar{h}_\alpha$

$$C = \sum_\alpha \bar{h}_\alpha + 0.5\delta t M \nabla^2 \mu_{gc} \quad (2.32)$$

As discussed in reference [103], the interfacial mobility M in Equation 2.32 plays a role to suppress the nonphysical parasitic currents caused by the numerical discretization. M should be chosen carefully large enough so that the diffusion maintain the interface near its equilibrium state but small enough to avoid damping the flow near the interface. In the present study, we set $M(=\ 6.67)$ as constants as suggested. The density ρ and the dimensionless relaxation frequency $(1/\tau)$ are taken as linear functions of the composition by

$$\rho_g(C) = C\rho_{g1} + (1-C)\rho_{g2}, \quad 1/\tau(C) = C/\tau_1 + (1-C)/\tau_2 \tag{2.33}$$

Boundary conditions

If ignoring the effects of the boundary condition, the periodic boundary condition as Sec.2.1.2 indicated will be applied in the simulation. However, taking the solid boundary effects into consideration for lattice Boltzmann modeling of the gas-liquid flow, there are 4 different types of the boundary conditions as following.

1) Unknown particle distribution functions at boundary nodes are obtained from the bounce-back scheme i.e. $g_\alpha(\mathbf{x_s}, t_g) = g_\alpha(\mathbf{x_f}, t_g)$ and $h_\alpha(\mathbf{x_s}, t_g) = h_\alpha(\mathbf{x_f}, t_g)$, $\mathbf{x_s}$ is the node on the boundary, $\mathbf{x_f} = \mathbf{x_s} - \mathbf{e}_\alpha\delta t$ is the node in the fluid.

2) The boundary for the $\nabla\phi$ is applied to prevent unphysical mass and momentum transfer through the boundary nodes. ϕ is macroscopic variables such as p_1, C, μ_c. The no flux condition is presented as $e_\alpha\dot{\nabla}\phi|_s = 0$. Discrete the no flux condition, it can be simplified as $\phi(\mathbf{x_s} + \mathbf{e}_\alpha\delta t) = \phi(\mathbf{x_s} - \mathbf{e}_\alpha\delta t)$, $\phi(\mathbf{x_s} + 2\mathbf{e}_\alpha\delta t) = \phi(\mathbf{x_s} - 2\mathbf{e}_\alpha\delta t)$, where the points $(\mathbf{x_s} + \mathbf{e}_\alpha\delta t)$, $(\mathbf{x_s} + 2\mathbf{e}_\alpha\delta t)$ are in the fluid domain, the points $(\mathbf{x_s} - \mathbf{e}_\alpha\delta t)$, $(\mathbf{x_s} - 2\mathbf{e}_\alpha\delta t)$ are out of the fluid domain.

3) The boundary for $\nabla^2\mu_{gc}$ ensures no mass flux in the normal direction of the solid wall, i.e

$$\mathbf{n}\cdot\nabla\mu_c|_s = 0. \tag{2.34}$$

4) The boundary for $\nabla^2 C$ can be derived from minimizing the free surface energy $\Psi_s = \int_S (\phi_0 - \phi_1 C_s + \phi_2 C_s^2 - \phi_3 C_s^3 + \ldots) dS$ caused by the interactions between the liquid-gas interface and solid surface.

   Minimizing the total energy by calculus of variations [137] leads to

$$\mathbf{n} \cdot \nabla C|_s = d\Psi_s / dC_s \tag{2.35}$$

   $\mathbf{n}$ is the unit vector in the normal direction of the solid wall. Retain higher-order terms in Ψ_s can avoid the numerical instability. Hence, the cubic boundary condition is selected [100] in this work, the condition for solid wall i.e. Equation 2.35 can be simplified as

$$\mathbf{n} \cdot \nabla C|_s = -\phi_c / \kappa_g (C_s - C_s^2), \tag{2.36}$$

   $\phi_c = \Omega_c \sqrt{2\beta_g \kappa_g}$. Here Ω_c is the wetting potential which related to the contact angle α i.e. $\Omega_c = cos\alpha$.

While the formation of LBEs in Section 2.2.2 seems complicated, the implementation of flow chart is straightforward as Figure 2.5.

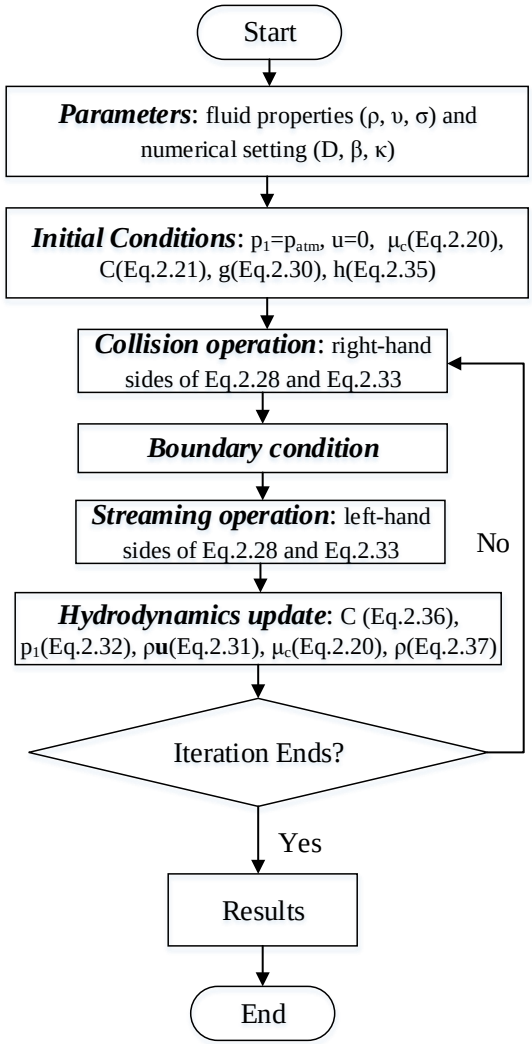

Figure 2.5: Flow chart of LBM implementation

3. GPU PARALLELISM AND ACCELERATION FOR LBM

One of the advantages of the LBM is the suitability for GPU parallelism. The GPU acceleration has been practiced in our research group for a couple years for different research areas such as turbulence [138], biomedical flows [139] and porous media flows [140, 141]. The general flow chart of GPU implementation is indicated in Figure 3.1. The difference between GPU parallel and CPU serial is the device used for the LBM implementation. To achieve an efficient GPU-LBM algorithm, it is important to combine feature of GPU with LBM. Firstly, A-B (2 sets of distribution functions) pattern is applied before and after streaming to avoid data dependency. Then developed CUDA parallel algorithms are employed in our simulation that include dynamic allocation, data layout, propagation scheme, register utilization, branch divergence removal and multi-GPU.

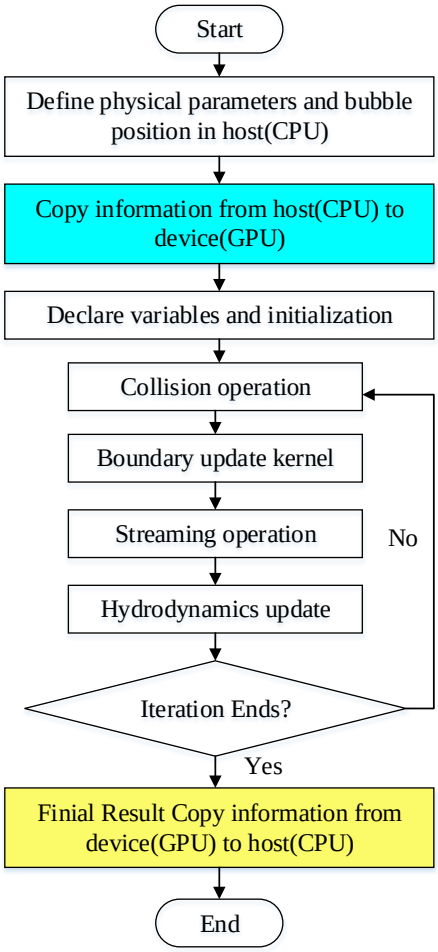

Figure 3.1: Flow chart of GPU Implementation

3.1 Dynamic allocation

By default, the compiled model for a code has a characteristic that the instructions and parameters of the code must be linked in the 2GB static continuous address space. This limitation takes the dominant effect in impeding the simulation of large scale problems. For the multiphase flow, flow properties (density, velocity, pressure, chemical potential, and composition), two sets of distribution functions of lattice Boltzmann model are essential

arrays to be defined in the CPU host. From the experience of investigating the temporal information of the global process of two bubbles coalescence in two-dimension (2D) space, the mesh size should be around 800×800. Meanwhile, if the investigation is on the spatial information of the bubble coalescence, three-dimension (3D) model is in demand. The mesh size is around $220 \times 120 \times 220$ for our calculation. Meanwhile, the mesh size is up to $280 \times 140 \times 280$ due to the limitation of 2GB static continuous address space. All these experience based on the two bubble coalescence, a bubbly problem, especially for the complex geometry, the needed memory must be larger than 2GB. Nowadays, a single NVidia GPU card has up to 12GB of memory for computing. Hence, it is critical to find a way to release this limitation. Dynamic memory (heap) instead of a static memory (stack) is applied in our simulations. Dynamic memory (heap) is randomly allocating portions from a large pool of memory. However, the data copy between CPU (host) to GPU (device), the transmission array should be logically contiguous. Hence, in our algorithm, a class has been developed.

- The class can dynamically allocate memory in one dimension array, and each variable only uses a total of $5\times$sizeof(float) or sizeof(double) on the stack. Each variable includes three dimensions in different directions, one variable of fluid properties, and data precision. The illustration likes Array3<precious; 3 dimensions in different directions> variable of fluid property. Here take composition C as an example, the class is Array3<double; nx; ny; nz> C.

- All the other memory is allocated dynamically on the heap orderly in a continuous block through properly overloading the copy constructor. And the information which is related to assignment operators will be swap and destroyed.

This class is to manage allocation, deallocation of memory, and utilize the full memory capacity of the GPU cards easily.

3.2 Memory access pattern

3.2.1 Propagation scheme

Propagation in the LBM relates to streaming. During the streaming, there is a problem called misaligned access. There are two main strategies to address this issue in literature as ‘push’ and ‘pull’ algorithms depending on the streaming direction which shows as Figure 3.2 and 3.3. The streaming direction of ‘push’ scheme is the same as usual streaming which pushes particles from the current cell to the adjacent cells, in other words, it has aligned read and misaligned write in the implementation. The distribution function after the collision is stored in a lattice as Figure 3.2(a) indicated. Then the post-streaming values push to the adjacent cell as the Figure 3.2(b) shows. Whereas ‘pull’ scheme has opposite streaming direction, it pulls particles from the adjacent cells to current cell. In the implementation, it yields to misaligned read and aligned write. The distribution function read from the adjacent cells as Figure 3.3(a) shows. After streaming, the values propagate to the local cell, as Figure 3.3(b) illustrates. Since misaligned read is faster than misaligned write in the GPU [113], the ‘pull’ scheme is employed in our simulation.

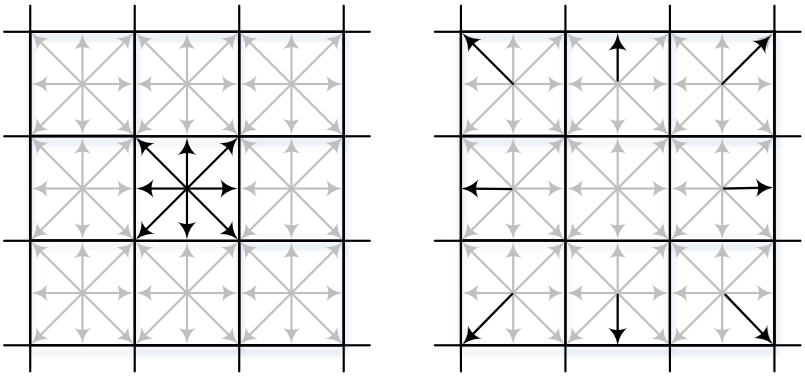

(a) Aligned read (b) Misaligned write

Figure 3.2: Push scheme for propagation. (a) the state before streaming with aligned read, (b) the state after streaming with misaligned write.

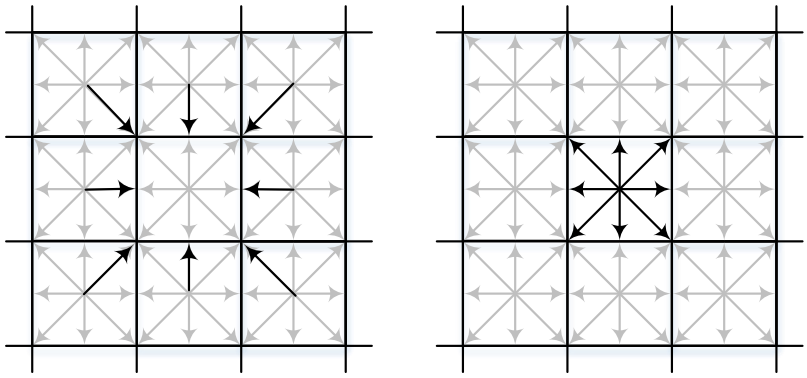

(a) Misaligned read (b) Aligned write

Figure 3.3: Pull scheme for propagation. (a) the state before streaming with misaligned read, (b) the state after streaming with aligned write.

3.2.2 Data layout

Coalesced memory access is an efficient way to reduce the memory latency of a GPU program that results in acceleration. Coalesced memory access means all the threads in a block access continuous memory address. Hence, the multiple dimensions arrays are expanded into one dimension arrays. We take the D3Q19 model in Figure 2.1 and assume the mesh size $nx \times ny \times nz$ to show the data layout in the GPU. Regularly, the DF stores as 4D array on the CPU such as $f[x][y][z][i]$. Here x, y, z presents the space; i ranges from 0 to 18. Different structure of one-dimensional array in the GPU leads to different effectiveness in the GPU acceleration. There are two main schemes for data layout: Array of Structure (AoS) and Structure of Array (SoA).

- Array of Structure (AoS)

  Nineteen distributions of each cell are arranged 19 consecutive elements of the 1D array illustrated in the top panel of Figure 3.4. The one dimension array format is $f[z \times ny \times nx \times 19 + y \times nx \times 19 + z \times 19 + i]$. This schema is preferred employed in the CPU parallelization.

- Structure of Array (SoA)

  The value of one distribution of all cells in whole computational domain occupies

consecutive elements in memory, which indicated in the bottom panel of Figure 3.4. The distribution functions are addressed as $f[i \times z \times nz \times ny \times nx + z \times ny \times nx + y \times nx + z]$. In this scheme, the number of the thread of DFs within a wrap (32 threads) can access consecutive memory. So it has been reported that the SoA scheme is suitable for the GPU acceleration [142].

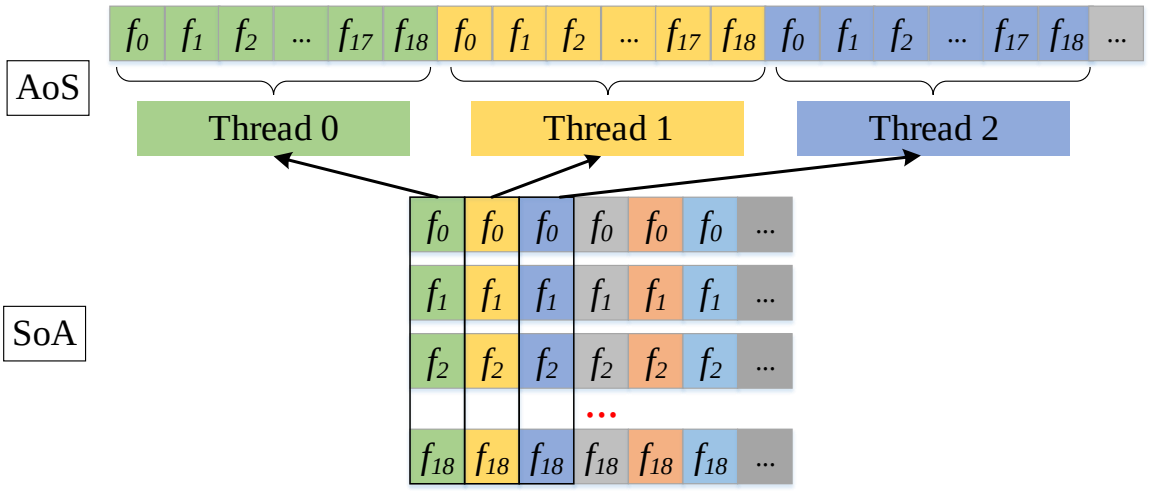

Figure 3.4: Data layout: AoS and SoA

3.3 Register Utilization

CUDA provides a memory hierarchy, including device memory and on-chip memory, as shown in Figure 3.5. Our attention is mainly on the followings.

- **Global Memory**

  Global memory is the main part of the device memory. Access of this memory has a high latency of 400–600 cycles [143]. For data-intensive numerical method like LBM, a large amount of data would be fetched. This latency is of considerable importance. In Fermi memory hierarchy, the access is cached by L1 and L2 caches by default. Each L1 cache line has 128 bytes and would be matched with a continuous

segment of 128 bytes in global memory. To pursue high performance, it is important to pack the data sequentially. For example, a 1D array in global memory, and make sure the access executed by a warp is coalesced and aligned to these sequential addresses. Otherwise, data would be transferred, leading to a waste of bandwidth.

- **Register**

  The register is a kind of on-chip resource distributed to each thread. It can be accessed as fast as 32 bits per cycle. The amount of registers may limit the number of concurrent threads on each SM.

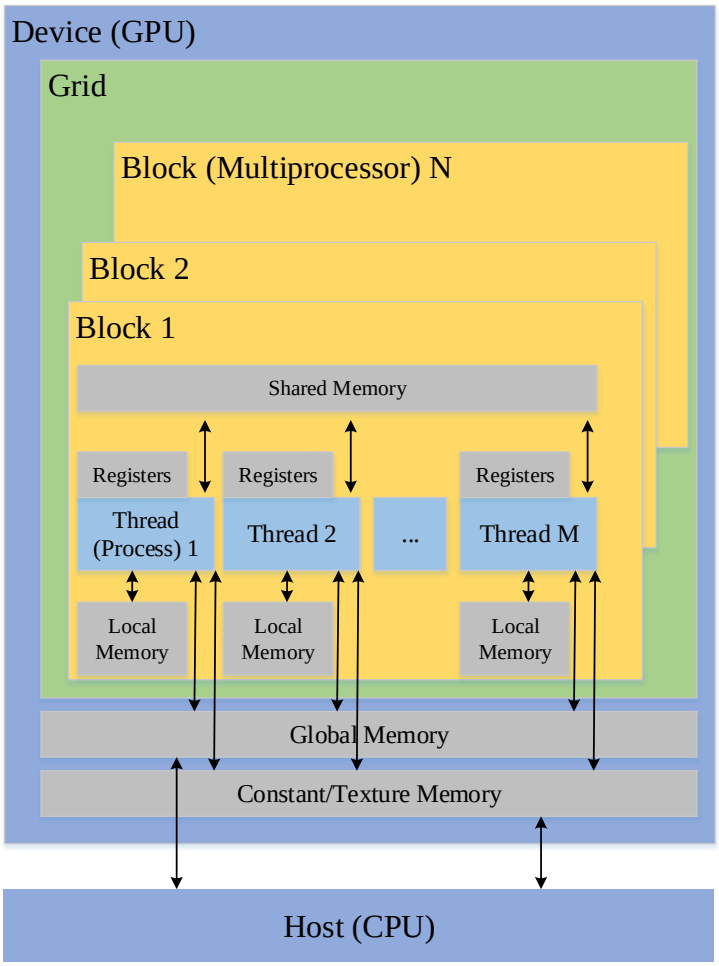

Figure 3.5: Illustration of GPU device memory

- **Shared Memory**

  Similar to the register, shared memory can be fast accessed but limited by its upper bound of storage. However, the shared memory, like L1 cache, is available to all the threads in the same block. It enables efficient communication inside a block. Shared memory is divided into 32 banks. It is noted that multiple accesses to the same banks, such as a broadcast, would cause a conflict and serial execution.

- **Local Memory**

  When registers or shared memory spill, the extra data will be stored in local memory. The latency of this type of memory is similar to global memory. The maximum number of registers used by each thread may be manually set to invoke more concurrent threads at the expense of accessing local memory. If carefully handled, this kind of trade-off can improve performance.

In these kinds of conditions, register memory is better to be applied in the optimization due to the low latency. Whereas the amount of registers is limited, a single streaming multiprocessor contains 65,536 registers for Tesla K20, and the memory for each register is 32-bit. While too many registers are assigned in each thread, it can't take full utilization in the memory. For example, 44 registers are needed in the D3Q19 per thread, and 1024 threads in one block. 44K registers will be used in one block. In this case, the remaining 21K registers are unused, and only one block is applied in the simulation, then get approximate 60% utilization. So utilization of register memory effectively in each thread is critical in the GPU optimization. Selection of the grid and block size is a scheme to get higher register memory utilization.

3.4 Branch divergence Removal

During the execution, all 32 threads inside one block sequentially compose a warp. When one warp of threads is waiting for data transfer, other warps, which are ready for executing instructions, would be selected out and executed. Therefore the time spent for computation and data access can be overlapped, leading to latency hiding. For execution,

CUDA adopts single instruction with multiple threads of architecture where groups of up to eight threads will execute the same instruction in a thread processing array. If the threads inside a warp are not on the same executive path, some data dependence of if-else branch will be involved. In this case, the implementation of different branches has to be serialized. In order to avoid using if-statements, the update of boundary condition is realized in another kernel. Due to the stretch direction changes at the boundary, the choice of blocksize will be changed.

3.5 Multi-GPU

The multi-GPU part of my research is in the infant stage. Current programming is based on the basic idea of the multi-GPU not include any optimizations. However, it improves the performance of the GPU acceleration is obvious in the large scale problems. The basic idea of the multi-GPU is splitting the total memory into several parts which read and written with different GPU cards. Before doing the multi-GPU parallel, two properties of the device should be checked. Firstly, can the device be able to do peer to peer communication (P2P)? And then, how many GPU cards can be applied in a calculation? As Figure 3.6 shows, there are three regions in each GPU card, including internal (white region), halo (orange region), and padding part (green region). First, compute the internal and halo parts in a stream. Then exchange halo data between neighboring GPUs in a different stream to update the data in different GPU devices. For example, the halo regions in GPU 0 will be transferred to the beginning padding part of GPU 1. And the padding part in the GPU 0 will get the information in the halo regions in the GPU 1. Next, synchronize computation on all devices before

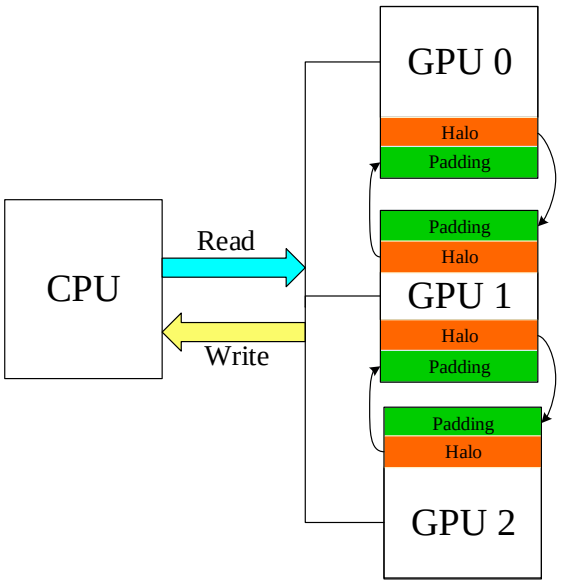

Figure 3.6: A schematic of data transfer between GPUs

proceeding to the next iteration by *cudaDeviceSynchronize()*. Last, the data from all the devices will be written in the CPU part ignore the padding part.

3.6 Performance test

In our research group, there are five computational resources with different types of CPU and GPU cards, as Table 3.1 shows. We employed the CUDA parallel algorithm and tested the speed-up with these four of five machines. The local PC usually is used for debugging the programming. The same code is applied to different machines. The speed-up between different machines with the ME machine is shown in the last column of Table 3.1.

	Machine Name	CPU	GPU	Speed-up
1	MERESPGU (ME Dept)	Intel(R) Xeon(R) E5645	Tesla C2050	1
2	PSC (Bridges)	Intel Broadwell E5-2683 v4	P100	20
3			K80	5
4	DRAGON (Math Dept)	Intel(R) Xeon(R) X5660	Tesla C2750	1
5	Local PC	Intel(R) Xeon(R) E5-2609 v2	Quadro K4000	N/A

Table 3.1: information of the resource used in the computation and speed-up between different machines with the ME machine

In the dissertation, there are three different cases needed to be tested: 2D with a liquid-gas interface and periodic boundary condition by a single GPU (case 1), 3D with a liquid-gas-solid interface and bounce-back boundary condition by a single GPU (case 2) and multi-GPU (case 3). Case 1 and case 2 are tested with the machine 3. Machine 4 has four GPU cards that is used to test the performance for case 3.

- Case 1

  The acceleration is indicated as Table 3.2 with different spatial resolutions 200×200, 400×400, 600×600, 800×800, 1000×1000. Here, MLUPS (Million Lattice Updates

Per Second) is applied to indicate the computation performance. Take resolution 1000×1000 as an example. The speed-up is 1164 between GPU parallel and serial execution. In other words, the time for a complete simulation should be 583.2 hours with serial execution, whereas, the time with the parallelism is only half an hour .

Resolution	GPU parallel (MLUPS)	Serial (MLUPS)	Speed-up	Parallel vs. Serial (in hour)
200×200	310	0.479	648	0.01/8.0
400×400	350	0.422	830	0.06/49.8
600×600	398	0.396	1004	0.15/151.2
800×800	418	0.378	1104	0.30/331.2
1000×1000	426	0.367	1164	0.50/583.2

Table 3.2: Performance test of GPU parallel and CPU serial for case 1. The last column is a comparison of parallel vs. serial wall-clock time for a global process of bubble coalescence.

- Case 2

  The gas-liquid-solid interface is taken into consideration in the case 2. Table 3.3 exhibits the GPU acceleration with five different spatial resolutions $88 \times 48 \times 88$, $132 \times 72 \times 132$, $176 \times 96 \times 176$, $220 \times 120 \times 220$, $264 \times 144 \times 264$. The speed-up increases with resolution increases. Here, take the resolution $220 \times 120 \times 220$ as an example, the speed-up is 2110. A numerical case can be done within half an hour with parallel execution, whereas it takes 44 days with serial execution.

- Case 3

  Multi-GPU is applied in the case 3. Table 3.4 exhibits the GPU acceleration with three different spatial resolutions $45 \times 54 \times 108$, $220 \times 120 \times 220$ and $280 \times 140 \times 280$ by one, two, three, four GPU cards separately. Accelerating the performance by multi-GPU is only existed when resolution is high. When the resolution is low, it is better to have the implementation in the single GPU.

Resolution	GPU parallel (MLUPS)	Serial (MLUPS)	Speed-up	Parallel vs. Serial (in hour)
$88 \times 48 \times 88$	181	0.13	1428	0.02/29
$132 \times 72 \times 132$	176	0.11	1653	0.08/132
$176 \times 96 \times 176$	200	0.11	1758	0.25/439
$220 \times 120 \times 220$	211	0.10	2110	0.50/1055
$264 \times 144 \times 264$	206	0.10	1994	1.25/2492

Table 3.3: Performance test of GPU parallel and CPU serial for case 2. The last column is a comparison of parallel vs. serial wall-clock time for a global process of bubble coalescence.

Resolution	$45 \times 54 \times 108$	$220 \times 120 \times 220$	$280 \times 140 \times 280$
1 GPU (MLUPS)	9.6	10.6	14.0
2 GPUs (MLUPS)	8.5	18.4	20.3
3 GPUs (MLUPS)	5.7	26.6	29.3
4 GPUs (MLUPS)	5.7	34.5	37.3
Speed-up	1.0/0.88/0.59/0.59	1.0/1.74/2.52/3.27	1.0/1.45/2.10/2.67

Table 3.4: Performance test of different numbers of GPU card.

In this dissertation, the total number of computational jobs is around 240. Corresponding, the computational time is estimated as 5 years with a serial execution. The suitability of LBM for parallel computing provides an excellent opportunity to overcome such a computation bottleneck.

4. TEMPORAL/SPATIAL BEHAVIORS OF BUBBLE COALESCENCE

4.1 Introduction

Microbubble coalescence is referred to an evolving process from two (or more) touched parent bubbles, to one single child bubble. A global coalescence typically consists of two stages. The first is the early coalescence during which neck bridges form and grow. The second is the post coalescence toward a child bubble with a minimal surface area. Microbubble coalescence exists in many applications such as airlift bioreactors [144], targeted drug and gene delivery [58], water and wastewater treatment [145], food storage [146], and so on. In some cases, rapid coalescence might be desirable, for example, to control bubble formation during gas injection from a micro-tube into the channel of a downward liquid cross-flow [35]. While in other systems, coalescence needs to be prevented or suppressed to avoid the loss of the total liquid-gas surface area. Therefore, it is of general interest to explore the dynamics of microbubble coalescence under various influences for better control of various gas-fluid systems.

There have been efforts to investigate different factors on individual stages of microbubble coalescence through mathematical analysis, laboratory experiment, and numerical simulation. The majority efforts have been made to reveal various effects on the early coalescence [47, 54, 147–149], during which a half power-law temporal scaling of neck growth has been well derived and validated. Among those, Paulsen *et al.* [54] sophisticatedly studied the effects of dense surrounding fluid on the formation of an infinitesimal neck bridge and discovered that outer fluid has a marginal impact on the dynamics of neck bridge formation and evolution. Whereas, the post-coalescence stage has not been well addressed. An early attempt was on the mathematical modeling for an oscillating elliptic bubble/droplet [64] and its numerical simulation [66] under characterized parameters. Based on

these early works, Stover *et al.* [71] was the first to experimentally study the microbubble oscillation focusing on the effects of liquid viscosity and surface tension on the decay of the damped oscillation. But this study stopped well short of quantitative exploration of the underlying physics of the oscillation. Unveiling post-coalescence is substantially meaningful to industrial processes to control microbubbles as very different behavior could occur in this stage such as damped oscillation [71, 150], shrinking [151], and off-center/head-on separation [152], etc. However, there remain challenges to study global coalescence, especially unequal size bubbles, are involved due to the demanding computation cost and/or the involvement of big data.

4.2 Computational set-up

To study spatial and temporal behaviors of global process of two unequal microbubbles coalescence in a square domain with the side length of $100(\mu m)$. as schematized in Figure 4.1. To distinguish the parent bubbles, we denote the large bubble as a father (F) with radius r_F and the small one as a mother (M) with r_M. The size inequality of the parent bubbles, γ, is defined by the ratio of the radii, r_F/r_M. For the purpose of exploring the effects of size inequality on bubble coalescence, we fix the size of the father bubble as $r_F = 20(\mu m)$ and vary r_M from $5(\mu m)$ to $20(\mu m)$, resulting in a range of γ from 4 to 1, among which $\gamma = 1$ is a limited case corresponding to equal-size coalescence. The fluid is filled in the domain. With the origin, $(0, 0)$ of a Cartesian coordinate system at the south-west corner of the domain, F is placed at $x = 30(\mu m)$ and $y = 50(\mu m)$ and M is attached to F at the same height. Thus, the mother bubble with radius r_M is located at $x = 50 + r_M(\mu m)$ and $y = 50(\mu m)$. The coalescence time (T) is referred to the entire merging time from two touched parent bubbles (solid circles) to one single child bubble (dash circle) with the minimum area surface and the size inequality. Subscript of "h" and "l" denote the heavy and light fluid respectively. The density and viscosity ratios of two fluids are defined as $\rho^* = \rho_h/\rho_l$ and $\mu^* = \mu_h/\mu_l$ respectively. The Ohnesorge number (Oh) is a dimensionless number that relates the viscous forces to inertial and surface tension

forces, and it is defined as $Oh(\equiv \mu_h/\sqrt{\rho_h \sigma R})$. The gas is fixed to air with density $\rho_l = 1.28kg/m^3$ and dynamic viscosity $\mu_l = 1.74 \times 10^{-5} kg/(m \cdot s)$. The density and viscosity ratios vary from $350 - 1361, 614 - 2130$ respectively. And surface tension in the range of $\sigma = (1.6 - 7.2) \times 10^{-2} N/m$. This physical setting results in a range of Oh numbers from 0.039 to 1.543 when the initial bubble radius R_0 is $20\mu m$. The corresponding parameters in lattice unit applied in simulation are selected as $\rho_{gh} = 1.0$, $\rho_{gl} = 1.0/\rho^*, \sigma_g = 10^{-3}, D = 4, \beta_g = 0.003$.

4.3 Convergence check & Verification

Mass conservation check As shown in Table 4.1, the relative mass changes before and after 2000 time steps are compared for four inequality cases of $\gamma = 4, 2, 1.33$, and 1. The mass change per time step is about 5.0×10^{-8}, which is acceptable for mass conservation.

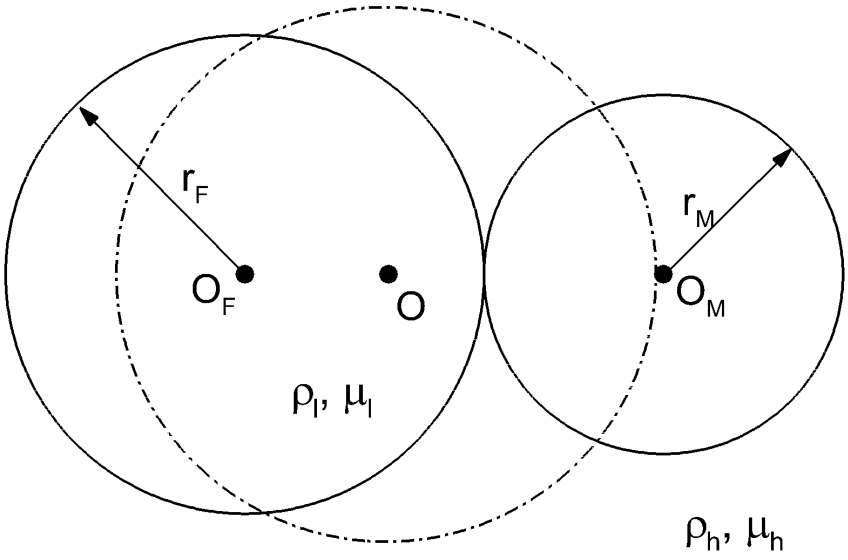

Figure 4.1: Schematics for the coalescence of two unequal bubbles initially touched (solid circles) toward one single bubble (dash circle) in a square domain.

Ratio (γ)	Mass change per time step
4	5.01^{-8}
2	5.02×10^{-8}
1.33	5.03×10^{-8}
1	5.5×10^{-8}

Table 4.1: Mass conservation check

Laplace-law check Maintaining the physical size of the bubble and flow domain, we use five spatial resolutions of 100^2, 200^2, 300^2, 600^2, and 800^2 to simulate the father bubble starting from the initial conditions described above, respectively. When the bubble reaches a steady state, the pressure difference across the air-water interface is calculated by $\triangle p = p_o - p_a$ in which p_o and p_a are the pressure value where $dp/dx \simeq 0.0$ adjacent the diffusive interface in air and oil sides respectively.It is found that the relative errors of $\triangle p$ over the analytical prediction from Laplace theory, $\triangle p = \sigma/R = 3.6kPa$, corresponding to the above resolution sequence are 12.1%, 1.95%, 1.1%, 0.63%, and 0.34%. We use 600^2 as the spatial resolution to produce the relationship between $\triangle p$ and r_F and compare with Laplace law as a validation. Six microbubbles with the radius from $20 - 40(\mu m)$ are simulated. The dependence of $\triangle p$ to $1/r_F$ is shown in Figure 4.2. It is seen that the simulation results (symbols) agree well with the analytical prediction (line), demonstrating the validity of the LBM modeling and simulation.

Convergence check of oscillation cases We select the small Oh number case ($Oh = 0.039$) with oscillation in the post-coalescence: $\rho_h = 1840kg/m^3$, $\rho_l = 1.28kg/m^3$, $\mu_h = 2.02 \times 10^{-3}kg/(m \cdot s)$, $\mu_l = 1.74 \times 10^{-5}kg/(m \cdot s)$, $\sigma = 3.2 \times 10^{-2}N/m$, to conduct a convergence check as the coalescence with oscillation (smaller Oh number) takes longer time and has richer dynamics. Figure 4.3(a) shows the time evolution of the vertical axis, D_y, defined as the vertical distance from the bubble center to the top interface, as illustrated in Figure 4.3(b). As shown in Figure 4.3(a), we select the maximum D_y as amplitude and the time between the first two successive peaks as time period. By increasing the spatial

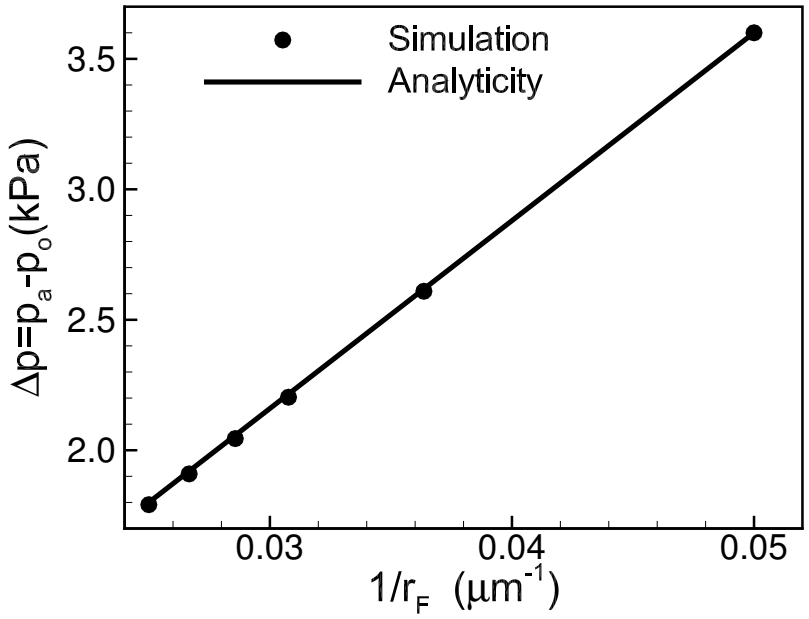

Figure 4.2: Pressure difference across the diffusive interface $\triangle p$ vs. inverse of radius $(1/r_F)$ via simulation (symbols) and Laplace theory (solid line).

resolution from 100×100 to 900×900 with six levels, we list the corresponding peak amplitude and the time period in Table 4.2, in which the third and fifth columns show the relative difference between two successive resolutions respectively. The spatial convergence is clearly seen in these two columns. The whole process of the time evolution of D_y has also shown in Figure 4.4. Taking all of them into consideration, we select the spatial resolution of 800^2 to conduct the parametric study in this section, unless otherwise indicated.

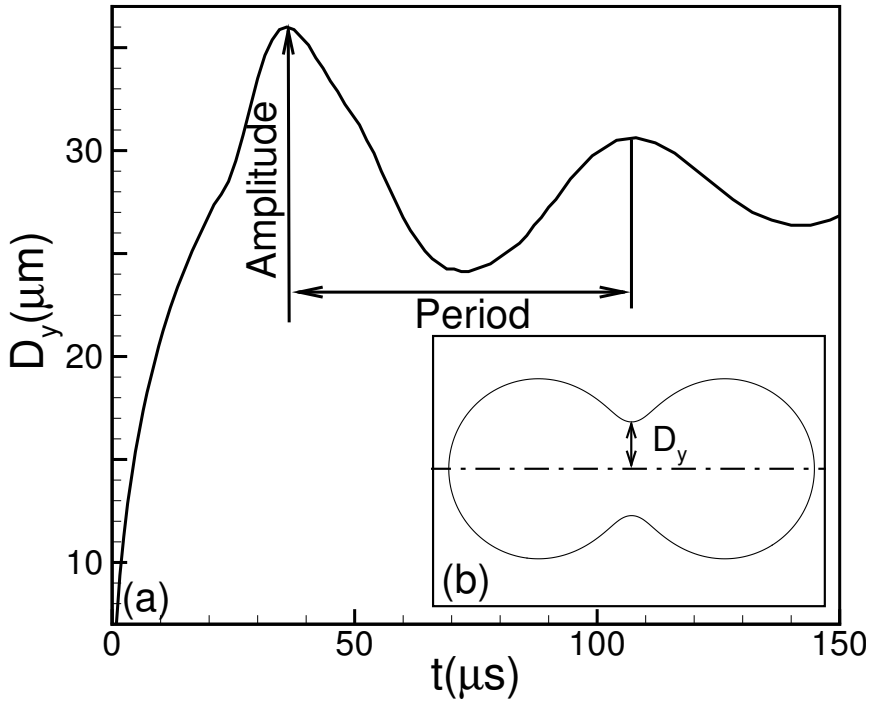

Figure 4.3: (a) Time evolution of half vertical axis (D_y), the distance from top point position to centreline (b), in the coalescence of two equal microbubbles. The maximum D_y and the time between the first two successive peaks are defined as amplitude and time period of the oscillation respectively.

Mesh	Period(μs)	Relative difference Period	Amplitude(μm)	Relative difference Amplitude
100×100	72.0		33.0	
200×200	66.4	7.78%	34.8	5.17%
400×400	65.4	1.51%	35.4	1.69%
600×600	64.8	0.92%	35.8	1.11%
800×800	64.6	0.31%	36.0	0.56%
900×900	64.6	0%	36.0	0%

Table 4.2: Convergence check through amplitude and period defined in Figure 4.3(a).

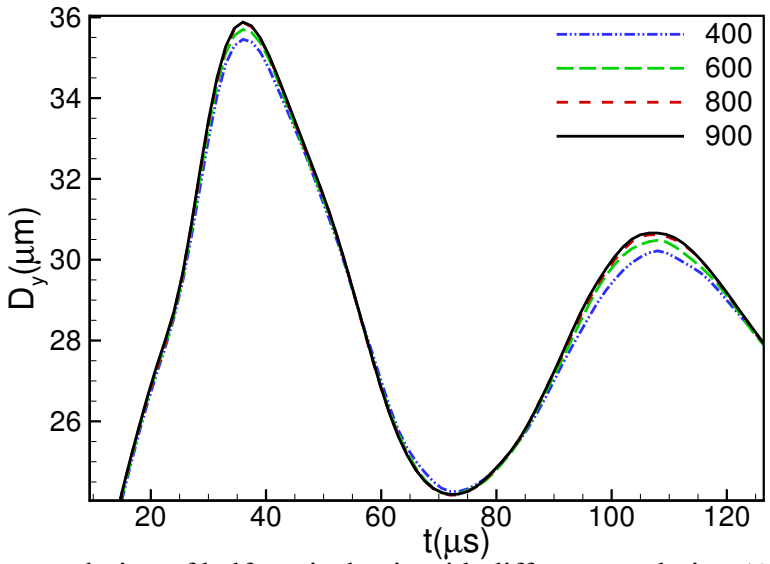

Figure 4.4: Time evolution of half vertical axis with different resolution 400×400, 600×600, 800×800, 900×900

4.4 Two distinct phenomenon of bubble coalescence

As schematized in Figure 4.5, D_x and D_y are the distances between the bubble edge and the mass center O in the horizontal and vertical directions respectively. A shape factor, defined as $\Delta = D_y/D_x$, is to track the interface of the coalescing bubble, starting from 0 (initial touched bubble) and ending at 1 (single coalesced bubble). Switching of the major axis of the coalescing bubble between the horizontal and vertical directions was observed, when the Oh number is relatively small, in the post-coalescence corresponding to the period from (c) to (g) in Figure 4.5. Since the shape factor Δ is reducing, this phenomenon is called damped oscillation. In general, the bubble coalescence can be categorized into three types of damping: underdamping (with a visible oscillation of Δ), overdamping (invisible oscillation of Δ) and critical damping (invisible oscillation with the shortest time to reach $\Delta = 1$).

In order to explore the effects of inertia, viscosity, and surface tension on the bubble coalescence, the dimensionless variable Oh is employed to characterize these effects. When keeping the same density ratio $\rho^* = 1000$ and varying viscosity ratios of $\mu^* = 1361$

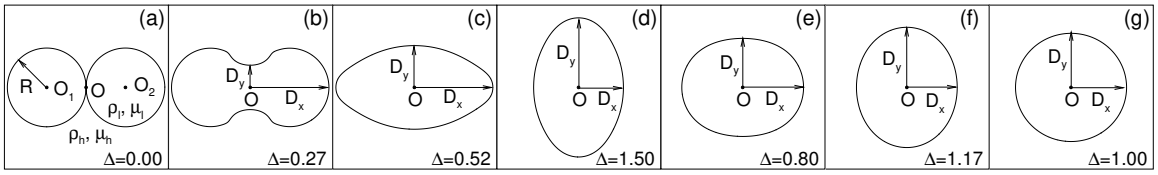

Figure 4.5: A typical microbubble coalescence process with damped oscillation in a microfluidic channel from (a)initially touched bubbles to (b) neck bridge evolution through (c)-(f) oscillation with damping axis ratio toward (g) a coalesced bubble with the minimum surface area. ρ_l/ρ_h and μ_l/μ_h are density and dynamic viscosity of gas/liquid respectively. D_x and D_y are the distances between bubble edge and the mass center O in the horizontal and vertical directions respectively, and $\Delta(= D_y/D_x)$ is the shape factor of the coalescing bubble.

and 100, resulting in Oh numbers 0.530 and 0.039 respectively, we observed two distinct phenomena in the post-coalescence of two equal bubbles, shown in Figure 4.6. For the case of the large Oh number, Figure 4.6(a) ($Oh = 0.530$), the coalescence is quite straightforward from initially two touched parent microbubbles(1), through a successive change of bubble outline, i.e. biconcave ellipse (2), ellipse (3), and nearly circle (4), eventually to a single bubble with the minimal surface area (5). Whereas at small Oh, Figure 4.6(b) ($Oh = 0.039$), the post-coalescence after the neck bridge developed (1) exhibits damped oscillation. The major axis of the coalescing bubble switches between horizontal and vertical directions with a damping amplitude, from (2) to (4), toward the final single round bubble (5).

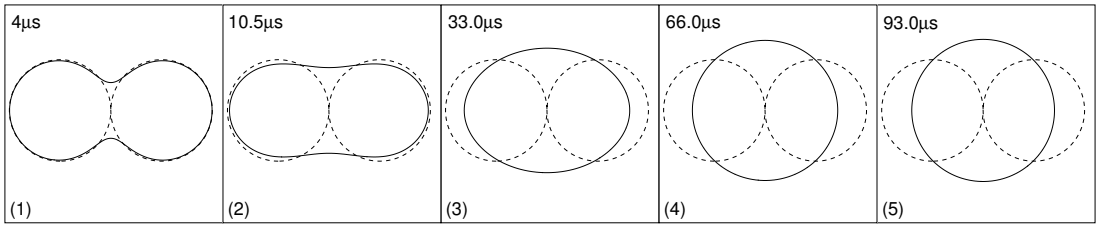

(a) $\mu^* = 1361, Oh = 0.530$

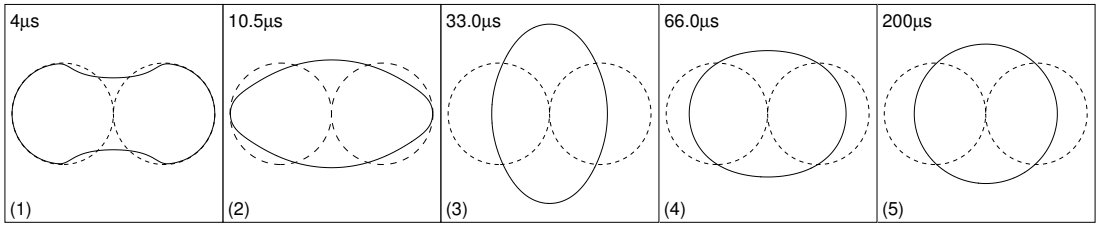

(b) $\mu^* = 100, Oh = 0.039$

Figure 4.6: Two distinct coalescence phenomena indicated by the evolution of the bubble outline at five time instants. (a) $\mu^* = 1361, Oh = 0.530$ and (b) $\mu^* = 100, Oh = 0.039$. Except for the viscosity ratio, computational setup and physical properties are identical, density ratio $\rho^* = 1000$. The bubble outline is determined by the composition contour line $C = 0.5$ inside the interface.

Hence, when and how a damped oscillation occurs during a coalescence is investigated through a systematic study. Table 4.3 shows the sixteen cases with identical physical and computational conditions except for the fluid viscosity μ_h and corresponding different Oh numbers. Figure 4.7 shows the time evaluation of the shape factor, $\Delta(= D_y/D_x)$, of 5 representative cases with $Oh = 0.039, 0.177, 0.477, 0.675$, and 0.964. The Oh value clearly affects the coalescence style. On one side when $Oh < 0.477$, the blue lines with solid symbols exhibit damped oscillation, indicating the axis switching of the coalescing bubble between horizontal and vertical directions with reducing the amplitude of Δ toward a final circular bubble. The smaller the Oh number, the stronger the oscillation. On the other side when $Oh > 0.477$, the green lines with empty symbols show asymptotic growth of the shape factor toward the end of the coalescence when $\Delta = 1.0$, implying that the coalescing bubble retains its major axis on the horizontal direction in the entire process of coalescence with no oscillation. In between, $Oh = 0.477$ serves as the dividing edge for the two distinct coalescence styles.

Another effect of Oh numbers on bubble coalescence is the coalescence time, denoted as T in μs, from two equal, initially-touched bubbles to finally one circular bubble when the minimum surface area, no matter with or without oscillations, as shown in Figure 4.8. When the Oh number is small (in blue) where damped oscillation is involved, increasing the Oh number can significantly reduce the coalescence time T. Whereas when the Oh number is large (in green) with no oscillation, increasing that Oh number causes larger T meaning longer coalescence process. For the Oh resolution selected in this study, there

Case	1	2	3	4	5	6	7	8	9	10	11	12	13	14	15	16
$\mu_h \times 10^3$ $(kg/m \cdot s)$	2.0	3.5	6.5	9.2	13.7	18.0	21.0	24.7	27.5	35.0	40.0	45.0	50.0	55.0	70.0	80.0
$Oh \times 10$	0.39	0.67	1.25	1.77	2.64	3.47	4.07	4.77	5.30	6.75	7.72	8.68	9.65	10.61	13.51	15.43

Table 4.3: Sixteen cases with identical physical and computational conditions except for the fluid viscosity μ_h, thus different Oh numbers.

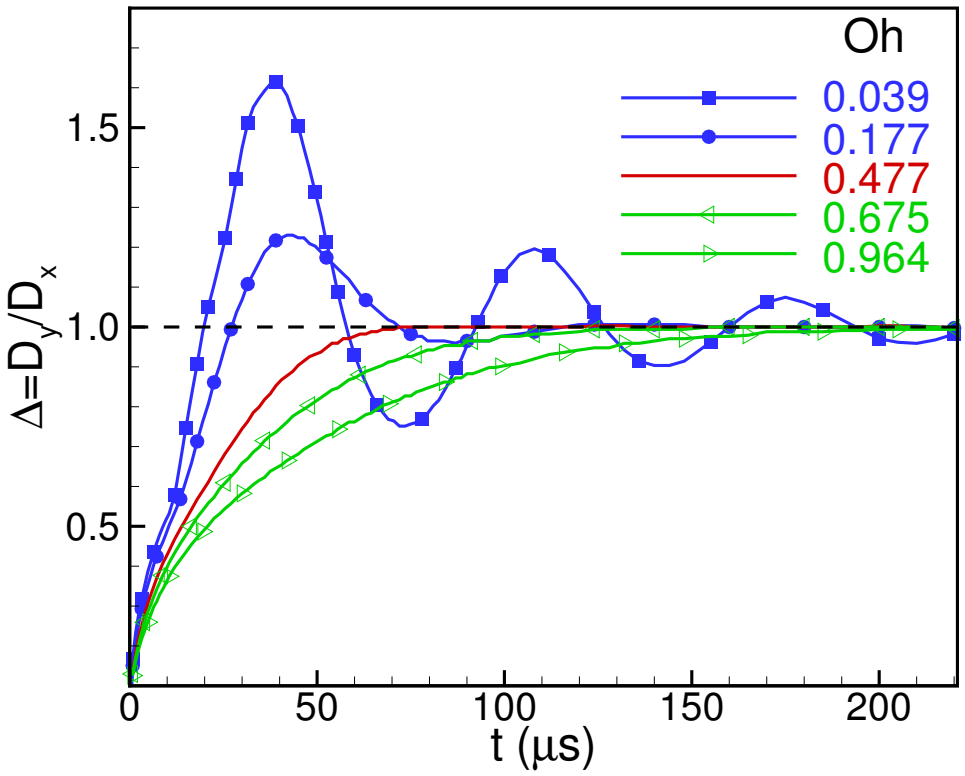

Figure 4.7: Time evolution of shape factor ($\Delta = D_y/D_x$) of 5 representative cases during bubble coalescence. Two distinct coalescence phenomena, with and without oscillations when $Oh < 0.477$ and $Oh > 0.477$ respectively, are identified. $Oh = 0.477$ serves as the dividing edge of them.

exists a critical Oh number, i.e., 0.477 (in red), that corresponds to the shortest coalescence time. If considering a continuous Oh range, the critical Oh number should be identified in the range from 0.407 to 0.530. A similar criterion for droplets was previously discovered, from which the critical Oh number is believed to be between 0.71 to 0.76 [66].

In general, the bubble coalescence can be split into two categories to study the mechanism including $Oh < 0.477$ with oscillation (Sec.4.5) and $0.477 < Oh < 1.0$ without oscillation (Sec.4.6) .

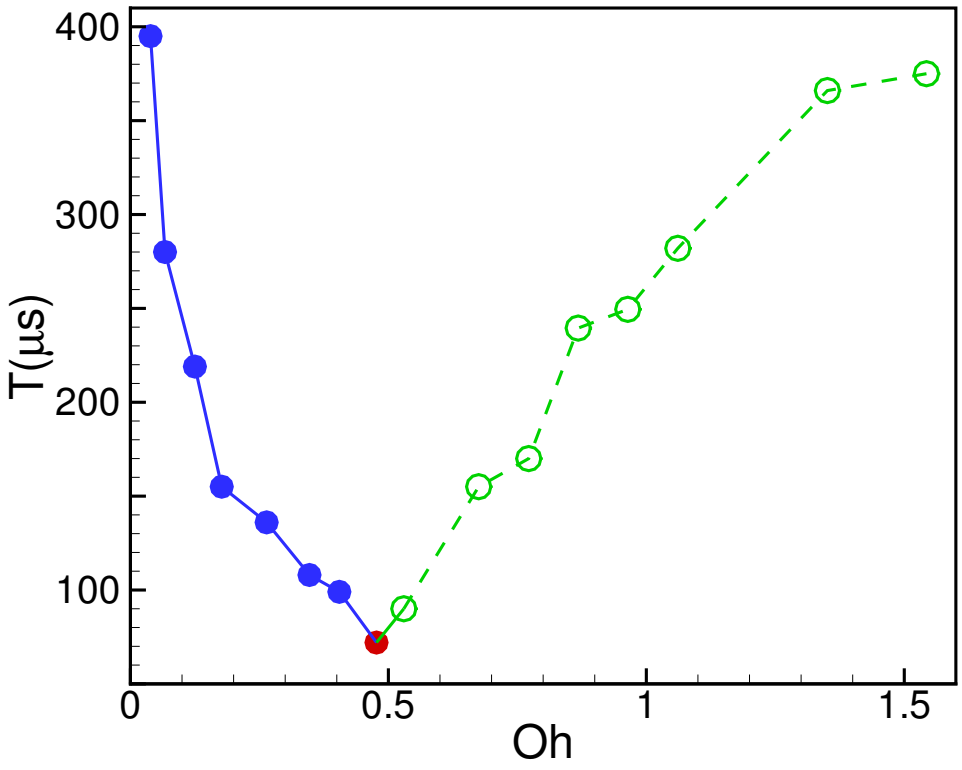

Figure 4.8: Effects of Oh on the bubble coalescence time T. Blue/green lines correspond to small/large Oh ranges. When Oh is small/large, increasing Oh reduces/increases coalescence time. The critical $Oh(= 0.477)$ corresponds to the shortest coalescence time that distinguishes the two distinct coalescence phenomena.

4.5 Mechanism of damped oscillation in microbubble coalescence ($Oh < 0.477$)

We now explore the mechanism behind these two distinct coalescence phenomena in terms of the competition between driving and resisting forces at different Oh ranges. Since, in all the study cases listed in Table 4.3, only liquid viscosity varies, causing the variation of the Oh number while all other parameters remain the same. We only consider the imbalance of surface tension at the interface and viscous resistance from the liquid in this part. Surface energy due to the surface tension can be divided into two parts. One is released to produce kinetic energy to drive the coalescence, which can be called useful energy. The other part

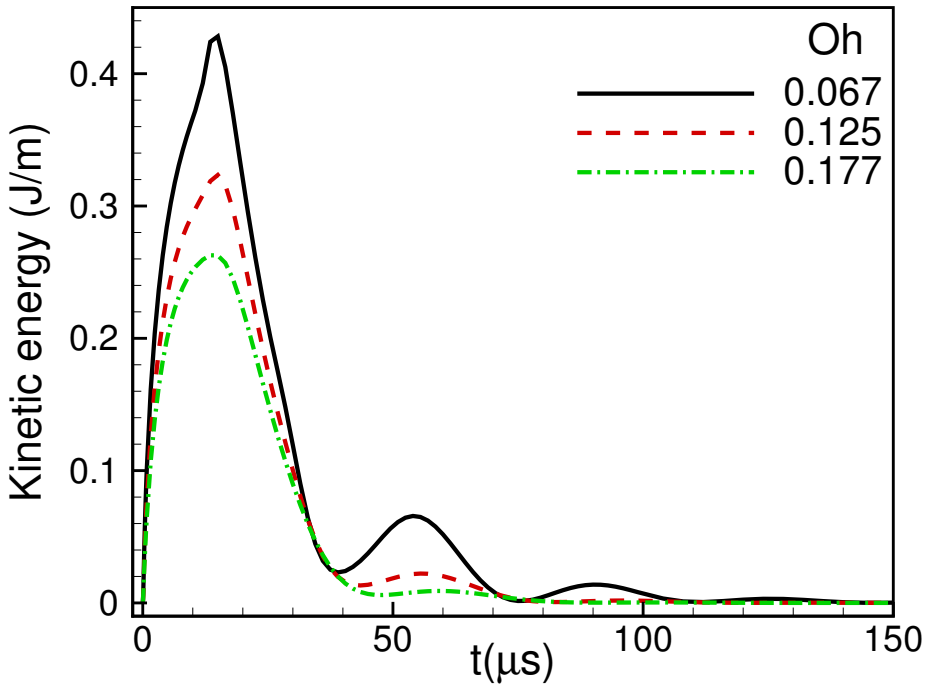

Figure 4.9: Kinematic energy distribution when Oh=0.067, 0.125, 0.177

is dissipated due to the viscous effect. The distribution of kinematic energy with different Oh is shown in Figure 4.9

First, we focus on the left side (in blue) in Figure 4.8. In this regime, the viscosity is relatively small. Thus the coalescence is dominated by surface tension. To better describe the phenomenon, we stick to the top half of the coalescing bubble and the middle point of the interface (called the saddle point). Once the neck is formed, see Figure 4.5(b), the surface tension induces a strong acceleration of the saddle point away from the bubble center, converting surface energy to kinetic energy. As Figure 4.9 shows, the initial acceleration of kinematic energy is similar for different Oh, due to surface energy is fixed for all the cases. When the interface gets flat, the velocity magnitude of the saddle point reaches the maximum as all of the useful surface energy has been converted to the kinetic energy for the interface motion. Due to the inertia, D_y continues to increase, and the interface becomes a convex shape, Figure 4.5(c), generating surface tension. The velocity of the saddle point slows down as the kinetic energy is being converted to surface energy. When all

the useful kinetic energy becomes surface energy, D_y reaches its peak and surface tension gets to the maximum Figure 4.5(d). The process from (c) to (d) illustrates the switching of the major axis from horizontal to vertical directions. The similar transformation between surface energy and kinetic energy occurs to switch the major axis from vertical to horizontal directions, Figure 4.5(d)-(e), in the opposite direction, completing the first cycle of the oscillation. Because of the existence of the energy dissipation, useful energy is losing as Figure 4.9 and the amplitude of D_y is reduced when the saddle point is back to its lowest location. Such cycles repeat with smaller and smaller amplitudes until it reaches the final stable coalesced bubble. In Figure 4.8 and 4.9, it is seen that smaller Oh results in faster growth and a higher peak of Δ. This is because smaller energy dissipation permits more useful surface energy to drive the bubble to coalesce.

If we consider that the surface tension acts as a restoring force, the surrounding fluid acts as a mass, and viscosity damps the motion, the 1-D motion of the saddle point can be modelled as a damped harmonic oscillator [71]

$$A'\rho R^3\frac{d^2D_y^2}{dt^2} + B'\rho\nu R\frac{dD_y}{dt} + C'\sigma D_y = 0 \tag{4.1}$$

where A', B', C' are dimensionless geometric parameters to be determined. The damped oscillation of the saddle point can be derived as the solution of the Equation (4.1)

$$D_y = Ae^{\frac{-B\nu t}{R^2}}sin(C\sqrt{\frac{\sigma}{\rho R^3}}t) \tag{4.2}$$

in which A (integral constant to be determined), $B(=\frac{B'}{2A'}$, and $C(=\sqrt{\frac{C'}{A'}-\frac{B'^2}{A'}\frac{Oh^2}{4}})$ correspond to the amplitude coefficient, decay factor, and the oscillation period respectively. We select three representative cases of $Oh = 0.067$, 0.125, and 0.177, and use the numerical results to determine A, B, and C respectively with the start point $D_y = R_e$. As shown in Figure 4.10, the oscillating trajectories of the saddle point with reduced amplitudes (symbols) are well-captured by the damped harmonic oscillator model (solid lines).

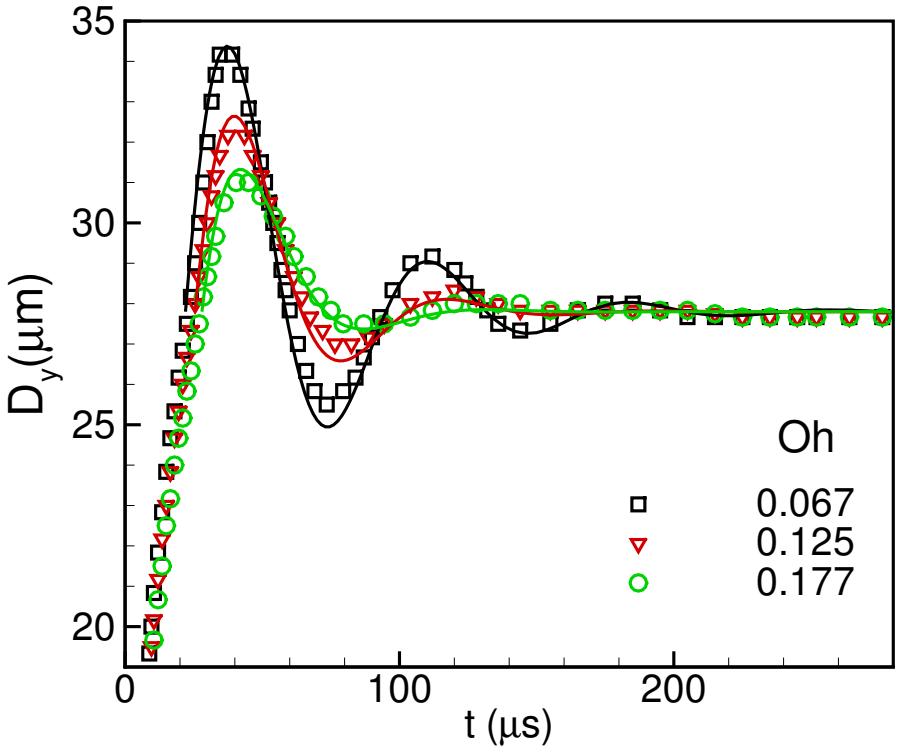

Figure 4.10: The oscillating trajectories of the saddle point, represented by D_y, with reduced amplitudes with $Oh = 0.067$ (black), 0.125 (red), and 0.177(green). Symbols: numerical results; solid lines: analytical solutions of Equation 4.2.

4.6 Spatial/Temporal behaviours for non-oscillation phenomenon (Oh>0.477)

4.6.1 Spatial and temporal scaling of air bubbles in oil

In this work, we simulate coalescence of two unequal air bubbles in oil. To study the inequality effects on the bubble coalescence, twelve cases, among which $\gamma = 1$ is a limited case corresponding to equal-size coalescence are listed in Table 4.4.

The time evolution of bubble coalescence for the case of $\gamma = 1.6$ in Table 4.4 is shown in Figure 4.11. The air-oil interface is depicted by the contour line of $C = 0.5$. The coalescence takes $60\mu s$ evolving from two attached parent bubbles (a) to a coalesced perfect bubble (f) going through asymmetrical dumbbell(b), egg(c), oval(d), and elliptical circle (e) shape.

Case	1	2	3	4	5	6	7	8	9	10	11	12
r_M	3.75	5.0	6.25	7.50	8.75	10.0	11.25	12.50	13.75	15.0	17.50	20.0
γ	5.33	4.0	3.20	2.67	2.29	2.0	1.78	1.60	1.45	1.33	1.14	1.0

Table 4.4: Studied cases of microbubble coalescence noticing $\gamma = 1$ corresponds a limit case of which the parent bubbles are equal.

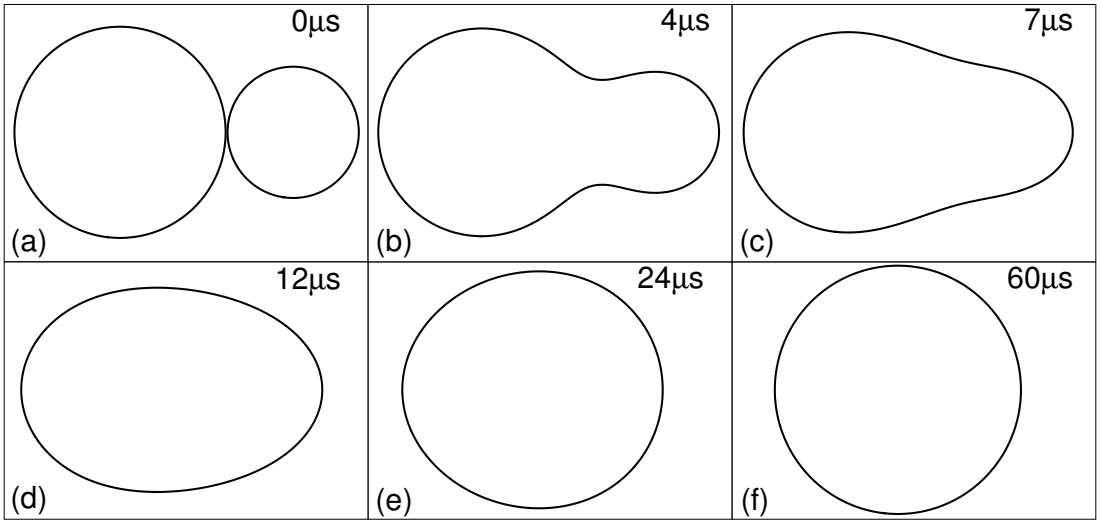

Figure 4.11: Bubble coalescence depicted by the contour line of $\rho = 0.5$ for the case of $\gamma = 1.6$. The coalescence takes $60\mu s$ changing from initially two attached parent bubbles (a) to a coalesced bubble (f) going through asymmetrical dumbbell(b), egg(c), oval(d), and elliptical circle (e) shape.

Figure 4.12 shows bubble coalescence processes in a stacked format with four different γs: (a) 4.0, (b) 2.0, (c) 1.33, and (d) 1.0. In each case, the bubble coalescence process from initially two attached bubbles (black dash line) to finally one perfect coalesced bubble (black solid). Three intermediate stages are denoted by red, green, and pink colors successively. The time is indicated with the same color correspondingly.

While the time evolution of the air-oil interface of each case is seen similar to that shown in Figure 4.11, there are two effects of size inequality on the coalescence. First, the perfected coalesced bubble (black solid line) merged from two unequal parent bubbles

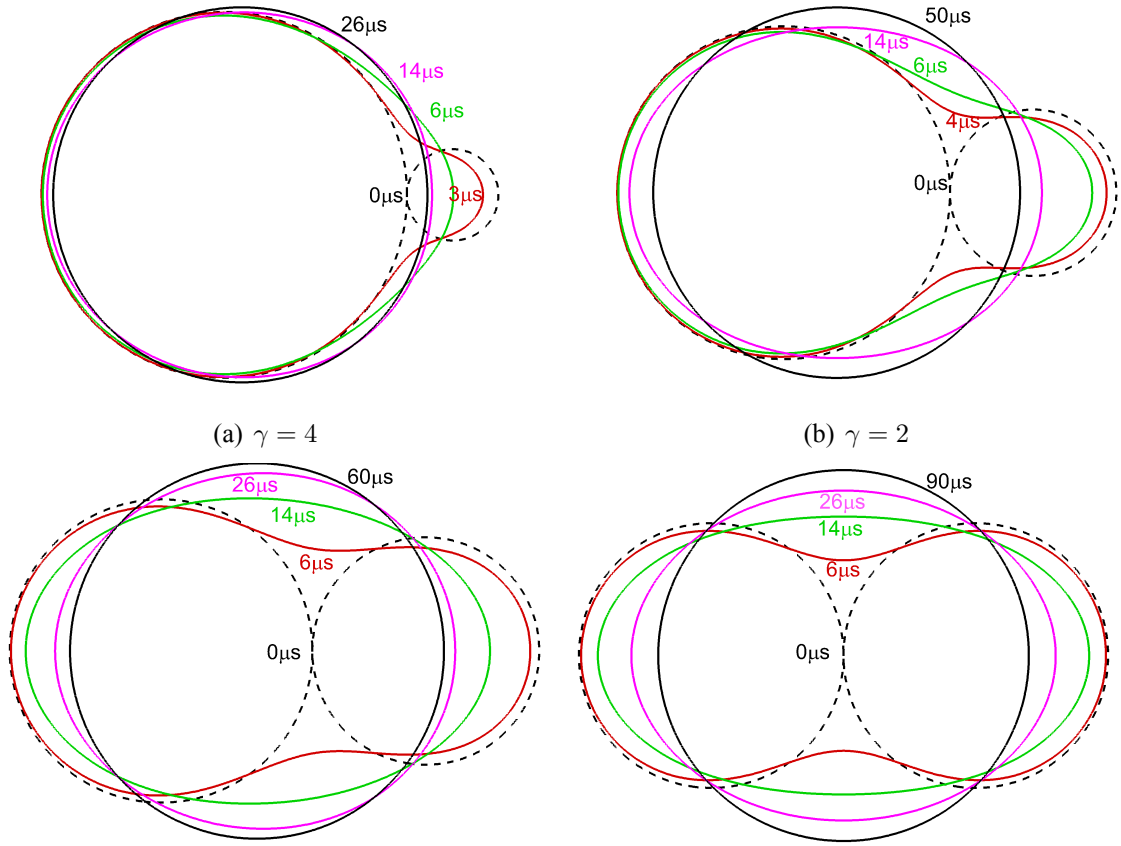

(a) $\gamma = 4$ (b) $\gamma = 2$

(c) $\gamma = 1.33$ (d) $\gamma = 1$

Figure 4.12: (Color online) Coalescence from two attached parent bubbles (black dashed lines) to one perfectly coalesced bubble (black solid line) with four different size ratios of parent bubbles: γ=(a) 4.0, (b) 2.0, (c) 1.33, and (d) 1.0 through stacked contour lines of $\rho = 0.5$ at representative time instants. The initial (before coalescence) and final (fully merged) water-air interfaces are recognized by the black dashed and solid lines. Three intermediate shapes evolving successively are denoted in red, green, and pink respectively. The coalescence time, seen as (a) $26\mu s$, (b) $50\mu s$, (c)$60\mu s$, and (d) $90\mu s$, increases when γ decreases.

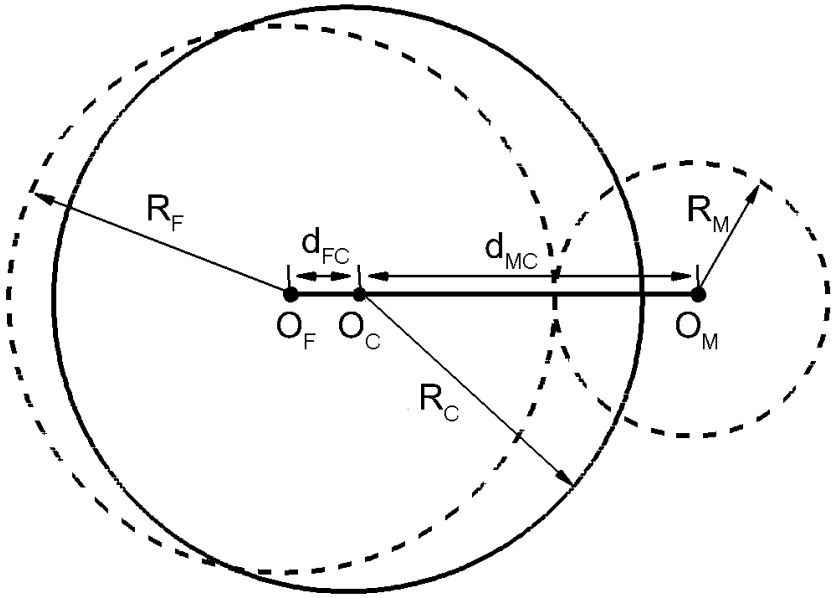

Figure 4.13: Schematics of coalescence geometry between before (dashed line) and after (solid line) coalescence.

(black dashed lines) tends to locate closer to the father bubble. This phenomenon is so called *coalescence preference*, recently observed in experiments [69, 70]. The preference can be quantified by the relative distance ratio of $\chi = d_{FC}/d_{MC}$, in which d_{FC} and d_{MC} are the distances of the centers of father bubble (O_F) and mother bubble (O_M) to coalesced bubble respectively, as schematized in Figure 4.13. As obtained in the experiments, the preferential distance ratio χ exhibits power-law relationship to the size inequality as $\chi \sim \gamma^{-p}$. Such a spatial power-law scaling is captured in the current numerical study. In Figure 4.14, red and green symbols are experimental results from Figure 4 in [70] and Figure 2 in [69] respectively, and black symbols are from the current simulation. Power-law fitting of the three data sets result in $p = 3.992$ (red [70]), 2.152(green [69]), and 1.794 (black).

The discrepancies among the three scaling are due to the different fluids and different set-ups between experiments and current simulation. Another major reason is the 2D simulation. If 3D bubbles are taken into consideration, the power-index of spatial scaling is close to 3, which can be derived from the center of mass theory [70]. However, the temporal

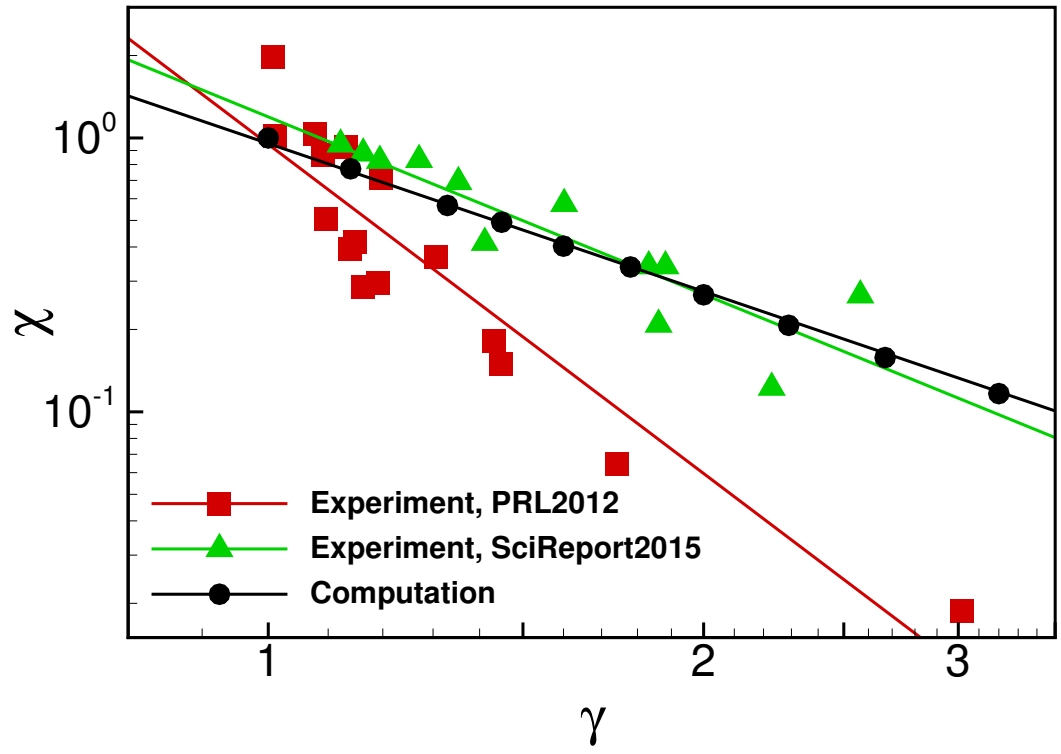

Figure 4.14: (Color online)Power-law spatial scaling of $\chi(= d_L/d_S) \sim \gamma^{-p}$ in log-log scale. Symbols are experimental and simulation results and lines are power-law fitting corresponding the same color. $p = 3.992$ (red), 2.152 (green), and 1.794 (black, current simulation).

scaling of 2D and 3D simulation is very similar. This investigation will be a very interested hypothesis to be verified through more cases.

As seen in Figure 4.11 and 4.12, larger γ corresponds to faster coalescence. The equal size case shown in Figure 4.12(d) takes the longest time, i.e. $T = 90\mu s$, to complete its coalescence while the largest inequality case, $\gamma = 4$ (Figure 4.12(a)), takes to shortest time, $T = 21\mu s$, to complete the coalescence. It is found that the coalescence time T from two-parent bubbles to a coalesced perfect bubble also exhibits a power-law relationship to the size inequality as $T \sim \gamma^{-q}$, as shown in Figure 4.15. The solid line is the trendline fitted by power-law for the symbols obtained from the simulation with $q = 0.899$, $R^2 = 0.9955$. Such a power-law relationship is believed to be the first time observation.

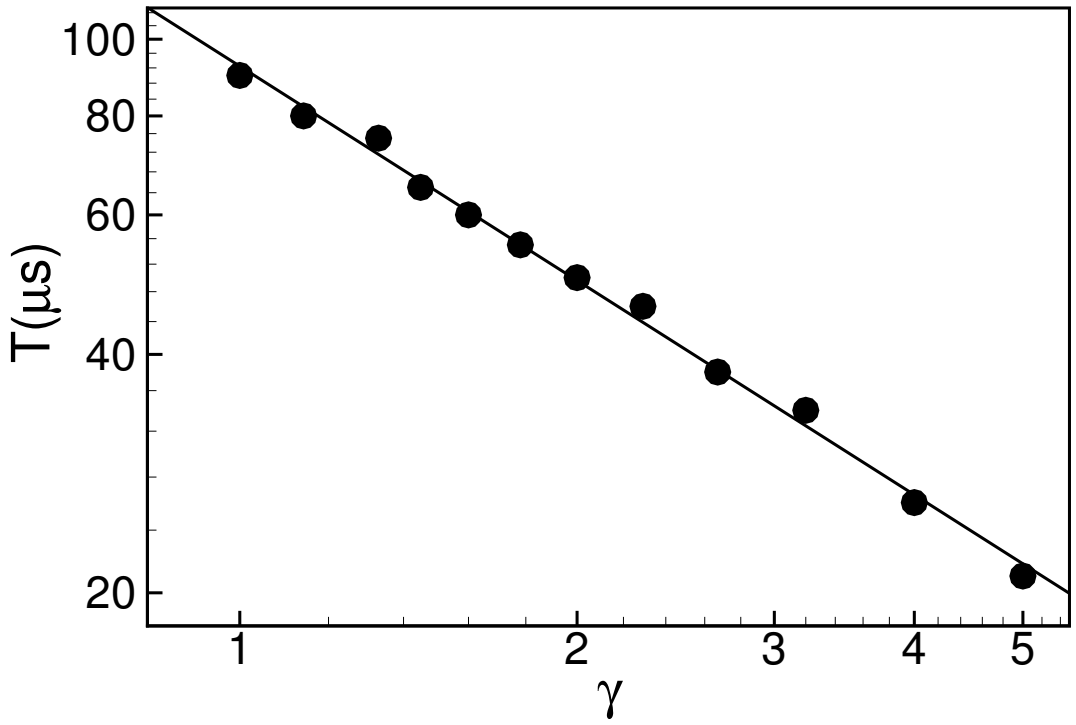

Figure 4.15: Power-law temporal scaling of $T \sim \gamma^{-q}$ in log-log scale. Symbols are simulation results, and the line is from a power-law fitting with $q = 0.899$ and $R^2 = 0.9955$.

Dynamics of air bubble coalescence in the oil

To understand the underlying physics behind the power-law spatial and temporal scaling of bubble coalescence, we look into the time evolution of coalescence for the case of $\gamma = 1.6$. The coalescence in terms of the air-water interface evolution has been shown and interpreted in Figure 4.11. Figure 4.16 and 4.17 show the pressure and velocity fields at (a) $t = 4\mu s$, (b) $9\mu s$, and (c) $24\mu s$. Shortly after the two parent bubbles are attached, i.e. (a) $t = 4\mu s$, the interface exhibits an asymmetrical dumbbell shape with a neck at the location where the two parent bubbles were originally attached. Large pressure at both edges of the father and mother bubbles and the small pressure at the neck (Figure 4.16(a)) is seen, and the pressure difference between the edge and neck is large. Air swarms from two edges toward the neck in the horizontal direction, stronger from the mother bubble side than the father. These two streams meet and interact inside the neck, spouting the flow along both sides in the vertical direction (Figure 4.17(a)). Two pairs of attached and opposite vortices are formed at the top and bottom interface, respectively. Such a flow pattern stretches the neck in an opposite direction vertically, more on the mother bubble size than the father. At an intermediate time, $t = 9\mu s$, the asymmetrical dumbbell shape has been stretched as an egg shape with a tip and a base at left and right respectively. Higher pressure is developed at both the tip and base end, but the pressure difference between the two ends drops (Figure 4.16(b)). As seen in Figure 4.17(b), air continues to flow face to face horizontally, stronger from the tip side than the base side.

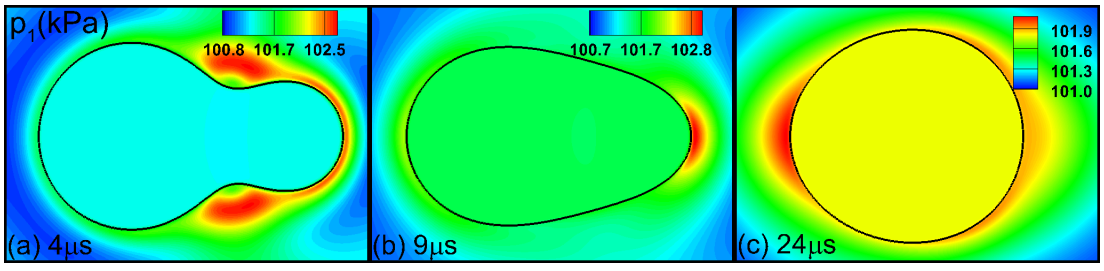

Figure 4.16: (Color online) Dynamics pressure fields at three representative time instants in the bubble coalescence for the case of $\gamma = 1.6$:(a)$t = 4\mu s$, (b)$t = 9\mu s$, and (c)$t = 24\mu s$.

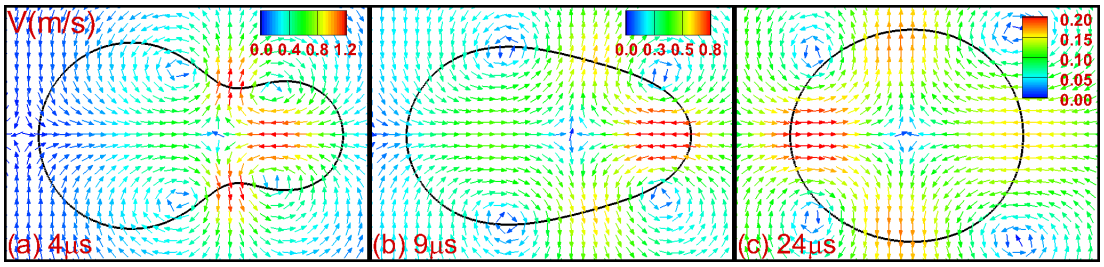

Figure 4.17: (Color online) Velocity vector fields at three representative time instants in the bubble coalescence for the case of $\gamma = 1.6$: (a)$t = 4\mu s$, (b)$t = 9\mu s$, and (c)$t = 24\mu s$. The legend indicates the velocity magnitude ($V = \sqrt{u_x^2 + u_y^2}$). The uniform vector arrows only show the flow direction.

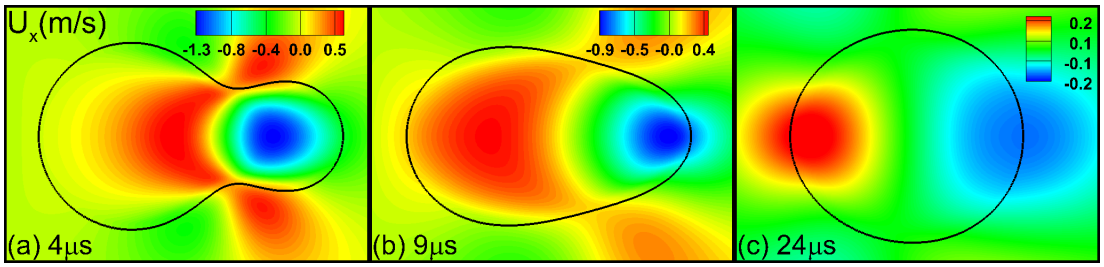

Figure 4.18: (Color online) Horizontal-component velocity (u_x) fields at three representative time instants in the bubble coalescence for the case of $\gamma = 1.6$: (a)$t = 4\mu s$, (b)$t = 9\mu s$, and (c)$t = 24\mu s$. The legend indicates the magnitude and direction of u_x. Red means flowing to right and blue means to left.

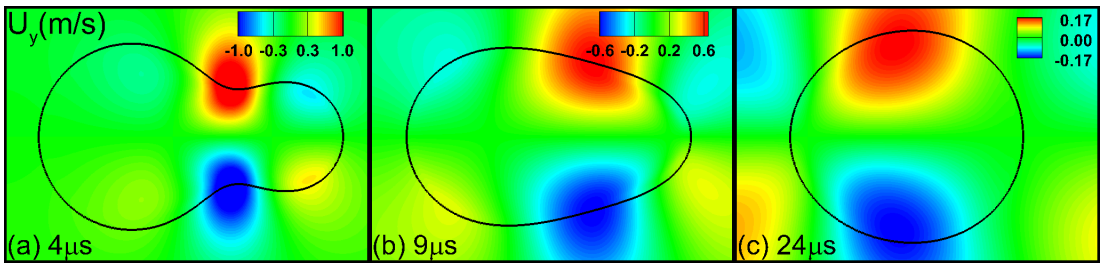

Figure 4.19: (Color online) Vertical-component velocity (u_y) fields at three representative time instants in the bubble coalescence for the case of $\gamma = 1.6$: (a)$t = 4\mu s$, (b)$t = 9\mu s$, and (c)$t = 24\mu s$. The legend indicates the magnitude and direction of u_y. Red means flowing down and blue means up.

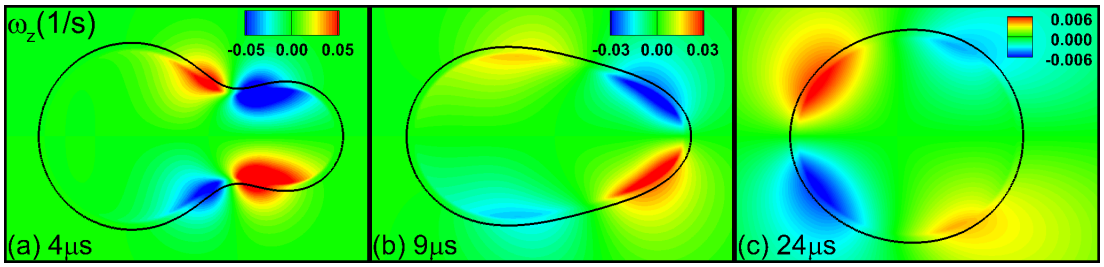

Figure 4.20: (Color online) Vorticity ($\omega = \partial u_y/\partial x - \partial u_x/\partial y$) fields at three representative time instants in the bubble coalescence for the case of $\gamma = 1.6$:(a)$t = 4\mu s$, (b)$t = 9\mu s$, and (c)$t = 24\mu s$. The legend indicates the magnitude and direction of ω. Red means anti-clockwise rotation and blue means clockwise rotation.

The location where horizontal flow streams meet and vertical streams leave are moved to the left. The opposite vortices at the top and bottom move apart to the tip and base area. Due to the unbalanced pressure and flow in horizontal direction, the interface is still stretched along the vertical direction stronger in the tip than the base side, reducing the curvature difference of the tip and base of the egg. At a later time, $t = 24\mu s$, additional larger pressure is developed at the farmost horizontal interface with vanishing difference (Figure 4.16(c)). The interface appears as an elliptical circle with similar curvature horizontally (Figure 4.17(c)). Two vortex pairs are formed similarly in both horizontal and vertical directions. Horizontal streams meet at the center of the bubble and leave along both sides of

vertical direction with similar velocity. The interface is further stretched along both sides of vertical direction toward minimum surface energy. Figure 4.18, 4.19, and 4.20 provide the quantitative information regarding to the flow of dynamics in the coalescence.

4.6.2 General power-law temporal scaling for unequal size bubble coalescence

Is the power-law temporal scaling investigated when air bubble in the oil suitable for other cases as $Oh > 0/477$. In this part, we show numerical results for unequal air bubbles coalescence in various liquids and address if the power-law temporal scaling is general and how the liquid phase affect the temporal scaling. To perform an effective parametric study, we fix the density and viscosity of gas phase as $\rho_l = 1.28kg/m^3$ and $\mu_l = 1.74 \times 10^{-5}kg/(m\mathring{u}s)$ and surface tension as $0.032N/m$ and vary the liquid density (ρ_h) and viscosity (μ_h) from $448 \sim 1482(kg/m^3)$ and $0.0111 \sim 0.0237(kg/(m \cdot s))$, respectively, resulting twelve cases with the Oh number in the range of $0.509 \sim 0.989$. Thus, overdamping is involved in the post-coalescence. The detail information is seen in Table 4.5. The parent bubble size inequalities are chosen $\gamma = 4, 3, 2, 1.5, 1.2, 1$, in which $\gamma = 1$ corresponds to the equal size parent bubble case. The Oh number is the ratio of

Case	1	2	3	4	5	6	7	8	9	10	11	12
Oh	0.509	0.522	0.577	0.602	0.638	0.654	0.654	0.705	0.774	0.800	0.872	0.946
$\rho_h(kg/m^3)$	896	1408	1152	640	1408	896	1480	1152	640	896	1152	640
$\mu_h \times 10$ $(kg/m \cdot s)$	0.122	0.157	0.157	0.122	0.191	0.157	0.201	0.191	0.157	0.191	0.237	0.191

Table 4.5: Twelve study cases varying liquid density and viscosity with fixed gas density, gas viscosity, and surface tension, resulting in the Oh number from 0.509 to 0.946.

viscous force versus inertial and surface tension forces. To explore the effects of the liquid phase, we first fix the surface tension. As indicated in the review paper for the coalescence of drops [46], when $Oh << 1$, the viscous effect is insignificant and the coalescence is dominated by inertial force. When Oh becomes of order unity, the inertial effect becomes insignificant and the coalescence is dominated by viscous force. For these two ends in the

Oh spectrum, two characteristic time scales [49] have been introduced: $t_i = \sqrt{\rho_h r_F^3/\sigma}$ and $t_v = \mu_h r_F/\sigma$ as inertial and viscous time scale respectively. In between, i.e. $0.2 < Oh < 1$, both inertial and viscous forces contribute to the resisting force in the coalescence process and t_i and t_v have approximately the same order. In the current study, the Oh number ranges from 0.5 to 1.0. We use t_i to normalize the coalescence time.

Figure 4.21 shows the numerical result (symbols) of normalized coalescence time T^* as a function of size inequality γ with three different Oh numbers. In each case, power-law temporal scaling $T^* = A_0\gamma^{-n}$ (fitting line) is exhibited with the standard deviation and correlation of numerical results vs. the fitting line are 0.115 and 0.999, 0.013 and 0.998, and 0.011 and 0.999 for Oh =0.509, 0.638, and 0.8 respectively. The corresponding 95%

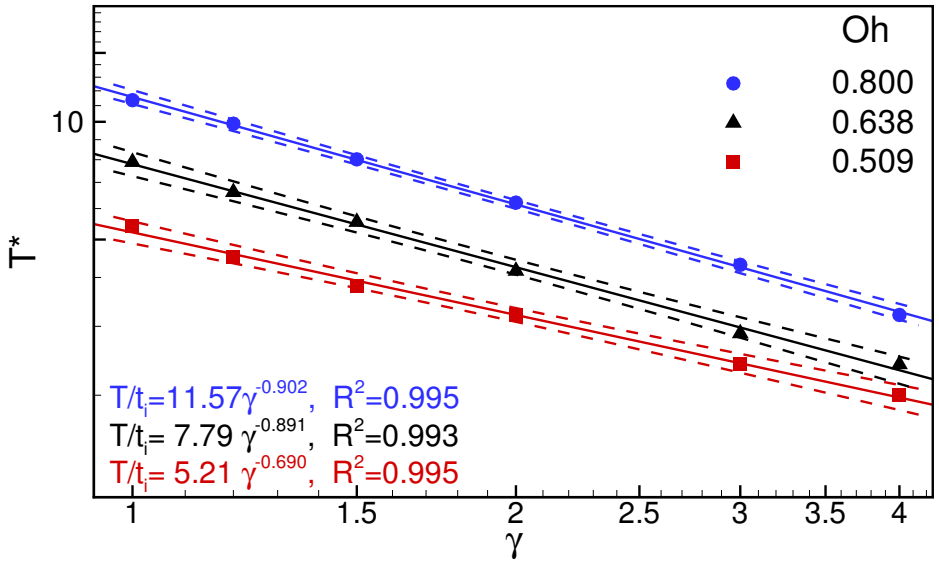

Figure 4.21: Power-law temporal scaling of unequal size microbubble coalescence with four different Oh numbers corresponding to cases 1, 5, and 10 in Table 4.5. Symbols: numerical results; lines:power-law fitting. The standard deviation and correlation of numerical results and the fitting line are 0.115 and 0.999, 0.013 and 0.998, and 0.011 and 0.999 for Oh =0.509, 0.638, and 0.8 respectively. The corresponding 95% confidence band (dashed line) for each Oh case is shown.

confidence bands (dashed lines) are shown, respectively. From bottom up, the prefactor (A_0) and power index (n) change as the Oh number increases. It is noticed that the surface tension of these four cases stays the same ($\sigma = 0.032N/m$). Thus, this result indicates that the power-law temporal scaling is affected by the liquid phase characterized by the Oh number.

Closely looking into the 12 cases, we show the quantitative effects of the Oh number on A_0 and n in Figure 4.22 with symbols from the simulations. In the upper panel, the prefactor A_0 shows a linear relation with Oh for the entire Oh range, the standard deviation numerical results from the fitting line is 0.21. And the corresponding correlation factor between them is 0.997. Whereas in the bottom panel, the power index n is linear to Oh when $Oh < 0.66$, with standard deviation and correlation factor 0.002, and 0.996 respectively and remains approximately a constant (0.9) when $Oh > 0.66$ with a standard deviation of 0.0022. On both plots, the dashed lines represent the 95% simultaneous confidence band, respectively. From Figure 4.22, we can derive the following relationship between the normalized global coalescence time T^* and inequality γ of parent bubbles parameterized by Oh as

$$T^* = A_0\gamma^{-n} \tag{4.3}$$

with

$$n = \begin{cases} 1.35Oh + 0.01 & : 0.5 < Oh < 0.66 \\ 0.9 & : 0.66 < Oh < 1.0 \end{cases}$$

This formulation indicates the existence of a general power-law scaling of microbubble coalescence in the range of Oh from 0.5 to 1.0. Noticing the definitions of $Oh(=\eta_h/\sqrt{\rho_h\sigma r_F})$ and $t_i(=\sqrt{\rho_h r_F^3/\sigma})$, we explore the physical insights of the general temporal scaling, i.e. Eq. 4.3, in what follows.

From Equation 4.3, we obtain $A_0 = T^* = 21.2Oh - 5.6$ when $\gamma = 1$, meaning that the prefactor of the power-law scaling is the normalized coalescence time of two equal-size

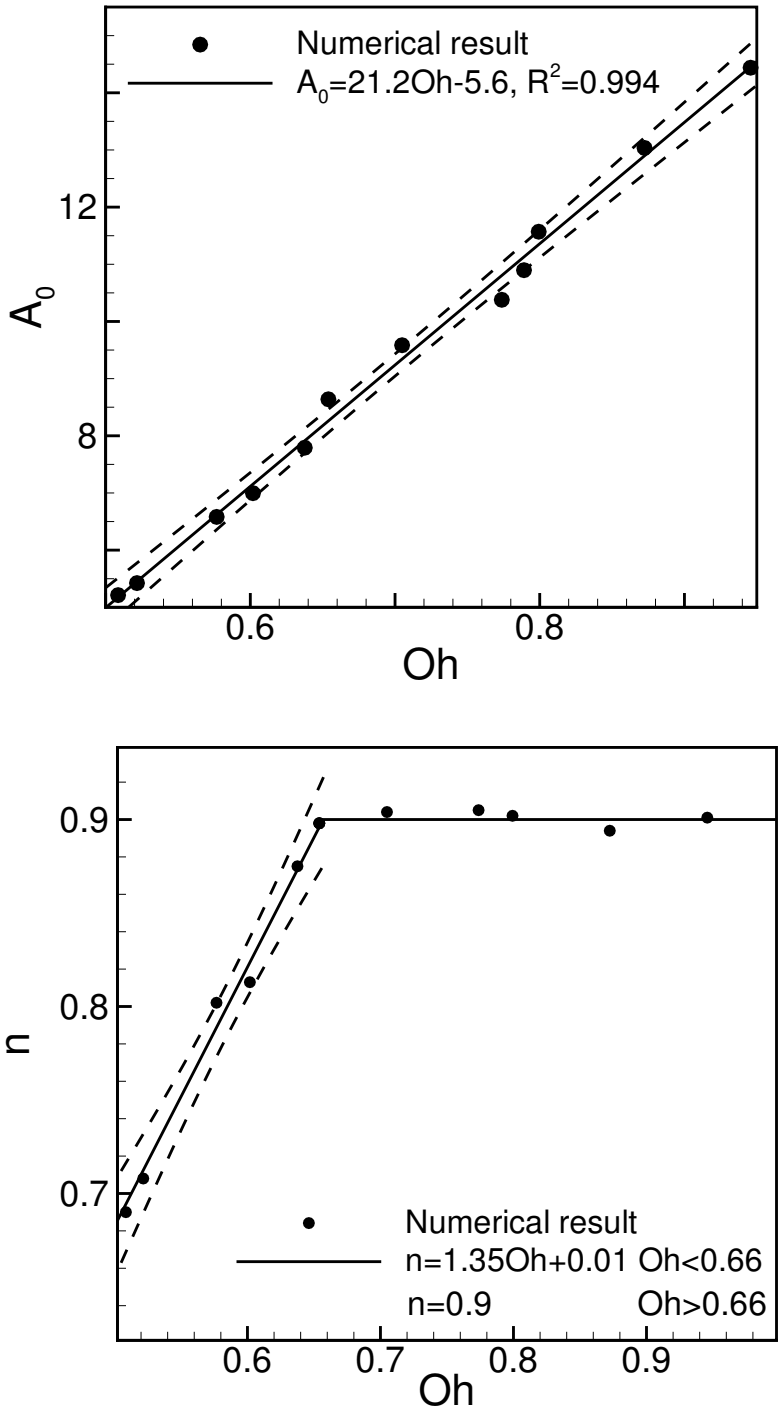

Figure 4.22: Effects of Oh number on prefactor (A_0), top panel, and power index (n), down panel with R^2=0.983, in the temporal power-law scaling. Symbols: numerical results; lines: fitting

bubbles, which is linear to Oh. The power index n is determined by $dT^*/d\gamma$ at $\gamma = 1$. Corresponding to two ranges of Oh in Equation 4.3, we have

$$\left.\frac{dT^*}{d\gamma}\right|_{\gamma=1} = \begin{cases} 28.38(Oh)^2 - 7.35Oh - 0.06 & : 0.5 < Oh < 0.66 \\ 19.08Oh - 5.04 & : 0.66 < Oh < 1.0 \end{cases} \tag{4.4}$$

Showing that the quickness of the coalescence from equal to unequal size bubble coalescence is determined by Oh. These behaviors might be understood from the following aspects. First, size inequality γ reflects the initial driven mechanism, generated by the imbalanced surface tension forces on the parent bubbles, of the bubble coalescence. Larger imbalance of surface tension forces generates stronger inertia, resulting in shorter global coalescence time. Second, when γ is fixed, larger Oh means stronger viscous effects in the liquid, leading to longer global coalescence time. These two effects can be seen in Fig. 4.21. Third, when the Oh number is relatively large, the viscous effect from liquid dominates the coalescence whereas the initially imbalanced surface tension forces and generates inertia become insignificant, which leads to a constant power index.

Since the temporal scaling of microbubble coalescence is rarely addressed in open literature, we select 11 new cases (Table 4.6), varying the fluid density, fluid viscosity, and surface tension, with three Oh numbers: 0.509, 0.654 and 0.800 to evaluate the temporal scaling formula, Equation 4.3.

$Case$	13	14	15	16	17	18	19	20	21	22	23
Oh	0.509	0.509	0.509	0.509	0.654	0.654	0.654	0.800	0.800	0.800	0.800
$\rho_h(kg/m^3)$	1197	896	1000	680	896	448	640	600	680	1482	896
$\mu_h \times 10$ $(kg/m \cdot s)$	0.122	0.149	0.182	0.160	0.111	0.157	0.107	0.111	0.204	0.371	0.271
$\sigma(N/m)$	0.024	0.048	0.064	0.073	0.016	0.064	0.021	0.016	0.048	0.064	0.073

Table 4.6: Eleven cases corresponding to three Oh numbers with the variation of fluid density, fluid viscosity, and surface tension.

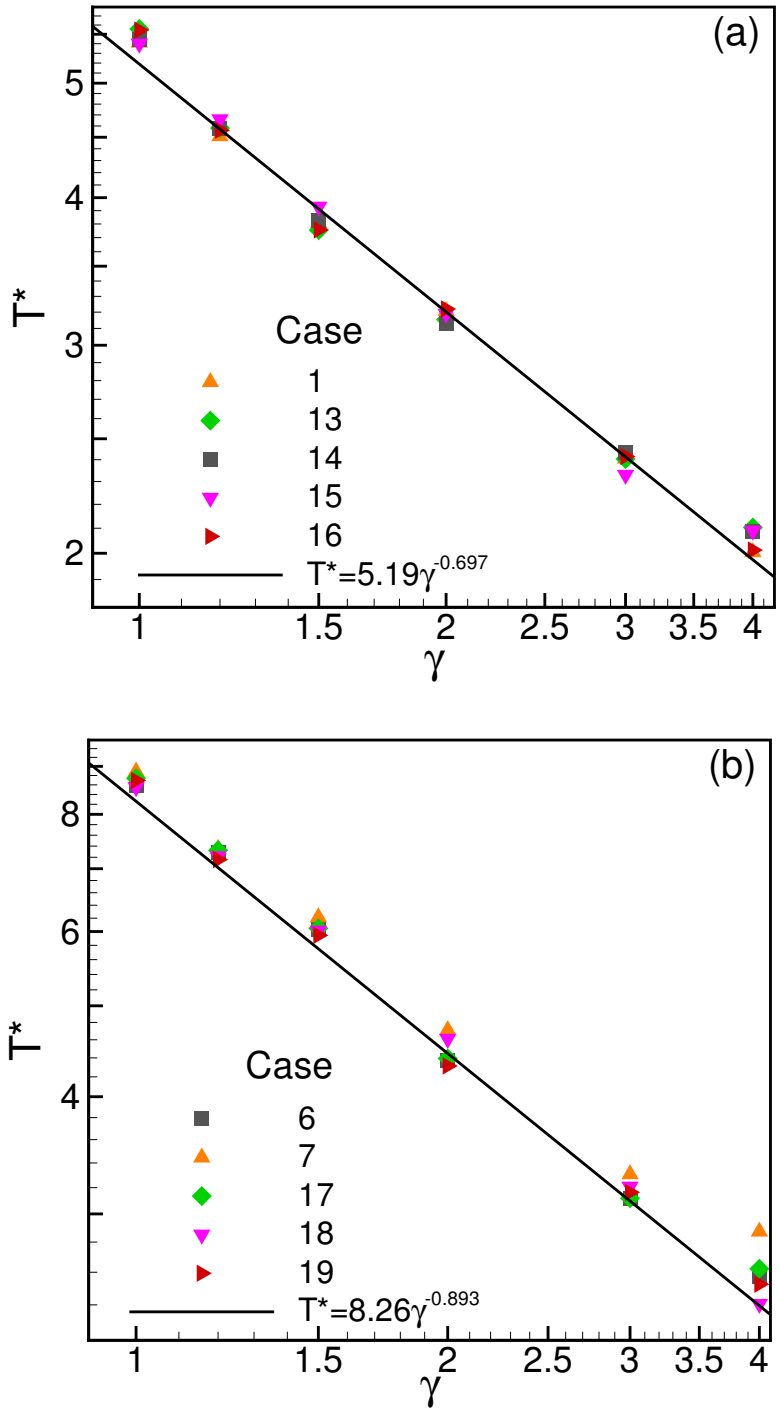

Figure 4.23: General power-law temporal scaling for unequal size air microbubble coalescence at Oh = (a)0.509,(b)0.654, and (c)Oh=0.8. Symbols: simulation results; lines: prediction from Equation 4.3

Figure 4.23: Continued

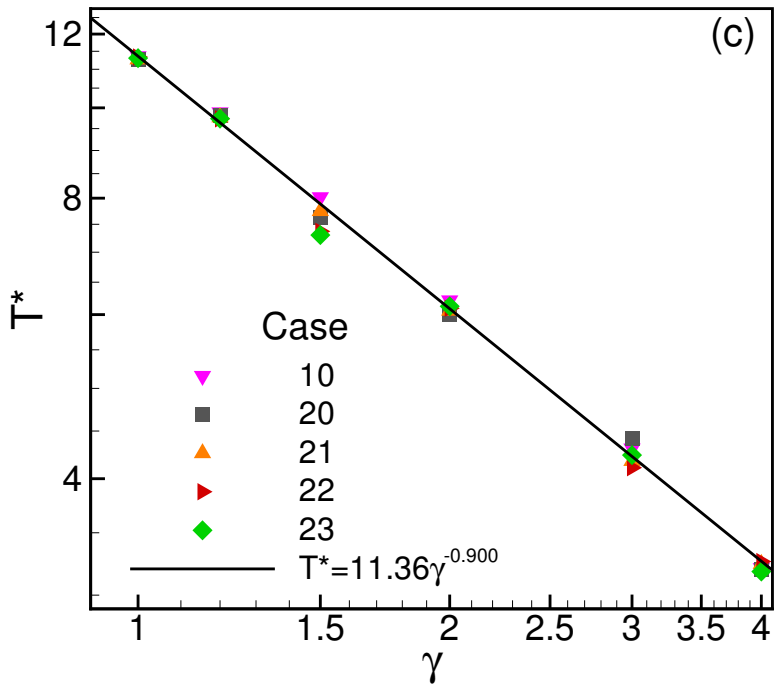

We plot the power-law temporal scaling of unequal size air microbubble coalescence in Figure 4.23. The symbols are simulation results and lines are predicted from Equation 4.3. Correspondingly, Table 4.7 shows the difference between the numerical and predictive results quantitatively.

Corresponding to $Oh = 0.509, 0.654$, and 0.800, Equation 4.3 predicts the power index of the power-law temporal scaling as 0.697, 0.893, and 0.900 respectively. The simulation results agree well with the predictions in each of the three evaluations. Thus, Equation 4.3 is regarded as a general power-law temporal scaling of unequal size air microbubble coalescence.

4.7 Conclusion

Using the GPU-accelerated LBM simulation, we are able to systematically investigate the effects of Oh number on the global coalescence process in a microchannel. Sixteen

$Case$	Oh	Prediction (Equation 4.3)		Check cases		Relative error	
		A_0	n	A_0	n	$A_0(\%)$	$n(\%)$
13	0.509	5.19	0.697	5.23	0.690	0.77	-1.00
14				5.28	0.703	1.73	0.86
15				5.27	0.709	1.54	1.72
16				5.21	0.684	0.39	-1.87
17	0.654	8.26	0.893	8.59	0.897	4.00	0.45
18				8.60	0.908	4.12	1.68
19				8.50	0.893	2.91	0
20	0.800	11.36	0.900	11.28	0.893	-0.70	-0.78
21				11.33	0.903	-0.26	0.33
22				11.2	0.901	-1.41	0.11
23				11.2	0.901	-1.41	0.11

Table 4.7: The comparison between eleven cases from Table 4.6 and the prediction from Equation 4.3

cases with the Oh number from 0.039 to 1.543, by varying the liquid viscosity from 0.0020 to $0.08\ kg/(m \cdot s)$ while keeping other parameters unchanged, are studied. By tracking the time evolution of the shape factor Δ, we identified two distinct coalescence phenomena. In the region of $Oh < 0.477$, damped oscillation is observed. The oscillation is more intensive when Oh is smaller, and resulting a longer time to complete the global oscillation. While $Oh > 0.477$, the shape factor asymptotically increases from 0 to 1 and the global coalescence time increases with the increase of Oh. In between the two regimes, a critical $Oh = (0.477)$ number is identified, corresponding to the smallest coalescence time. Strictly speaking, when consider a continuous Oh range, the critical Oh number should fall in the range between 0.407 and 0.530. Such a criterion of with and without damped oscillation determined by Oh number are consistent to the drop coalescence that has presented in open data.

For the oscillation cases, the mechanism behind the different coalescence behavior is explored in terms of the competition of the surface tension driving and viscous resisting. When $Oh < 0.477$, the viscous force is small, thus energy dissipation is insignificant. The bubble coalescence is dominated by the surface tension force. The transformation between the surface energy and kinetic energy with energy dissipation causes the damped oscillation of microbubble coalescence. Smaller Oh number cases possess more useful surface energy to drive stronger oscillation, resulting in longer coalescence time. The damped oscillation can be modeled as a damped harmonic oscillator that has an analytical solution. The numerical simulation has a good agreement with the analytical prediction.

When $Oh > 0.477$, there is no oscillation phenomenon in this range. From a study case that air bubble in the oil, the coalescence preference that the coalesced bubble is located closer to the larger parent bubble is well captured. The preferential location of the coalesced bubble is a function of size inequality, the radius ratio of the father (large) to mother (small) bubble $\gamma = r_F/r_M$. Systematical simulation of 12 cases varying the size inequality γ from 5.33 to 1 results in a power-law relation between the preferential relative distance χ and size inequality γ as $\chi \sim \gamma^{-1.794}$, which is consistent to the recent experimental observations, although the power index is far from the experiment. It is caused by the different set-up and 2D simulations. If we want to find accurate quantitative results related to space, the bubble should be simulated in 3D. Meanwhile, we found that the coalescence time is also correlated to the size inequality through a power-law relation, $T \sim \gamma^{-0.899}$, implying that unequal-size bubbles always coalesce faster than equal-size bubbles and that the larger the size inequality is, the faster they coalesce. Such a temporal scaling of coalescence on inequality size ratio is believed to be a first time observation.

A general power-law time scaling of unequal size microbubble coalescence has been derived when bubble coalescence without oscillation. The physical insights of both prefactor and power index have been well understood:

1. The power-law temporal scaling of unequal size microbubble coalescence $T^* = A_0\gamma^{-n}$ generally exists in the range of $0.5 < Oh < 1.0$, where no oscillation is involved in the post-coalescence.

2. The prefactor A_0 is linear to Oh. The power index n is linear to Oh in the range of $0.5 < Oh < 0.66$ and remains a constant when Oh increases toward 1.0.

In an additional 11 cases which vary the fluid density, fluid viscosity, and surface tension, resulted in three Oh numbers, $Oh = 0.509, 0.654$, and 0.800. The power-law temporal scaling of unequal size microbubble coalescence for each Oh number was captured from the numerical simulation. All three Oh cases are in agreement with the predictions from the formulation, Equation 4.3, demonstrating the reliability of this newly discovered general power-law temporal scaling. This scaling was obtained when the gas phase was fixed. Based on recent studies [54, 71, 153], the droplet coalescence is sensitive to the outer fluid (heavy fluid) but insensitive to the inner fluid (light fluid). We expect this conclusion applies to the current work. That is to say, the results of this work obtained from a fixed gas (air) are applicable for different gases.

5. COALESCENCE-INDUCED MICROBUBBLE DETACHMENT IN MICROFUIDICS

5.1 Introduction

Bubble detachment in the microchannel is a common phenomenon during the bubble oscillation stage when the bubble initially attaches on the solid surface. It can be observed in many industrial and medical processes, such as electrochemical reaction in a microchannel [25,154,155], thermal management of semiconductor [156], self-cleaning for membrane biofouling [157, 158] and microbial colonization of dental surface [159], to name a few. In general, external energy input and internal motion are two major mechanisms to drive the bubble detachment from a surface. External energy through heat transfer [160, 161], acoustic effects [162], and light irradiation [163] causes the growing of microbubbles and further detaching from the surface. The research focuses on energy-driven bubble detachment have been on the detachment criteria [164] and the optimization to balance between detachment and unclogging in microchannels [156, 165]. Bubble detachment caused by internal motion, e.g., microbubble coalescence [166], is more fundamental and significant to understand the underlying physics of bubble dynamics for the design and fabrication of microfluidics with various applications. In spite of a few attempts made on revealing the effects of surface conditions such as superhydrophobic, smooth surface [167, 168], superhydrophobic, rough surface [169], Leidenfrost surface [170], and initial conditions and radius inequality [171] on the coalescence-induced detachment of droplets, the detachment dynamics due to microbubble coalescence has been rarely addressed.

The experiment was carried out inside a polymer microfluidic gas generation device to study one of the phenomena in the post-coalescence of bubble coalescence. This device is fabricated by aligning and sequentially stacking/thermopress bonding multiple layers of patterned polystyrene (PS) film [172]. Figure 5.1(a) schematizes the cross-section view of

the device. Hydrogen peroxide (H_2O_2) enters at the inlet and performs a catalytic decomposition producing water (H_2O) and oxygen (O_2) on the layer of Pt catalyst. The oxygen bubbles travel from left to right driven by imbalanced capillary force due to unequal channel heights and then trapped at the gas vent through a membrane. Right before the gas vent, the inner walls of the micro-channel change from hydrophilic to hydrophobic surfaces. Whereas liquid, driven by the moving bubbles, leaves at the outlet. High-speed X-ray imaging was conducted at the 32-ID-B beamline of the Advanced Photon Source (APS) to visualize the bubble transport in the reaction channel, see a snapshot in Figure 5.1(b). The detail description of the design, fabrication, imaging acquisition of the experiment is referred to as published papers [172, 173].

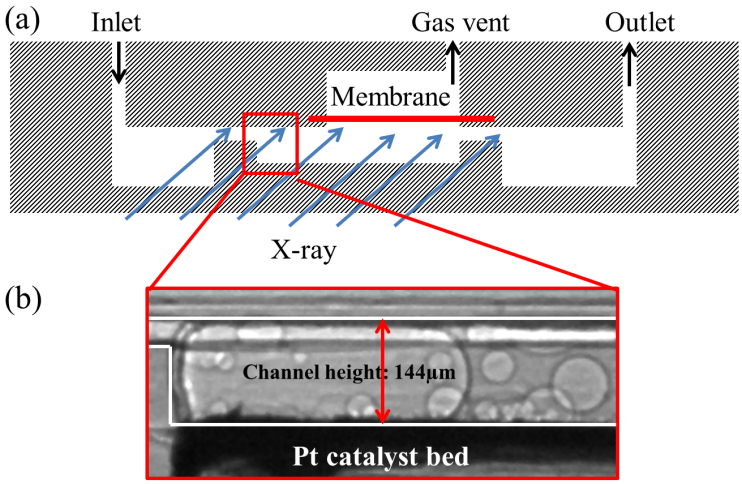

Figure 5.1: (a) Schematic of the cross-section view of the fabricated polymer microfluidic gas generation and (b) high-speed X-ray images of the device

5.2 Computational set-up

We looked into eight videos of bubble transport recorded from the experiment and identified six cases, in each of which unequal bubble coalescence is observed. The same initial set-up is required to recover the experimental bubble coalescence process by simulation. We use ImageJ (National Institutes of Health) to measure the radii, r_F and r_M and

center locations, O_F and O_M of the two initial parent bubbles after cropping the computational domain as small as possible. The process is indicated in Figure.5.2. Meanwhile, the parameters for the initial set-ups are shown in Table 5.1.

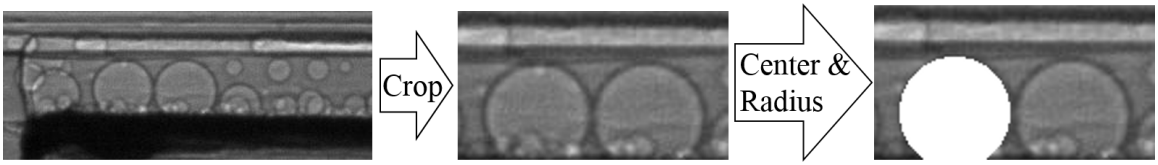

Figure 5.2: The brief image process to get the centers and radii of two parent microbubbles

$Case\#$	$r_F(\mu m)$	γ	O_F $(\mu m, \mu m)$	O_M $(\mu m, \mu m)$
1	19	1.27	(69, 15)	(33, 13)
2	24	1.41	(80, 18)	(37, 15)
3	39	1.34	(59, 35)	(127, 21)
4	43	1.72	(71, 37)	(137, 21)
5	55	1.06	(186, 39)	(78, 44)
6	62	1.82	(88, 50)	(185, 26)

Table 5.1: Parameters of the initial set-ups in the experimental cases

As schematized in Figure.5.3, two parent oxygen bubbles (gray color) with the size inequality ($\gamma = r_F/r_M$) in the hydrogen peroxide solution merge into one single child bubble with minimal area surface (red color). The center and radius of the single child bubble are O_e and R_e respectively. The size inequality is the radius ratio of large (father) r_F vs. small (mother) r_M bubbles. The density and viscosity of oxygen and 30% hydrogen peroxide are $\rho_{O_2} = 1.3kg/m^3$, $\rho_{H_2O_2} = 1060kg/m^3$, $\mu_{O_2} = 1.92 \times 10^{-5}kg/(m \cdot s)$, $\mu_{H_2O_2} = 1.06 \times 10^{-3}kg/(m \cdot s)$ respectively. The numerical study is conducted in height $H = 144$ (μm) cuboid domain with periodic boundary in x and z directions. The length

of the channel is L, which determined by the size of microbubbles varies from $100\mu m$ to $264\mu m$. And the width of the channel W (in the z-direction) is the same as the length. For all cases, the equilibrium contact angle is set as $36°$.

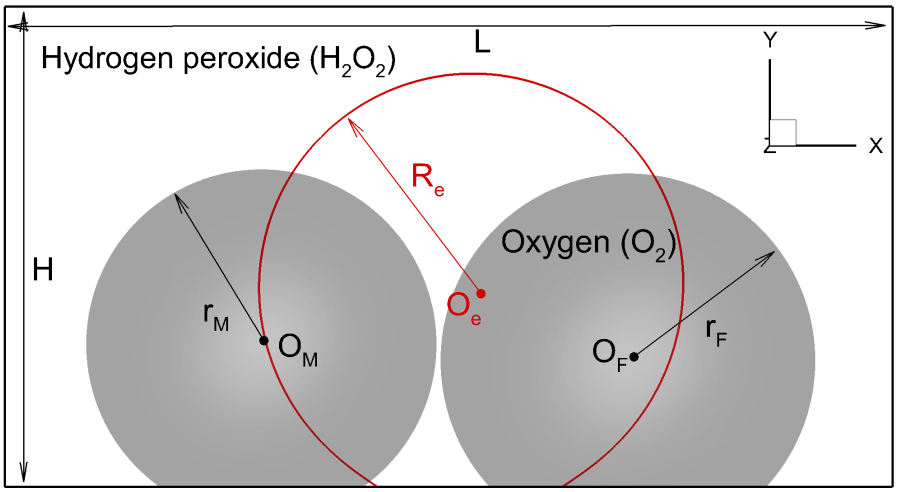

Figure 5.3: Schematics of two oxygen bubbles coalescence in the hydrogen peroxide solution from initial state (gray) to steady state (red)

5.3 Convergence check & Validation

The contact angle is simulated to find the appropriate spatial resolution for the numerical analysis. We set an half-sphere bubble (i.e., $\alpha^{initial} = 90°$) with $R = 60\mu m$ initially sit on a solid surface, and the targeted contact angle of the solid surface is $60°$. As Figure 5.4 shows, the initial bubble (gray color) with half sphere becomes the equilibrium state. In the equilibrium state, the slice (black line) in the middle of x-direction is chosen to do the validation and the liquid-vapor interface, which is represented by a contour level of $C = 0.5$. The simulated contact angle α^{eq} can be calculated by Eq.5.1 through the measurement of the height of liquid-vapor interface a and a base diameter of a bubble b on a solid surface at equilibrium state.

$$\alpha^{eq} = 2arctan(\frac{b}{2a}). \tag{5.1}$$

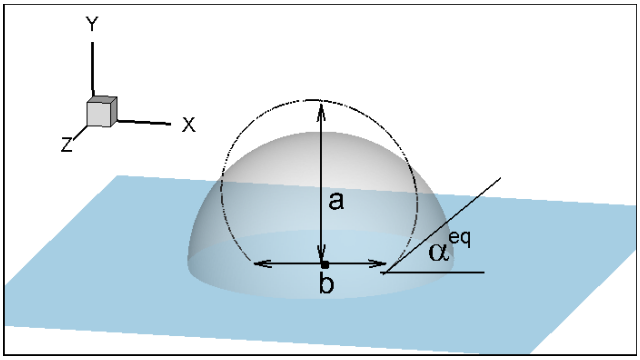

Figure 5.4: Schematics of the half sphere bubble initially sitting on the wetting surface

Convergence check and validation are done through the spatial resolution varies from $44 \times 24 \times 44$ to $264 \times 144 \times 264$ with six different levels which listed in Table 5.2. The fourth and fifth columns of this table show the relative difference between simulated and targeted contact angle and spatial convergence, respectively. Take computational cost and accuracy into consideration, and we select the spatial resolution of $220 \times 120 \times 220$ to conduct the parametric study unless otherwise indicated.

Resolution	Simulated contact angle	Targeted contact angle	Relative difference(%)	Convergence (%)
$44 \times 24 \times 44$	53.00	60	11.67	
$88 \times 48 \times 88$	56.88		5.20	6.82
$132 \times 72 \times 132$	58.10		3.17	2.10
$176 \times 96 \times 176$	59.22		1.30	1.89
$220 \times 120 \times 220$	59.58		0.70	0.60
$264 \times 144 \times 264$	59.84		0.27	0.43

Table 5.2: Convergence check and validation when targeted contact angle is $60°$.

To validate this numerical method suitable for a wide range of contact angles is very important as well. Here the initial area of the bubble is kept constant that half sphere with $60\mu m$ radius on a solid wetting surface as Figure 5.4 shows. A slice in the center of the

x-direction is selected to show the shape of the circular arc and calculated the simulated contact angle in an equilibrium state with the different wetting surface, i.e., different targeted contact angle. Figure 5.5(a) presents the relationship between the equilibrium contact angle and dimensionless wetting potential Ω_c when the equilibrium contact angle varies from $40°$ and $150°$. The numerical result is well consistent with the analytical result. Two cases selected from all the test cases to show the equilibrium profiles of a bubble sitting on a solid surface with equilibrium contact angles of $150°$ and $45°$ are indicated in the Figure 5.5(b) and Figure 5.5(c) respectively. The red point is the analytical circular arc, and the black lines are the contour level of $C = 0.2, 0.5, 0.8$, respectively. Compare the shape between the analytical circular arc and the numerical equilibrium profile of the bubble, and the test cases confirm that free-energy based LBM with cubic boundary condition is reliable.

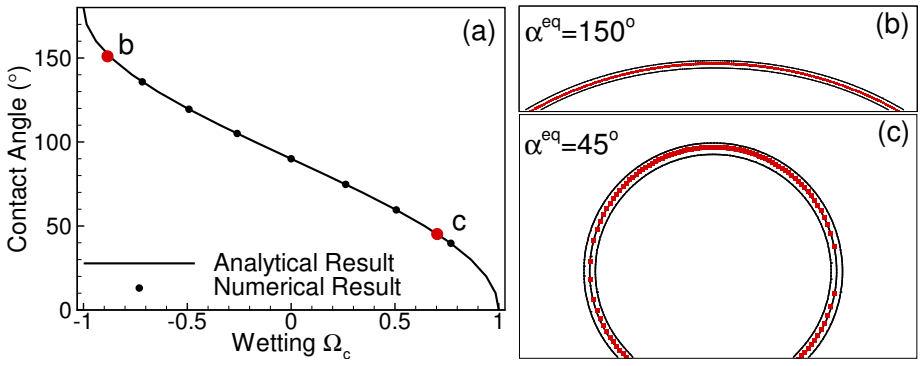

Figure 5.5: (a) The comparison of the relationship between equilibrium contact angle and dimensionless wetting potential with analytical and numerical results; Equilibrium profiles of the bubble on the solid surface of (b) $\alpha_{eq} = 150°$ and (c) $\alpha_{eq} = 45°$

5.4 Numerical and experimental study of coalescence-induced microbubble detachment

Experimental cases are recorded by the high-speed camera with $90kHz$ or $100kHz$, which applied to investigate the bubble coalescence. From the six experimental cases showing in Table 5.1, we find there are two distinct phenomena as Table 5.3 presents. Hence, we have a hypothesis that the coalescence-induced microbubble detachment phenomenon

(CIMD) occurs when the bubble radius ratio close to 1. Due to the fast speed of microbubble coalescence and the uncontrollable bubble size in the experiment, the dynamic of the coalescence and the conditions for CIMD can't afford to be studied only from the experimental cases. The parametric study of simulation is applied to confirm this hypothesis.

$Case\#$	$r_F(\mu m)$	γ	Detachment or not
1	19	1.27	No
2	24	1.41	No
3	39	1.34	No
4	43	1.72	No
5	55	1.06	Yes
6	62	1.82	No

Table 5.3: The coalescence-induced detachment phenomena can be observed or not in the experimental cases.

Before confirming the hypothesis, the suitable of the methodology should be validated. From the process of bubble coalescence in experimental cases, there is a big difference between case 5 and others. In case 5, CIMD can be observed in the animation of the experimental results, but from the static image, there are lots of small bubble at bottom affects the visual view. In other cases, the microbubble always attaches in the solid surface during the global process of bubble coalescence. Hence, No. 5, and 6 cases are selected as two representative cases to do the comparison between the experiment and simulation, which is shown in Figure 5.6. For each case, there are two rows. The top row is the result of the simulation at six instantaneous times, and the bottom row is the result of experiments with the same time. We find the process of shape evolution between simulation and experiment are quite similar in both cases. They start from the two parent microbubbles touched, generation and growth of neck bridge; then bubble oscillates with a small amplitude; eventually

becomes a single child bubble. Meanwhile, the case for CIMD occurring is consistency with experimental cases.

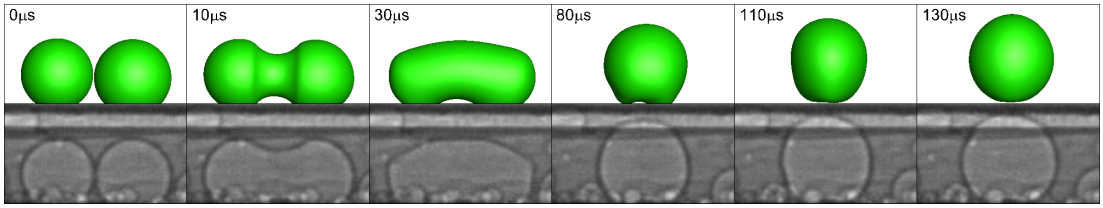

(a) Case 5

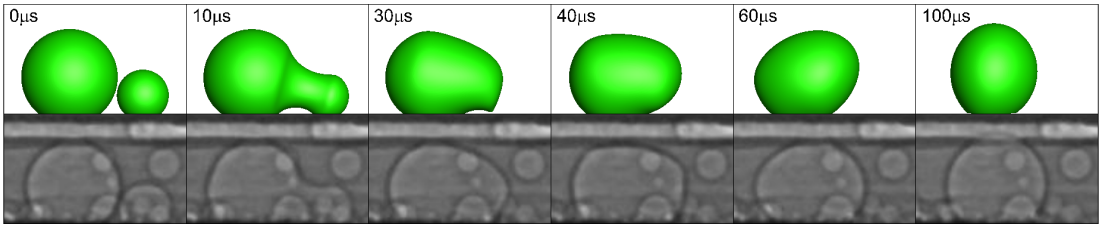

(b) Case 6

Figure 5.6: Time evolution of bubble coalescence: (a) case 5 and (b) case 6 are both presented the phenomenon from the simulation (top row) and experiment (bottom row) with six specific times.

The process of CIMD is focused on the bubble radius ratio and bubble size. Therefore, the bubble radius ratio varies as 1, 2, 3 and the radius of the father bubble $r_F = 30$, 36, 42, 48 μm are selected as study cases showing in the Table 5.4.

From the investigation of the experimental and numerical cases, we generated a phase diagram showing as Figure 5.7 to investigate when the CIMD occurs. The black circle symbols indicate the results are from the simulation, and the red rectangular symbols are from experimental cases. The CIMD can be observed in the case marked with the solid symbol. From the phase diagram, we find when the radius ratio is close to 1, and the radius of the father bubble is larger than $40\mu m$, the phenomena will occur. That means the CIMD does not only depends on the bubble radius ratio but also relates the size of the microbubbles.

Why do these two conditions affect the occurring of CIMD? Here we discuss in two parts.

$Case\#$	$r_F(\mu m)$	γ	O_F $(\mu m, \mu m)$	O_M $(\mu m, \mu m)$
*1	19	1.27	(69, 15)	(33, 13)
*2	24	1.41	(80, 18)	(37, 15)
3	30	1	(101,29)	(161, 29)
4		1.93		(145, 15)
5		3.13		(137, 11)
6	36	1	(95,33)	(167,33)
7		2		(146, 18)
8		3		(138, 13)
*9	39	1.34	(59, 35)	(127, 21)
10	42	1	(89,38)	(173, 38)
11		1.95		(150, 20)
12		2.92		(139, 14)
*13	43	1.72	(71, 37)	(137, 21)
14	48	1	(83,44)	(179,44)
15		2		(152, 23)
16		3.07		(143, 17)
*17	55	1.06	(186, 39)	(78, 44)
*18	62	1.82	(88, 50)	(185, 26)

Table 5.4: Parameters of the initial set-ups in the experimental(mark with *) cases and numerical cases of the parametric study

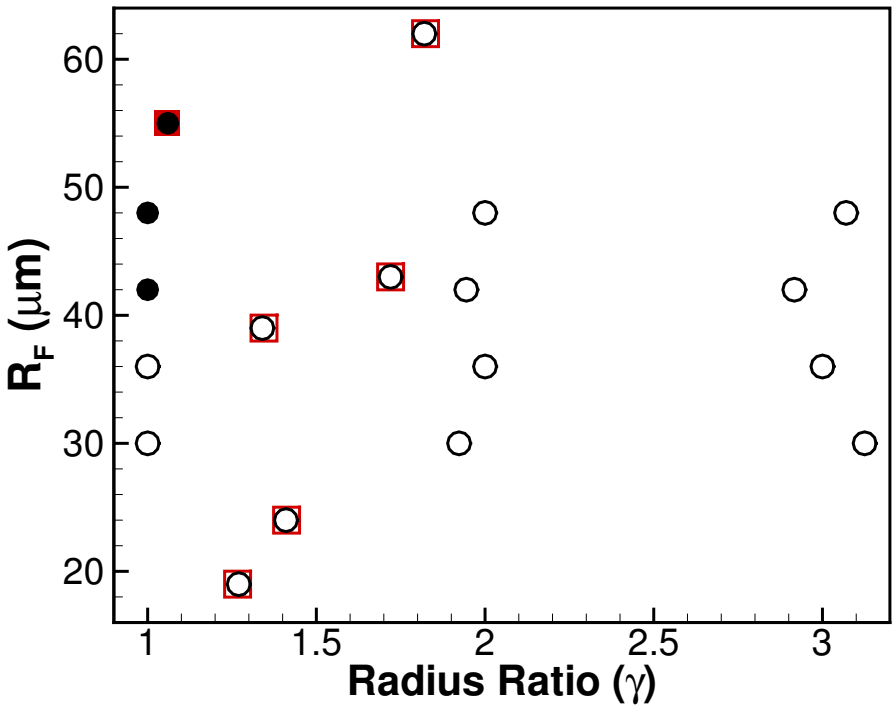

Figure 5.7: The bubble radius ratio and radius of farther bubble effect on CIMD. The circle symbols(black): numerical cases, the rectangular symbols(red): experimental cases. The solid symbols: CIMD can be observed, empty symbols: no detachment phenomena.

Same father bubble size with different size ratio

Two representative cases with same father bubble radius $r_F = 42\mu m$ and different size ratio: (a) $\gamma = 1.94$ and (b) $\gamma = 1.0$ as Figure 5.8 represents to study the mechanism. In each case, the velocity distribution of bubble coalescence is illustrated as three different stages: (1) early stage (i.e., generation and growth of neck bridge), (2) intermediate stage(i.e., the neck bridge continuous growth until two bubbles merge into one), (3) late stage (i.e., bubble oscillation after two parent bubble merged into one). In stage 1 ($T = 4\mu s$), the bubble with a smaller radius has the larger surface tension force in the perpendicular direction of the centerline to drive the bubbles coalescing. The time evolution in case (a) is faster than the

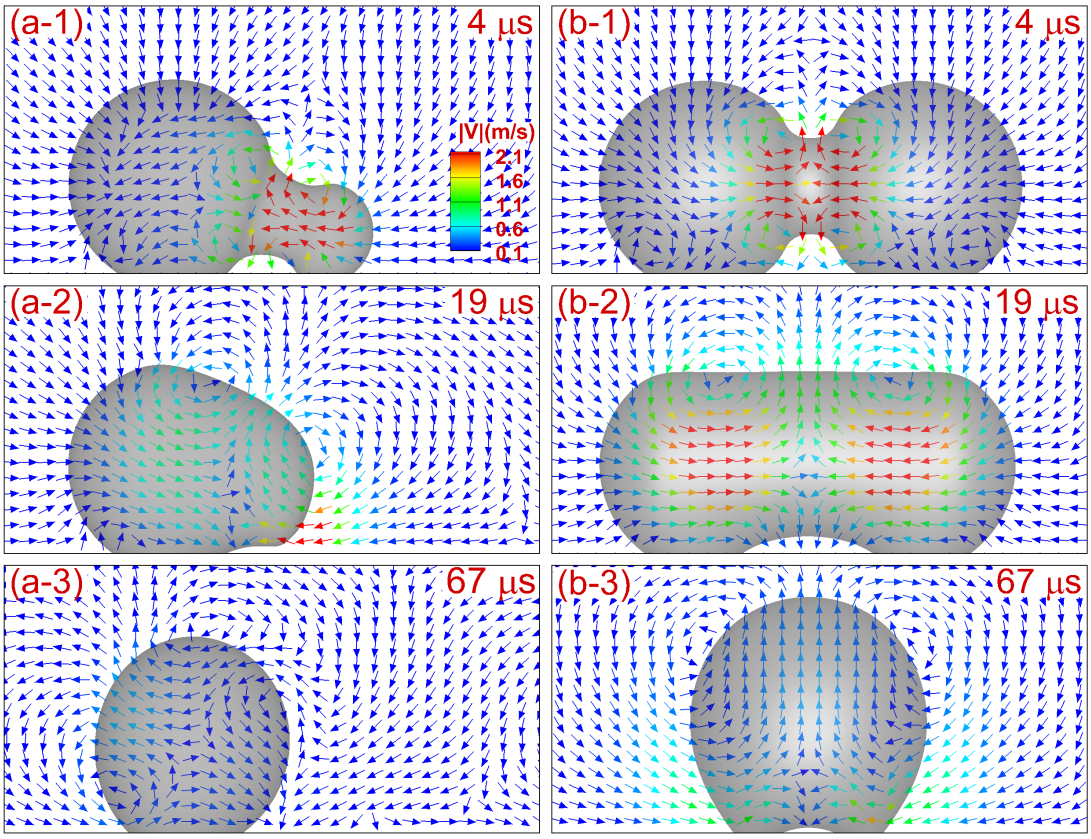

Figure 5.8: Instantaneous velocity fields with the velocity magnitude $|V| = \sqrt{v_x^2 + v_y^2 + v_z^2}$ color map in three different stages: (1) early stage; (2) intermediate stage; (3) late stage with two different cases (a) $\gamma = 1.94$, (b) $\gamma = 1.0$ with $r_F = 42\mu m$

case (b). And the kinetic energy distribution of gas is different between these two cases. In case (a), the larger kinetic energy in the side of the mother bubble, whereas, it is in the neck bridge region of case (b). Hence, at $T = 19\mu s$ of stage 2, the mother bubble detaches from the solid surface with larger kinetic energy. The father bubble almost keeps the same as it is in the case (a). However, the process of bubble coalescence is symmetrical, and two parent bubbles move on the solid surface for a similar bubble size in the case (b). From stage 2 to 3, the vortexes develop in the direction along the surface of the sphere for case (a), so that there is no extra force make the bubble detached from the solid surface. Whereas, symmetrical development make the detachment easier in case (b).

Same size ratio with different father bubble size In order to investigate the condition caused by the different father bubble radii, the cases are selected with same size ratio $\gamma = 1.0$, and two representative sizes of father bubble (b)$r_F = 42\mu m$ and (c)$r_F = 30\mu m$. The

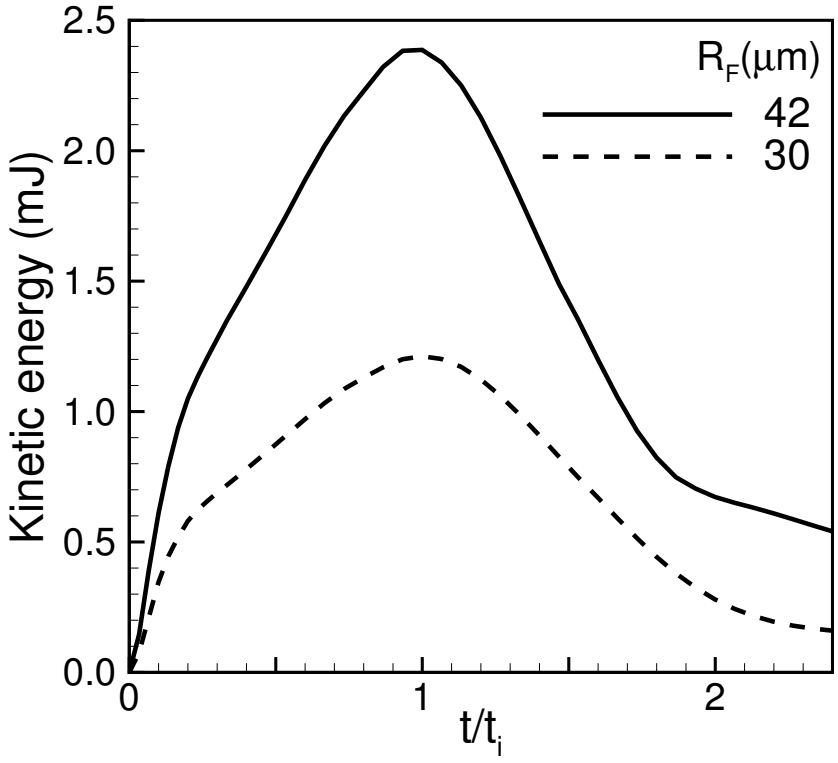

Figure 5.9: Kinematic energy distribution with normalized time (t/t_i) for two different cases (b) $r_F = 42\mu m$, (c) $r_F = 30\mu m$, with $\gamma = 1.0$

kinetic energy distribution is indicated in Figure 5.9. Comparing these two cases, the driving force of case (c) is larger than the case (b) due to the small radius bubble have large capillary force. However, the energy dissipation is larger in case (c) as Figure 5.9 presenting. In other words, the resistant force is much larger in the case (c) which is consistent with a smaller radius lead to the larger resistant force.

Size ratio close to 1 and the larger father bubble size are the two conditions for observing the CIMD easily. These two conditions are consistent with the tendency in the Ref. [174] which describe the criteria of the diameter of heated bubble detachment from the solid surface, but the driving mechanism is different.

5.5 Conclusion

We have systematically studied CIMD in the process of microbubble coalescence by six experimental cases recorded by the high-speed camera and eighteen numerical cases including six cases with the same initial set-ups of the experiments and twelve cases with different combinations of radius ratio and father bubble size. In this work, we imposed a gas-liquid-solid interface in the code and did the validations through a half sphere bubble sitting on the different wetting surfaces with targeted contact angles from $36°$ to $150°$. The focus is on conditions to observe CIMD by the experimental and numerical investigation when two-parent oxygen bubbles attached on the Pt surface with $36°$ contact angle in the hydrogen peroxide solution. The results are summarized as follows.

- The phenomenon of microbubbles coalescence on the solid surface is consistent with experimental capture.
- Both the size inequality and bubble size have effects on the CIMD. When the bubble size ratio is close to 1, and father bubble size is larger, the CIMD is observed easily.

Additionally, the velocity distribution during bubble coalescence process, including early stage, intermediate stage, and late stage is applied to study the reasons for occurring of CIMD. For the same father bubble radius and different size ratio, the mother bubble dominate the effects of mechanism. The smaller mother bubble has a large capillary force for

driving that leads the mother bubble to detach from the solid surface. After the mother bubble detaches from the solid surface, the energy dissipated and father bubble doesn't have enough energy to detach. Similar size bubble coalescence, the process is symmetrical, detach from the solid surface is easier. While, the smaller bubble size with same size radius ratio, the resistant force caused by the viscous force is larger. It results in small radius bubble have not enough energy detach from solid surface corresponding with larger radius bubble.

6. EFFECTS OF INITIAL CONDITIONS ON THE MICROBUBBLES COALESCENCE

6.1 Introduction

Coalescence is a common process in gas-liquid systems. When two bubbles/droplets are close, a microscopic connecting neck bridge will form and rapidly grow tending to merge and minimize the surface area. Studying the neck bridge (contact area) growth at the early stage of coalescence is essential in understanding the dynamics of bubble/droplet co-

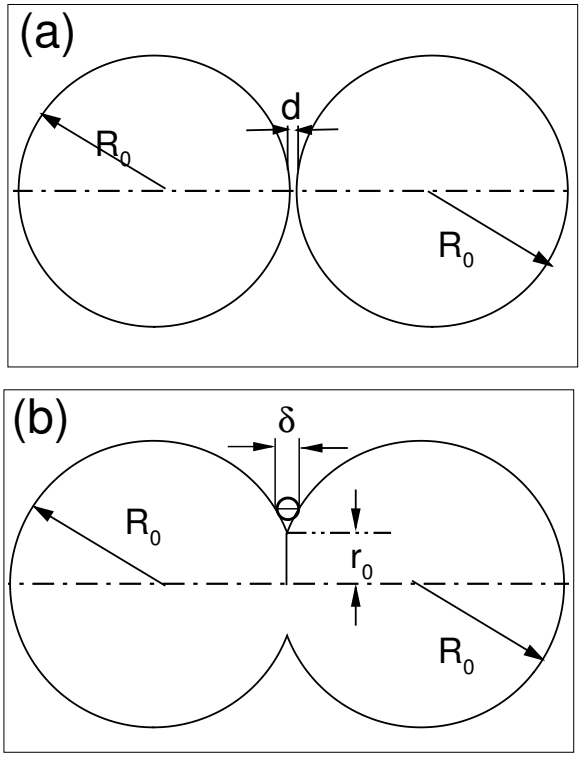

Figure 6.1: Schematics of two initial scenarios for two equal bubbles with radius R_0: (a) separated bubbles with distance d and (b) connected bubbles with neck bridge radius r_0 and meniscus diameter δ. The meniscus curvature is $K_\delta = 2/\delta$.

alescence [52,153,175–177]. Many efforts have been focused on the neck bridge evolution of droplet coalescence through numerical [51, 53, 72], experimental [46, 50] and theoretical [47] studies. There are two common initial set-ups from simulations and experiments. Separated with small distance d or connected with a small neck bridge radius r_0, schematized in Figure 6.1 (a) and (b) respectively, are two typical initial set-ups in the research of bubble/droplet coalescence. In scenario (a), when the distance d is small enough, two bubbles/droplets are attracted through Van de Waals attraction force till bubbles/droplets touch when the coalescence starts [40, 67]. Whereas in scenario (b), the initial radius r_0, corresponding to a meniscus diameter δ thus meniscus curvature $K_\delta = 2/\delta$, is usually due to small perturbation because the static touch of two bubbles/droplets are not stable and the coalescence starts immediately. The effects of these two scenarios on droplet coalescence have been studied numerically [177]. It has been observed that for scenario (a), the bridge evolution is sensitive to the distance of the initial separation and for scenario (b), a slower initial growth corresponds a larger initial neck bridge radius. The dynamics of microbubble coalescence under various influences are needed to be systematically investigated.

6.2 Computational set-up

The early-stage coalescence ($t < 5\mu s$) of two identical air micro-bubbles are studied, R_0(=20μm) sitting at the center of a square domain filled with water. The side length of the domain is 100(μm). For the purpose of exploring the effects of initial conditions of the bubbles on the bubble coalescence, two conditions are considered, as schematized in Figure 6.1. In case (a), the bubbles are separated by a distance d, as used in the experimental set-up [40]. It is known [42, 67, 178] that when the separation of two bubbles is within the effective range of intermolecular attraction force, the attraction force will drive the bubbles moving inward. When the bubbles are touched, a bridge is formed, and then the bubble coalescence starts. Figure 6.2 shows the instantaneous velocity vector fields right before and right after the neck bridge forms. The small separation distance is selected to ensure the occurrence of coalescence. The ratio of separation distance and bubble radius, $\gamma_d(\equiv d/R_0)$,

varies from 0.008 to 0.042. In case (b), the bubbles are connected with an initial neck bridge radius r_0. The ratio of initial bridge neck radius and bubble radius, $\gamma_r(\equiv r_0/R_0)$ changes from 0.16 to 0.38. The domain boundaries in vertical and horizontal directions are periodic. The density and viscosity of the water and air are $\rho_h = 10^3(kg/m^3)$, $\rho_l = 1.2(kg/m^3)$ and $\mu_h = 10^{-3}kg/(ms)$, $\mu_l = 1.98 \times 10^{-5}kg/(ms)$ respectively, resulting in the density ratio 833 and viscosity ratio 50.5 of water vs. air. The surface tension between water and air is assumed $\sigma = 7.2 \times 10^{-2}N/m$. Such a physical set-up was used in this section unless otherwise indicated.

6.3 Convergence Check & Verification

To investigate the effects of the initial conditions on the microbubbles coalescence, we take power-law scaling between neck bridge evolution and normalized time as a validation test to find out an appropriate resolution firstly. Selecting $Oh = \mu_h/\sqrt{\rho_h R_0 \sigma} = 2.6 \times 10^{-2}$ (inertial regime) and varying five spatial resolutions of 200^2, 400^2, 600^2, 800^2, 1000^2 for the flow domain. It is found that in all the five cases, the time evolution of neck bridge radius r follows power-law $r/R_0 = A_0(t/t_s)^{1/2}$. There are two kinds of timescale for normalizing the time of this process [46], $t_i = \sqrt{\rho_h R_0^3/\sigma}$ when the coalescence process dominated by the competition with capillary force and inertial force. When the effect of viscous forces on resisting the process becomes important, the system follows another timescale, $t_v = \mu_h r_F/\sigma$. $0.2 < Oh < 1$, both t_i and t_v have approximately the same values, which means that both the inertial and viscous forces contribute to the resisting force in the coalescence process. In this case, $Oh = 2.6 \times 10^{-2} < 0.2$, so that $t_s = t_i = \sqrt{\rho_h R_0^3/\sigma} = 10.5\mu s$, and t is measured from the instant of bubble coalescence, with varying A_0, as shown in Table 6.1. The neck bridge radius r is determined through contour line of $C = 0.4$. As the resolution increases, A_0 converges to 1.06 with reducing relative errors. To avoid high computation cost, 600^2 is selected as the typical resolution to produce the results for the present study. The half power-law scaling, $r/R_0 \propto (t/t_i)^{1/2}$, meets the analytical prediction [54]. The

prefactor $A_0 = 1.05$ for this resolution is within the range of experimental measurements [175, 179], 1.09 ± 0.08 for air bubbles coalescence in water.

The relationship between normalized neck bridge r/R_0 and normalized time. It is seen in Figure 6.3 that the simulation results (symbols) agree well with the analytic bridge

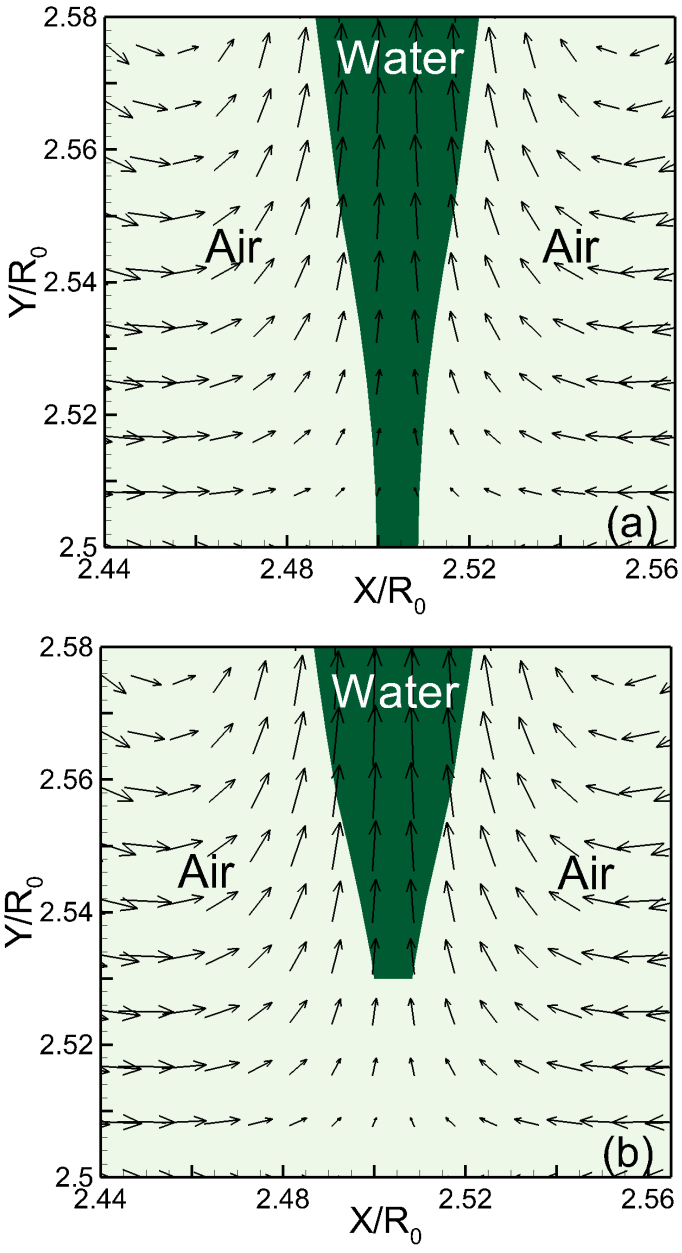

Figure 6.2: Instantaneous velocity fields right before (a) and right after (b) two bubbles are connected forming a neck bridge.

Resolution	200^2	400^2	600^2	800^2	1000^2
A_0	0.9181	1.1017	1.050	1.056	1.060
Relative error	13.39%	4.06%	0.94%	0.37%	$\times$

Table 6.1: Resolution convergence check and the relative error is to the finest resolution.

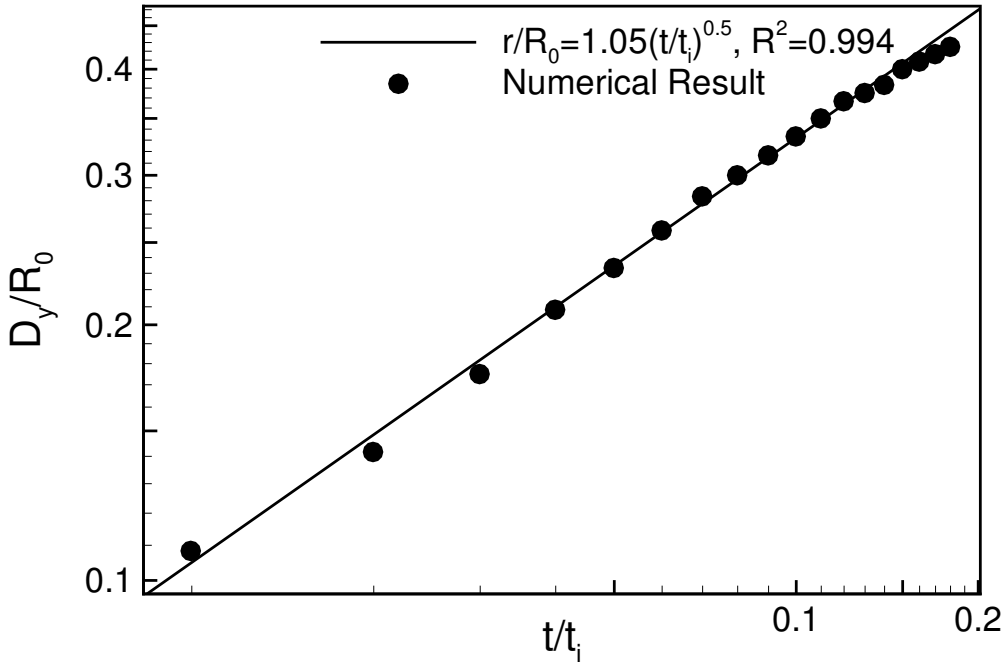

Figure 6.3: The simulation results (symbols) agree well with the power-law (line), it is demonstrating the validity of the modeling.

evolution in early time [47] (line) i.e. $r/R_0 \propto (t/t_i)^{0.5}$ with prefactor 1.05 and $R^2 = 0.994$, demonstrating the validity of the modeling.

6.4 Effects of initial neck bridge radius r_0 on neck bridge evolution

In this part, five cases with the relative radii of the initial neck bridge, $\gamma_r (= r_0/R) = 0.16, 0.20, 0.28, 0.33,$ and 0.38, are investigated. Figure 6.4 shows the neck bridge evolution of a representative case ($\gamma_r = 0.28$). It can be seen in Figure 6.4(a) that after a development

time, the relative growth of neck bridge, $(r - r_0)/R_0$, becomes linear to $(t/t_i)^{1/2}$, which is equivalent to the half power-law of $(r-r_0)/R_0 = 0.81(t/t_i)^{1/2}$. The half power-law scaling has been predicted analytically [47], which has been confirmed in recent experiments [54]. The result is a numerical confirmation of the half power-law scaling. In order to understand the underlying physics of the early neck growth, we should closely look into the driving mechanism to the coalescence in this early stage. Figure 6.4(b) shows the neck bridge development in the development time from a to d and half power-law scaling regime from d to f indicated in Figure 6.4(a). As the neck bridge radius r increases gradually, pushing the bottom of the neck up, the meniscus gradually rounds up with an increased diameter of δ. Table 6.2 lists the curvature of meniscus ($K_\delta = 2/\delta$) vs. curvature of neck bridge ($K_r = 1/r$) at the corresponding time sequence. At the initial time (point a), the neck bridge radius is set to be small and corresponds a steep meniscus, resulting in the curvature of the meniscus 5600 times larger than the curvature of the neck bridge. It implies that the initial growth of the neck bridge is driven by the curvature of the meniscus. Within a very short time period ($0.01t_i$) from point a to d, the meniscus curvature K_δ rapidly reduces 29311% from 1000.0 to 3.4 μm^{-1} while the neck curvature K_r only reduces around 21% from 0.179 to 0.147μm^{-1}. In other words, toward a more balanced driving mechanism contributed by both meniscus curvature and neck bridge curvature. In the period of half power-law scaling from time point d to f, it is seen that the ratio of the two curvature is around 15. Thus, the time development before the half-power law scaling is due to the significantly unbalanced capillary force of the meniscus curvature and the neck curvature.

The time evolution of the neck bridge with different initial neck bridge radius, is plotted in Figure 6.5, distinguished by the dimensionless parameter $\gamma_r (= r_0/R_0)$. The solid line corresponds to the representative case discussed above. While each initial radius case has a similar tendency of the neck growth to the representative case, it is seen that smaller γ_r (from bottom up) results in faster growth of the neck bridge, meaning that smaller initial neck bridge leads faster coalescence at the early stage. It is noticed that the plotted power-law scaling as $(r - r_0)/R_0 = A_0(t/t_i)^{1/2}$ for the purpose to compare different initial neck bridge radius r_0. Meanwhile, smaller γ_r exhibits faster neck bridge evolution. Smaller γ_r

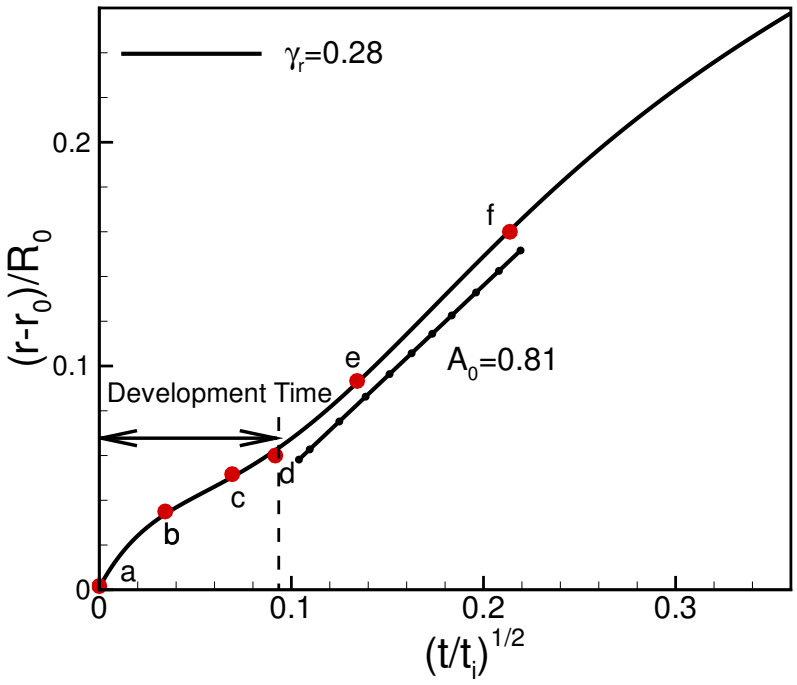

(a)

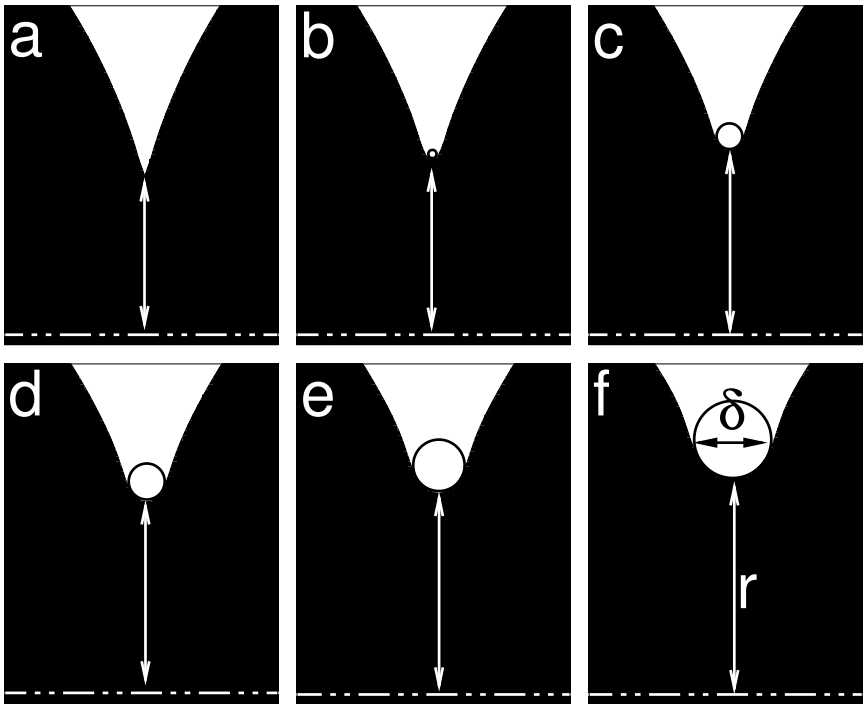

(b)

Figure 6.4: (a) A representative neck bridge evolution for the case of $\gamma_r = 0.28$. (b) Sequence of meniscus development and neck growth across development time (from a to d) and half power-law scaling time (from d to f).

Time Point	δ	r	$K_\delta(=2/\delta)$	$K_r=(1/r)$	K_δ/K_r
a	0.002	5.6	1000.0	0.179	5600
b	0.067	6.3	29.9	0.159	188
c	0.417	6.6	4.8	0.152	32
d	0.583	6.8	3.4	0.147	23
e	0.833	7.1	2.4	0.141	17
f	1.250	7.6	1.6	0.132	12

Table 6.2: Curvature of meniscus (K_δ) vs. curvature of neck bridge (K_r) at representative time points indicated in Figure 6.4(a). Units: δ and r – μm. K_δ and K_r – μm^{-1}

γ_d	0.008	0.017	0.025	0.033	0.042
Development Time (t/t_i)	0	0.0076	0.0196	0.0256	0.289
A_0	1.05	1.08	1.12	1.12	1.13

Table 6.3: Effect of γ_d on the development time.

corresponds to larger initial curvature of the meniscus, resulting in large capillary force to drive the neck growth, leading faster coalescence. Corresponding to the smallest $\gamma_r = 0.16$ (long-dash line), the initial curvature of meniscus a neck bridge is as high as 2985 as opposed to 1000 of the representative case (solid line). These effects of initial neck bridge radius on micro-bubble coalescence are similar to those on droplet coalescence [177].

6.5 Effects of initial separation distance (d) on neck bridge evolution

In this part, five cases with different initial separation distance d, distinguished by $\gamma_d(=d/R_0) = 0.008, 0.017, 0.025, 0.033, 0.042$, are investigated. Once again, the half power-law scaling after development time is seen in each separation case, which is a numerical confirmation for the analytical prediction [47]. The development time is defined in Figure 6.6. The time evolution of the neck bridge is plotted in Figure 6.7. It is seen

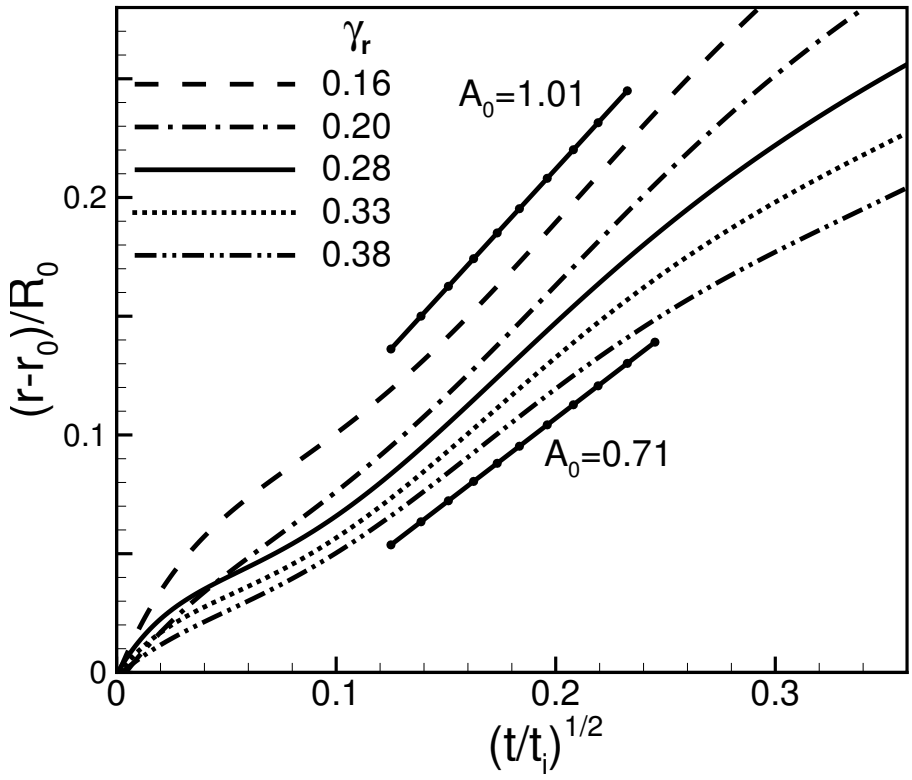

Figure 6.5: Effects of initial neck bridge radius ($\gamma_r = r_0/R_0$) on the growth of the neck bridge radius (r/R_0). The solid line corresponds to the representative case in Figure 6.4.

that smaller separation distance (bottom-up) leads faster neck growth, thus faster coalescence, and shorter development time. Table 6.3 lists the development time for each case. The smallest γ_d case starts the half power-law almost immediately when two bubbles attach whereas the largest γ_d case takes $0.289t_i$ before starting the half power-law. The development time for this initial scene is the result of elongated neck formation, as explored in a study of the effects of initial separation distance to the neck growth in droplet coalescence [177]. As the initial separation d is small enough, within the effective range of the intermolecular attraction force, the attraction force between the two approaching surfaces initiates the thinning and rupture of the liquid film between two bubbles and forms a gas bridge. The film is thinning leads to an elongated neck bridge in the horizontal direction.

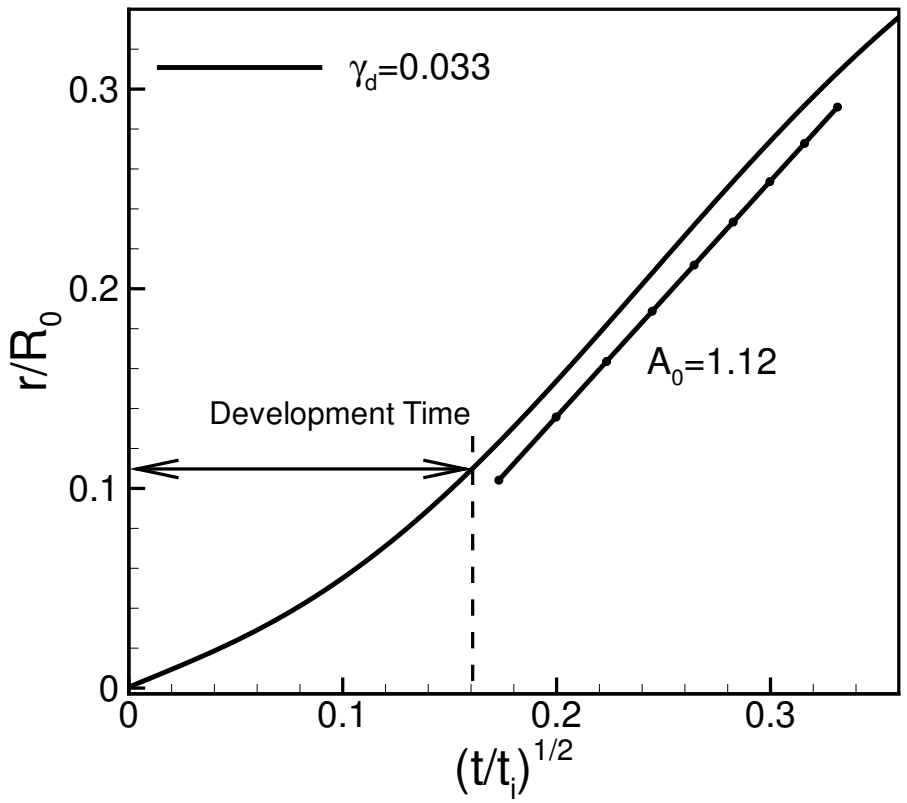

Figure 6.6: A representative neck bridge evolution for the case of $\gamma_d = 0.033$.

As seen in Figure 6.8 for two initial separation distance cases with $\gamma = 0.008$ (a) and 0.042(b) respectively, smaller separation distance forms shorter neck bridge with larger curvature of meniscus. The larger meniscus curvature leads to faster neck growth, thus faster coalescence, as have been discussed above.

The prefactor A_0 represents the relative neck bridge radius r/R_0 at $t = t_i$. Table 6.3 shows that for the varying initial separation distance cases, A_0 varies marginally from 1.05 to 1.13. It is in good agreement with experimental results. Table 6.4 shows A_0 values of different liquids. The experimental cases are all in the inertial regime, the same as the present study. It seems that A_0 is closely related to the density of the liquid. Larger liquid density leads to a smaller A_0. The current work studies air bubble coalescence in water with the liquid density of $\rho_h = 1000kg/m^3$. The range of A_0 in the present work agrees well with the experimental results.

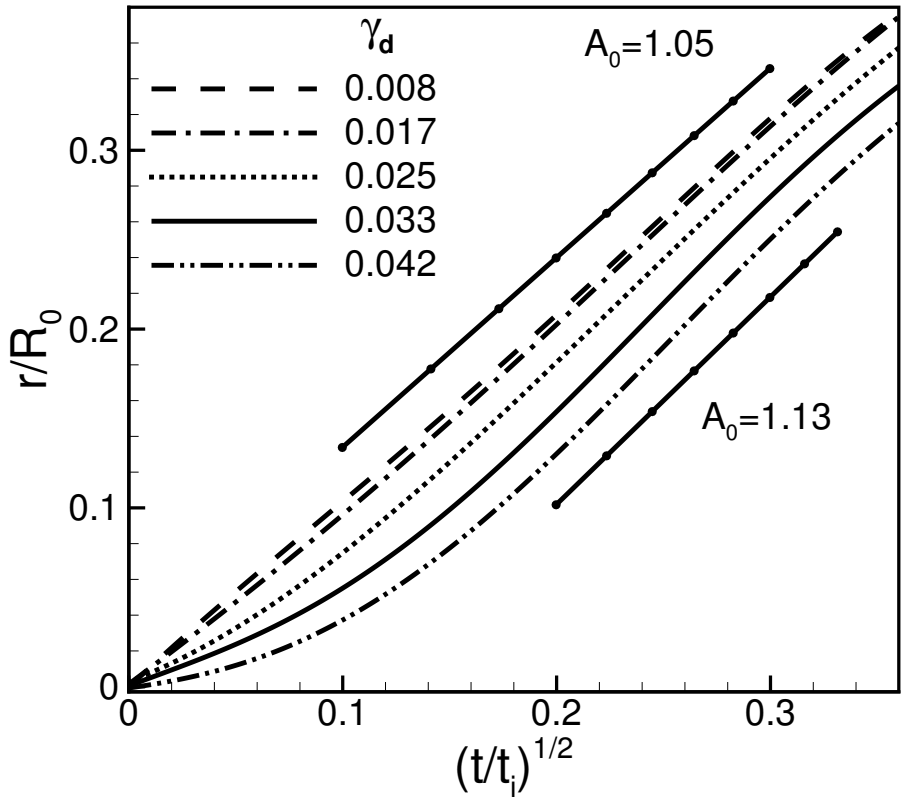

Figure 6.7: Effects of initial separation distance ($\gamma_d = d/R_0$) on the growth of the neck bridge radius (r/R_0).

A_0	$\rho_h(kg/m^3)$	$\mu_h(N \cdot s/m^2)$	$\sigma(N/m^2)$	$R_0(mm)$
1.24 [175]	931	5.0×10^{-3}	0.020	2.0
1.11 [175]	750	2.0×10^{-2}	0.020	2.0
1.14 [175]	1000	1.0×10^{-3}	0.073	2.0
1.29 ± 0.05 [179]	792	5.9×10^{-4}	0.023	1.94
1.09 ± 0.08 [179]	1000	1.0×10^{-3}	0.073	1.94
1.03 ± 0.07 [179]	1160	1.44×10^{-2}	0.067	1.94

Table 6.4: Table list of prefactor A_0 from literature.

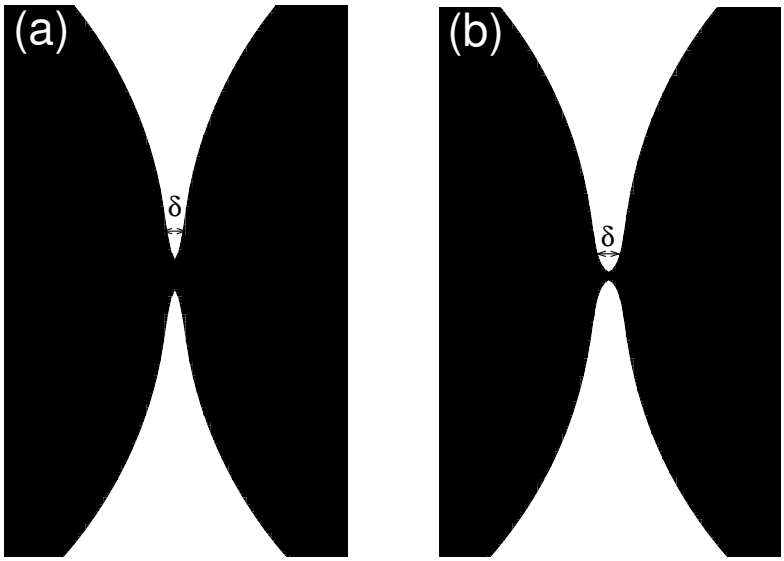

Figure 6.8: Effects of initial separation distance on the formation of elongated neck bridge in horizontal direction, (a) $\gamma_d = 0.008$ and (b) $\gamma_d = 0.042$

6.6 Conclusion

The effects of two initial set-ups, i.e., separated and connected bubbles have been studied respectively, on the neck bridge evolution using the LBM. Simulation results show the two initial conditions have a significant influence on the neck growth, thus the coalescence dynamics. In both initial scenarios, the neck bridge evolution exhibits half power-law scaling, $r/R_0 = A_0(t/t_i)^{1/2}$ after development time. The half power-law agrees with the recent analytical prediction and experimental results. It has been found that small initial separation distance or small initial neck bridge radius results in faster growth of neck bridge and bubble coalescence, which is similar to the effects of these two initial scenarios on droplet coalescence. The physical mechanism behind the development time is explored. For the initial connected case, smaller neck bridge radius corresponds to a steeper meniscus at the liquid side, leading significantly larger curvature of meniscus than that of neck bridge. The development time is to lessen the significant bias and enable contributions from both curvatures of meniscus and neck bridge to capillary forces. Whereas for the initial separated case, the thinning of liquid film between two bubbles causes elongated neck bridge in the

approaching direction of two bubbles due to the intermolecular attraction. In the range of intermolecular attraction, smaller separation distance leads a steeper meniscus (equivalent to larger curvature or larger capillary force. This explains why smaller separation distance shows faster neck growth. Meanwhile, smaller separation distance forms smaller elongated neck bridge, thus causes shorter development time to start the half power-law scaling. The values of the prefactor A_0 in the power-law scaling for all the cases are in good agreement with experimental results. These simulation results are expected to provide informative guidance for initial set-up of numerical simulation of bubble coalescence.

7. SUMMARY

The objectives of dissertation include enhancing computational skills related to the GPU parallel acceleration and understanding underlying physical of bubble coalescence in the microchannel.

In the computational skills part, a framework of the GPU parallelism and acceleration for a sophisticated free energy LBM model based on the Cahn-Hilliard diffuse interface approach is developed. Compared with serial CPU, the acceleration is up to 1000 with Tesla P100 GPU card. Meanwhile, the multi-GPU algorithm is developed for the cases with high resolution. The acceleration rapidly increases compared with a single GPU.

We get several investigations in the global process of bubble coalescence of the physical analysis part.

- **Spatial/Temporal behaviors of bubble coalescence:** there are two distinct phenomena of bubble coalescence, including oscillation (underdamping) and without oscillation (overdamping). From the test cases, the regimes for the different phenomenon is investigated. Underdamping occurs when $Oh < 0.477$. Whereas, the overdamping phenomena can be observed when $Oh > 0.477$.

  - The mechanism for underdamping is explored in terms of the competition of the surface tension driving and viscous resisting. When $Oh < 0.477$, the viscous force is small, thus energy dissipation is insignificant. The bubble coalescence is dominated by the surface tension force. The transformation between the surface energy and kinetic energy with energy dissipation causes the damped oscillation of microbubble coalescence. Smaller Oh number case possesses more useful surface energy to drive stronger oscillation.
  - There is a spatial power-law relation between the preferential relative distance and size inequality for overdamping cases. Meanwhile, we found that the coa-

lescence time is also correlated to the size inequality through a power-law relation presented as $T/t_i = A_0\gamma^{-n}$ when the air bubble coalescence in the oil. The temporal scaling is general for the global process of bubble coalescence. Both the inertial and viscous affect the prefactor A_0 (represents the coalescence time of equal bubbles) and n(indicates the quickness of coalescence from equal to unequal bubble coalescence) Oh number has a linear relationship with A_0, and n when $Oh < 0.66$. If $Oh > 0.66$, the power index tends to be a constant 0.9.

- **Coalescence-induced detachment of bubble coalescence**: coalescence-induced detachment phenomena will be observed when taking the solid boundary into consideration. Both the size inequality and father bubble size have effects on the coalescence-induced detachment phenomena. When bubble size ratio is close to 1 and the father bubble size is larger, the coalescence-induced detachment phenomena is easy to be observed.

- **Effects of the initial conditions**: faster neck growth corresponding to smaller initial neck radius is due to the significant bias between the capillary forces contributed by the meniscus curvature and the neck bridge curvature; whereas in the case of the initial separated scenario, faster growth corresponded to shorter separation distance due to the formation of elongated neck bridge.

REFERENCES

REFERENCES

[1] G. Whitesides, "The origins and the future of microfluidics," *Nature*, vol. 442, no. 7101, p. 368, 2006.

[2] D. Chiu, D. Di Carlo, P. Doyle, C. Hansen, R. Maceiczyk, R. Wootton *et al.*, "Small but perfectly formed? successes, challenges, and opportunities for microfluidics in the chemical and biological sciences," *Chem*, vol. 2, no. 2, pp. 201–223, 2017.

[3] P. Yager, T. Edwards, E. Fu, K. Helton, K. Nelson, M. Tam, and B. Weigl, "Microfluidic diagnostic technologies for global public health," *Nature*, vol. 442, no. 7101, p. 412, 2006.

[4] K. Lien and G. Lee, "Miniaturization of molecular biological techniques for gene assay," *Analyst*, vol. 135, no. 7, pp. 1499–1518, 2010.

[5] D. Beebe, G. Mensing, and G. Walker, "Physics and applications of microfluidics in biology," *Annual review of biomedical engineering*, vol. 4, no. 1, pp. 261–286, 2002.

[6] D. Holmes and S. Gawad, "The application of microfluidics in biology," in *Microengineering in biotechnology*. Springer, 2010, pp. 55–80.

[7] K. Ohno, K. Tachikawa, and A. Manz, "Microfluidics: applications for analytical purposes in chemistry and biochemistry," *Electrophoresis*, vol. 29, no. 22, pp. 4443–4453, 2008.

[8] A. Theberge, F. Courtois, Y. Schaerli, M. Fischlechner, C. Abell, F. Hollfelder, and W. Huck, "Microdroplets in microfluidics: an evolving platform for discoveries in chemistry and biology," *Angewandte Chemie International Edition*, vol. 49, no. 34, pp. 5846–5868, 2010.

[9] B. Kirby, *Micro-and nanoscale fluid mechanics: transport in microfluidic devices*. Cambridge university press, 2010.

[10] C. Lee, C. Chang, Y. Wang, and L. Fu, "Microfluidic mixing: a review," *International journal of molecular sciences*, vol. 12, no. 5, pp. 3263–3287, 2011.

[11] V. Hessel, H. Löwe, and F. Schönfeld, "Micromixers—a review on passive and active mixing principles," *Chemical Engineering Science*, vol. 60, no. 8-9, pp. 2479–2501, 2005.

[12] B. Weigl and P. Yager, "Microfluidic diffusion-based separation and detection," *Science*, vol. 283, no. 5400, pp. 346–347, 1999.

[13] X. Xue, M. Patel, M. Kersaudy-Kerhoas, M. Desmulliez, C. Bailey, and D. Topham, "Analysis of fluid separation in microfluidic t-channels," *Applied Mathematical Modelling*, vol. 36, no. 2, pp. 743–755, 2012.

[14] D. Huh, W. Gu, Y. Kamotani, J. Grotberg, and S. Takayama, "Microfluidics for flow cytometric analysis of cells and particles," *Physiological measurement*, vol. 26, no. 3, p. R73, 2005.

[15] B. Helmke and A. Minerick, "Designing a nano-interface in a microfluidic chip to probe living cells: challenges and perspectives," *Proceedings of the National Academy of Sciences*, vol. 103, no. 17, pp. 6419–6424, 2006.

[16] A. Demello, "Control and detection of chemical reactions in microfluidic systems." *Nature*, vol. 442, no. 7101, pp. 394–402, 2006.

[17] R. Pawell, R. Taylor, K. Morris, and T. Barber, "Automating microfluidic part verification," *Microfluidics and Nanofluidics*, vol. 18, no. 4, pp. 657–665, 2015.

[18] J. Khandurina, T. E. McKnight, S. C. Jacobson, L. C. Waters, R. S. Foote, and J. M. Ramsey, "Integrated system for rapid pcr-based dna analysis in microfluidic devices," *Analytical Chemistry*, vol. 72, no. 13, pp. 2995–3000, 2000.

[19] A. Hopwood, C. Hurth, J. Yang, Z. Cai, N. Moran, J. Lee-Edghill, A. Nordquist, R. Lenigk, M. Estes, J. Haley *et al.*, "Integrated microfluidic system for rapid forensic dna analysis: sample collection to dna profile," *Analytical chemistry*, vol. 82, no. 16, pp. 6991–6999, 2010.

[20] R. Pawell, D. Inglis, T. Barber, and R. Taylor, "Manufacturing and wetting low-cost microfluidic cell separation devices," *Biomicrofluidics*, vol. 7, no. 5, p. 056501, 2013.

[21] C. Shields IV, C. Reyes, and G. López, "Microfluidic cell sorting: a review of the advances in the separation of cells from debulking to rare cell isolation," *Lab on a Chip*, vol. 15, no. 5, pp. 1230–1249, 2015.

[22] C. Meinhart and H. Zhang, "The flow structure inside a microfabricated inkjet printhead," *Journal of microelectromechanical systems*, vol. 9, no. 1, pp. 67–75, 2000.

[23] J. Feng, J. Yuan, and S. Cho, "Micropropulsion by an acoustic bubble for navigating microfluidic spaces," *Lab on a Chip*, vol. 15, no. 6, pp. 1554–1562, 2015.

[24] J. Kobayashi, Y. Mori, K. Okamoto, R. Akiyama, M. Ueno, T. Kitamori, and S. Kobayashi, "A microfluidic device for conducting gas-liquid-solid hydrogenation reactions," *Science*, vol. 304, no. 5675, pp. 1305–1308, 2004.

[25] L. Zhu, N. Kroodsma, J. Yeom, J. Haan, M. Shannon, and D. Meng, "An on-demand microfluidic hydrogen generator with self-regulated gas generation and self-circulated reactant exchange with a rechargeable reservoir," *Microfluidics and nanofluidics*, vol. 11, no. 5, pp. 569–578, 2011.

[26] E. Selli, G. Chiarello, E. Quartarone, P. Mustarelli, I. Rossetti, and L. Forni, "A photocatalytic water splitting device for separate hydrogen and oxygen evolution," *Chemical communications*, no. 47, pp. 5022–5024, 2007.

[27] M. Walter, E. Warren, J. McKone, S. Boettcher, Q. Mi, E. Santori, and N. Lewis, "Solar water splitting cells," *Chemical reviews*, vol. 110, no. 11, pp. 6446–6473, 2010.

[28] C. Muhich, B. Ehrhart, I. Al-Shankiti, B. Ward, C. Musgrave, and A. Weimer, "A review and perspective of efficient hydrogen generation via solar thermal water splitting," *Wiley Interdisciplinary Reviews: Energy and Environment*, vol. 5, no. 3, pp. 261–287, 2016.

[29] J. Ditzig, H. Liu, and B. Logan, "Production of hydrogen from domestic wastewater using a bioelectrochemically assisted microbial reactor (beamr)," *International Journal of Hydrogen Energy*, vol. 32, no. 13, pp. 2296–2304, 2007.

[30] B. Logan, D. Call, S. Cheng, H. Hamelers, T. Sleutels, A. Jeremiasse, and R. Rozendal, "Microbial electrolysis cells for high yield hydrogen gas production from organic matter," *Environmental science & technology*, vol. 42, no. 23, pp. 8630–8640, 2008.

[31] B. Logan, "Scaling up microbial fuel cells and other bioelectrochemical systems," *Applied microbiology and biotechnology*, vol. 85, no. 6, pp. 1665–1671, 2010.

[32] K. Khoshmanesh, A. Almansouri, H. Albloushi, P. Yi, R. Soffe, and K. Kalantar-Zadeh, "A multi-functional bubble-based microfluidic system," *Scientific reports*, vol. 5, p. 9942, 2015.

[33] K. Akita and F. Yoshida, "Bubble size, interfacial area, and liquid-phase mass transfer coefficient in bubble columns," *Industrial & Engineering Chemistry Process Design and Development*, vol. 13, no. 1, pp. 84–91, 1974.

[34] S. Karakashev, P. Nguyen, R. Tsekov, M. Hampton, and A. Nguyen, "Anomalous ion effects on rupture and lifetime of aqueous foam films formed from monovalent salt solutions up to saturation concentration," *Langmuir*, vol. 24, no. 20, pp. 11 587–11 591, 2008.

[35] S. Ghaemi, P. Rahimi, and D. Nobes, "The effect of gas-injector location on bubble formation in liquid cross flow," *Physics of Fluids*, vol. 22, no. 4, p. 043305, 2010.

[36] K. Wang, Y. Lu, L. Yang, and G. Luo, "Microdroplet coalescences at microchannel junctions with different collision angles," *AIChE Journal*, vol. 59, no. 2, pp. 643–649, 2013.

[37] T. Wang, J. Wang, and Y. Jin, "Theoretical prediction of flow regime transition in bubble columns by the population balance model," *Chemical Engineering Science*, vol. 60, no. 22, pp. 6199–6209, 2005.

[38] R. Revellin, B. Agostini, and J. Thome, "Elongated bubbles in microchannels. part ii: Experimental study and modeling of bubble collisions," *International Journal of Multiphase Flow*, vol. 34, no. 6, pp. 602–613, 2008.

[39] Y. Liao, R. Rzehak, D. Lucas, and E. Krepper, "Baseline closure model for dispersed bubbly flow: Bubble coalescence and breakup," *Chemical Engineering Science*, vol. 122, pp. 336–349, 2015.

[40] M. Firouzi, T. Howes, and A. Nguyen, "A quantitative review of the transition salt concentration for inhibiting bubble coalescence," *Advances in colloid and interface science*, vol. 222, pp. 305–318, 2015.

[41] C. Henry and V. Craig, "The link between ion specific bubble coalescence and hofmeister effects is the partitioning of ions within the interface," *Langmuir*, vol. 26, no. 9, pp. 6478–6483, 2010.

[42] D. Chan, E. Klaseboer, and R. Manica, "Film drainage and coalescence between deformable drops and bubbles," *Soft Matter*, vol. 7, no. 6, pp. 2235–2264, 2011.

[43] C. Curschellas, D. Gunes, H. Deyber, B. Watzke, E. Windhab, and H. Limbach, "Interfacial aspects of the stability of polyglycerol ester covered bubbles against coalescence," *Soft Matter*, vol. 8, no. 46, pp. 11 620–11 631, 2012.

[44] J. KIM and W. LEE, "Coalescence behavior of two bubbles in stagnant liquids." *Journal of Chemical Engineering of Japan*, vol. 20, no. 5, pp. 448–453, 1987.

[45] J. Kim and W. Lee, "Coalescence behavior of two bubbles growing side-by-side," *Journal of colloid and interface science*, vol. 123, no. 1, pp. 303–305, 1988.

[46] H. Kavehpour, "Coalescence of drops," *Annual Review of Fluid Mechanics*, vol. 47, pp. 245–268, 2015.

[47] J. Eggers, J. Lister, and H. Stone, "Coalescence of liquid drops," *Journal of Fluid Mechanics*, vol. 401, pp. 293–310, 1999.

[48] G. Charles and S. Mason, "The coalescence of liquid drops with flat liquid/liquid interfaces," *Journal of Colloid Science*, vol. 15, no. 3, pp. 236–267, 1960.

[49] H. Aryafar and H. Kavehpour, "Drop coalescence through planar surfaces," *Physics of Fluids*, vol. 18, no. 7, p. 072105, 2006.

[50] A. Menchaca-Rocha, A. Martínez-Dávalos, R. Nunez, S. Popinet, and S. Zaleski, "Coalescence of liquid drops by surface tension," *Physical Review E*, vol. 63, no. 4, p. 046309, 2001.

[51] L. Duchemin, J. Eggers, and C. Josserand, "Inviscid coalescence of drops," *Journal of Fluid Mechanics*, vol. 487, pp. 167–178, 2003.

[52] S. Thoroddsen, T. Etoh, K. Takehara, and N. Ootsuka, "On the coalescence speed of bubbles," *Physics of Fluids*, vol. 17, no. 7, p. 071703, 2005.

[53] J. Sprittles and Y. Shikhmurzaev, "A parametric study of the coalescence of liquid drops in a viscous gas," *Journal of Fluid Mechanics*, vol. 753, pp. 279–306, 2014.

[54] J. Paulsen, R. Carmigniani, A. Kannan, J. Burton, and S. Nagel, "Coalescence of bubbles and drops in an outer fluid," *Nature Communications*, vol. 5, pp. 3182–3199, 2014.

[55] T. Tsukada, M. Sato, N. Imaishi, M. Hozawa, and K. Fujikawa, "A theoretical and experimental study on the oscillation of a hanging drop," *Journal of chemical engineering of Japan*, vol. 20, no. 1, pp. 88–93, 1987.

[56] D. Gaitan, L. Crum, C. Church, and R. Roy, "Sonoluminescence and bubble dynamics for a single, stable, cavitation bubble," *The Journal of the Acoustical Society of America*, vol. 91, no. 6, pp. 3166–3183, 1992.

[57] I. Akhatov, O. Lindau, A. Topolnikov, R. Mettin, N. Vakhitova, and W. Lauterborn, "Collapse and rebound of a laser-induced cavitation bubble," *Physics of Fluids*, vol. 13, no. 10, pp. 2805–2819, 2001.

[58] N. Matsuki, S. Ichiba, T. Ishikawa, O. Nagano, M. Takeda, Y. Ujike, and T. Yamaguchi, "Blood oxygenation using microbubble suspensions," *European Biophysics Journal*, vol. 41, no. 6, pp. 571–578, 2012.

[59] G. Kaushik and A. Chel, "Microbubble technology: emerging field for water treatment," *Bubble Science, Engineering & Technology*, vol. 5, no. 1-2, pp. 33–38, 2014.

[60] L. Chew, E. Klaseboer, S. Ohl, and B. Khoo, "Interaction of two differently sized oscillating bubbles in a free field," *Physical Review E*, vol. 84, no. 6, p. 066307, 2011.

[61] A. Prosperetti, "Linear oscillations of constrained drops, bubbles, and plane liquid surfaces," *Physics of fluids*, vol. 24, no. 3, p. 032109, 2012.

[62] L. Rayleigh, "On the capillary phenomena of jets," *Proc. R. Soc. London*, vol. 29, no. 196-199, pp. 71–97, 1879.

[63] H. Lamb, *Hydrodynamics*. Cambridge university press, 1932.

[64] C. Miller and L. Scriven, "The oscillations of a fluid droplet immersed in another fluid," *Journal of Fluid Mechanics*, vol. 32, no. 3, pp. 417–435, 1968.

[65] A. Prosperetti, "Free oscillations of drops and bubbles: the initial-value problem," *Journal of Fluid Mechanics*, vol. 100, no. 2, pp. 333–347, 1980.

[66] O. Basaran, "Nonlinear oscillations of viscous liquid drops," *Journal of Fluid Mechanics*, vol. 241, pp. 169–198, 1992.

[67] I. Vakarelski, R. Manica, X. Tang, S. O'Shea, G. Stevens, F. Grieser, R. Dagastine, D. Chan *et al.*, "Dynamic interactions between microbubbles in water," *PNAS*, vol. 107, no. 25, pp. 11 177–11 182, 2010.

[68] L. Yang, K. Wang, J. Tan, Y. Lu, and G. Luo, "Experimental study of microbubble coalescence in a t-junction microfluidic device," *Microfluid Nanofluid*, vol. 12, pp. 715–722, 2012.

[69] Y. Kim, S. Lim, B. Gim, and B. Weon, "Coalescence preference in densely packed microbubbles," *Scientific Reports*, vol. 5, p. 7739, 2015.

[70] B. Weon and J. Je, "Coalescence preference depends on size inequality," *Physical review letters*, vol. 108, no. 22, p. 224501, 2012.

[71] R. Stover, C. Tobias, and M. Denn, "Bubble coalescence dynamics," *AIChE J*, vol. 43, no. 10, pp. 2385–2392, 1997.

[72] J. Sprittles and Y. Shikhmurzaev, "Coalescence of liquid drops: Different models versus experiment," *Physics of Fluids*, vol. 24, no. 12, p. 122105, 2012.

[73] U. Frisch, B. Hasslacher, and Y. Pomeau, "Lattice-gas automata for the navier-stokes equation," *Physical review letters*, vol. 56, no. 14, p. 1505, 1986.

[74] S. Wolfram, "Cellular automaton fluids 1: Basic theory," *Journal of statistical physics*, vol. 45, no. 3, pp. 471–526, 1986.

[75] P. Bhatnagar, E. Gross, and M. Krook, "A model for collision processes in gases. I. small amplitude processes in charged and neutral one-component systems," *Physical Review*, vol. 94, no. 3, pp. 511–525, 1954.

[76] X. He and L. Luo, "A priori derivation of the lattice Boltzmann equation," *Physical Review E*, vol. 55, no. 6, pp. R6833–R6336, 1997.

[77] ——, "Theory of lattice Boltzmann method: From the Boltzmann equation to the lattice Boltzmann equation," *Physical Review E*, vol. 56, no. 12, pp. 6811–6817, 1997.

[78] ——, "Lattice Boltzmann model for the incompressible Navier-Stokes equation," *Journal of Statistical Physics*, vol. 88, no. 3–4, pp. 927–944, 1997.

[79] S. Chen and G. Doolen, "Lattice Boltzmann method for fluid flows," *Annual Review of Fluid Mechanics*, vol. 30, pp. 329–364, 1998.

[80] C. Aidun and J. Clausen, "Lattice-Boltzmann method for complex flows," *Annual Review of Fluid Mechanics*, pp. 439–472, 2010.

[81] K. Andrew K. Gunstensen, H. Daniel H Rothman, S. Zaleski, and G. Zanetti, "Lattice Boltzmann model of immiscible fluids," *Phys. Rev. A*, vol. 43, pp. 4320–27, 1991.

[82] X. Shan and H. Chen, "Lattice Boltzmann model for simulating flows with multiphases and components," *Physical Review E*, vol. 47, pp. 1815–1819, 1993.

[83] ——, "Simulation of nonideal gases and liquid-gas phase transitions by the lattice Boltzmann equation," *Physical Review E*, vol. 49, no. 4, pp. 2941–2948, 1994.

[84] X. He, X. Shan, and G. Doolen, "Discrete Boltzmann equation model for nonideal gases," *Physical Review E*, vol. 57, p. R13, 1998.

[85] X. He, S. Chen, and R. Zhang, "A lattice boltzamnn scheme for incompressible multiphase flow and its application in simulation of Rayleigh-Taylor instability," *J. Comp. Phys.*, vol. 152, 1999.

[86] M. Swift, W. Osborn, and J. Yeomans, "Lattice Boltzmann simulation of nonideal fluids," *Phys. Rev. Let.*, vol. 75, no. 5, pp. 830–833, 1995.

[87] M. Swift, E. Orlandini, W. Osborn, and J. Yeomans, "Lattice Boltzmann simulations of liquid-gas and binary fluid systems," *Physical Review E*, vol. 54, no. 5, pp. 5041–5052, 1996.

[88] A. Mazloomi M, S. Chikatamarla, and I. Karlin, "Entropic lattice Boltzmann method for multiphase flows," *Phys. Rev. Lett.*, vol. 114, p. 174502, 2015.

[89] L. Chen, Q. Qinjun Kang, Y. Mua, Y.-L. He, and W.-Q. Tao, "A critical review of the pseudopotential multiphase lattice Boltzmann model: Methods and applications," *International Journal of Heat and Mass Transfer*, vol. 76, pp. 210 – 236, 2014.

[90] K. Connington and T. Lee, "A review of spurious currents in the lattice Boltzmann method for multiphase flows," *Journal of Mechanical Science and Technology*, vol. 26, no. 12, pp. 3857–3863, 2012.

[91] Q. Kang, D. Zhang, and S. Chen, "Displacement of a three-dimensional immiscible droplet in a duct," *Journal of Fluid Mechanics*, vol. 545, pp. 41–66, 2005.

[92] H. Huang, D. Thorne Jr, M. Schaap, and M. Sukop, "Proposed approximation for contact angles in shan-and-chen-type multicomponent multiphase lattice Boltzmann models," *Physical Review E*, vol. 76, no. 6, p. 066701, 2007.

[93] M. Schaap, M. Porter, B. Christensen, and D. Wildenschild, "Comparison of pressure-saturation characteristics derived from computed tomography and lattice boltzmann simulations," *Water Resources Research*, vol. 43, no. 12, 2007.

[94] M. Latva-Kokko and D. Rothman, "Static contact angle in lattice boltzmann models of immiscible fluids," *Physical Review E*, vol. 72, no. 4, p. 046701, 2005.

[95] A. Briant, A. Wagner, and J. Yeomans, "Lattice boltzmann simulations of contact line motion. i. liquid-gas systems," *Physical Review E*, vol. 69, no. 3, p. 031602, 2004.

[96] A. Dupuis and J. Yeomans, "Lattice boltzmann modelling of droplets on chemically heterogeneous surfaces," *Future Generation Computer Systems*, vol. 20, no. 6, pp. 993–1001, 2004.

[97] A. Yiotis, J. Psihogios, M. Kainourgiakis, A. Papaioannou, and A. Stubos, "A lattice boltzmann study of viscous coupling effects in immiscible two-phase flow in porous media," *Colloids and Surfaces A: Physicochemical and Engineering Aspects*, vol. 300, no. 1-2, pp. 35–49, 2007.

[98] L. Wang, H. Huang, and X. Lu, "Scheme for contact angle and its hysteresis in a multiphase lattice boltzmann method," *Physical Review E*, vol. 87, no. 1, p. 013301, 2013.

[99] H. Huang, M. Sukop, and X. Lu, *Multiphase lattice Boltzmann methods: Theory and application*. John Wiley & Sons, 2015.

[100] L. Liu and T. Lee, "Wall free energy based polynomial boundary conditions for non-ideal gas lattice Boltzmann equation," *International Journal of Modern Physics C*, vol. 20, no. 11, pp. 1749–1768, 2009.

[101] T. Lee and C.-L. Lin, "A stable discretization of the lattice Boltzmann equation for simulation of incompressible two-phase flows at high density ratio," *J. Comp. Phys.*, vol. 206, no. 10, pp. 16 – 47, 2005.

[102] T. Lee and P. Fischer, "Eliminating parasitic currents in the lattice Boltzmann equation method for nonideal gases," *Physical Review E*, vol. 74, no. 4, p. 046709, 2006.

[103] T. Lee, "Effects of incompressibility on the elimination of parasitic currents in the lattice Boltzmann equation method for binary fluids," *Computers and Mathematics with Applications*, vol. 58, pp. 987 – 994, 2009.

[104] T. Lee and L. Liu, "Lattice Boltzmann simulations of micron-scale drop impact on dry surfaces," *J Comp Phys*, vol. 229, pp. 8045–8063, 2010.

[105] W. Li, X. Wei, and A. Kaufman, "Implementing lattice boltzmann computation on graphics hardware," *The Visual Computer*, vol. 19, no. 7, pp. 444–456, 2003.

[106] NVIDIA Corporation, "Cuda zone," https://developer.nvidia.com/cuda-zone.

[107] S. Ryoo, C. Rodrigues, S. Baghsorkhi, S. Stone, D. Kirk, and W. Hwu, "Optimization principles and application performance evaluation of a multithreaded gpu using cuda," in *Proceedings of the 13th ACM SIGPLAN Symposium on Principles and practice of parallel programming*. ACM, 2008, pp. 73–82.

[108] J. Henning, "Spec cpu2006 benchmark descriptions. acm sigarch comput archit news 34 (4): 1–17," 2006.

[109] M. Wittmann, T. Zeiser, G. Hager, and G. Wellein, "Comparison of different propagation steps for lattice boltzmann methods," *Computers & Mathematics with Applications*, vol. 65, no. 6, pp. 924–935, 2013.

[110] J. Tölke and M. Krafczyk, "TeraFLOP computing on a desktop PC with GPUs for 3D CFD," *International Journal of Computational Fluid Dynamics*, vol. 22, no. 7, pp. 443–456, 2008.

[111] J. Tölke, "Implementation of a lattice Boltzmann kernel using the compute unified device architecture developed by NVIDIA," *Computing and Visualization in Science*, vol. 13, no. 1, pp. 29–39, 2010.

[112] P. Bailey, J. Myre, S. Walsh, D. Lilja, and M. Saar, "Accelerating lattice boltzmann fluid flow simulations using graphics processors," in *Parallel Processing, 2009. ICPP'09. International Conference on*. IEEE, 2009, pp. 550–557.

[113] C. Obrecht, F. Kuznik, B. Tourancheau, and J. Roux, "A new approach to the lattice Boltzmann method for graphics processing units," *Computers & Mathematics with Applications*, vol. 61, no. 12, pp. 3628–3638, 2011.

[114] N. Tran, M. Lee, and S. Hong, "Performance optimization of 3d lattice boltzmann flow solver on a gpu," *Scientific Programming*, vol. 2017, 2017.

[115] G. Herschlag, S. Lee, J. S. Vetter, and A. Randles, "Gpu data access on complex geometries for d3q19 lattice boltzmann method," in *2018 IEEE International Parallel and Distributed Processing Symposium (IPDPS)*. IEEE, 2018, pp. 825–834.

[116] "CUDA Toolkit Documentation," http://docs.nvidia.com/cuda/index.html, accessed: September 2015.

[117] O. Navarro-Hinojosa, S. Ruiz-Loza, and M. Alencastre-Miranda, "Physically based visual simulation of the lattice boltzmann method on the gpu: a survey," *The Journal of Supercomputing*, vol. 74, pp. 3441–3467, 2018.

[118] X. Li, Y. Zhang, X. Wang, and W. Ge, "Gpu-based numerical simulation of multi-phase flow in porous media using multiple-relaxation-time lattice boltzmann method," *Chemical Engineering Science*, vol. 102, pp. 209–219, 2013.

[119] M. Januszewski and M. Kostur, "Sailfish: A flexible multi-gpu implementation of the lattice boltzmann method," *Computer Physics Communications*, vol. 185, no. 9, pp. 2350–2368, 2014.

[120] T. Huang, C. Chang, and C. Lin, "Simulation of droplet dynamic with high density ratio two-phase lattice boltzmann model on multi-gpu cluster," *Computers & Fluids*, vol. 173, pp. 80–87, 2018.

[121] C. Obrecht, F. Kuznik, B. Tourancheau, and J. Roux, "Multi-gpu implementation of the lattice boltzmann method," *Computers & Mathematics with Applications*, vol. 65, no. 2, pp. 252–261, 2013.

[122] B. Zigon, L. Zhu, and F. Song, "Interactive 3d simulation for fluid–structure interactions using dual coupled GPUs," *The Journal of Supercomputing*, vol. 74, no. 1, pp. 37–64, 2018.

[123] J. Myre, S. Walsh, D. Lilja, and M. Saar, "Performance analysis of single-phase, multiphase, and multicomponent lattice-Boltzmann fluid flow simulations on GPU clusters," *Concurrency and Computation: Practice and Experience*, vol. 23, no. 4, pp. 332–350, 2011.

[124] W. Xian and A. Takayuki, "Multi-GPU performance of incompressible flow computation by lattice Boltzmann method on GPU cluster," *Parallel Computing*, vol. 37, no. 9, pp. 521–535, 2011.

[125] S. Blair, C. Albing, A. Grund, and A. Jocksch, "Accelerating an mpi lattice boltzmann code using openacc," in *Proceedings of the second workshop on accelerator programming using directives*. ACM, 2015, p. 3.

[126] S. Succi, *The Lattice Boltzmann Equation for Fluid Dynamics and Beyond*. Oxford University Press, 2001.

[127] S. Chen, D. Martinez, and R. Mei, "On boundary conditions in lattice boltzmann methods," *Physics of fluids*, vol. 8, no. 9, pp. 2527–2536, 1996.

[128] Z. Guo and T. Zhao, "Lattice boltzmann model for incompressible flows through porous media," *Physical Review E*, vol. 66, no. 3, p. 036304, 2002.

[129] J. Cahn and J. Hilliard, "Free energy of a nonuniform system. I. Interfacial free energy," *J. Chem. Phys.*, vol. 28, pp. 258 – 266, 1958.

[130] D. Anderson, G. McFadden, and A. Wheeler, "Diffus-interface method in fluid mechanics," *Annu. Rev. Fluid Mech.*, vol. 30, pp. 139 – 165, 1998.

[131] D. Jacqmin, "Calculation of two-phase Navier-Stokes flows using phase-field modeling," *J. Comp. Phys.*, vol. 155, no. 10, pp. 96 – 127, 1999.

[132] J. Rowlinson and B. Widom, *Molecular Theory of Capillarity*. Oxford Univ. Press, Oxford, UK, 1989.

[133] H. Ding, P. Spelt, and C. Shu, "Diffuse interface model for incompressible two-phase flows with large density ratios," *J. Comp. Phys.*, vol. 226, no. 10, pp. 2078 – 2095, 2007.

[134] M. o. Carpinlioğlu and M. Gündoğdu, "A critical review on pulsatile pipe flow studies directing towards future research topics," *Flow Meas. Instrum.*, vol. 12, no. 3, pp. 163–174, 2001.

[135] D. Jamet, O. Lebaigue, N. Coutris, and J. Delhaye, "The second gradient method for the direct numerical simulation of liquid–vapor flows with phase change," *Journal of Computational Physics*, vol. 169, no. 2, pp. 624–651, 2001.

[136] M. Day and J. Bell, "Numerical simulation of laminar reacting flows with complex chemistry," *Combust. Theory Model.*, vol. 4, pp. 535 – 556, 2000.

[137] J. Yang, D. Hubball, M. Ward, E. Rundensteiner, and W. Ribarsky, "Value and relation display: Interactive visual exploration of large datasets with hundreds of dimensions," *IEEE Transactions on Visualization and Computer Graphics*, vol. 13, no. 3, pp. 494–507, 2007.

[138] N. Chen and H. Yu, "Mechanism of axis switching in low aspect-ratio rectangular jets," *Computer & Mathematics with Applications*, vol. 67, no. 2, pp. 437–444, 2014.

[139] Z. Wang, N. Chen, Y. Zhao, and H. Yu, "GPU-accelerated lattice Boltzmann method for extracting real biomechanical geometry and volumetric boundary condition," *Computers & Fluids*, vol. 115, pp. 192–200, 2015.

[140] S. An, H. Yu, Z. Wang, R. Chen, B. Kapadia, and J. Yao, "Unified mesoscopic modeling and GPU-accelerated computational method for image-based pore-scale porous media flows," *Int. J. of Heat Mass Trans.*, vol. 115, pp. 1192 – 1202, 2017.

[141] S. An, H. Yu, and J. Yao, "GPU-accelerated volumetric lattice Boltzmann method for porous media flow," *J. Petro. Sci. Eng.*, vol. 156, pp. 546 – 552, 2017.

[142] N. Delbosc, J. Summers, A. Khan, N. Kapur, and C. Noakes, "Optimized implementation of the lattice boltzmann method on a graphics processing unit towards real-time fluid simulation," *Computers & Mathematics with Applications*, vol. 67, no. 2, pp. 462–475, 2014.

[143] J. Power, M. Hill, and D. Wood, "Supporting x86-64 address translation for 100s of gpu lanes," in *2014 IEEE 20th International Symposium on High Performance Computer Architecture (HPCA)*. IEEE, 2014, pp. 568–578.

[144] M. AL-Mashhadani, J. Wilkinson, and B. Zimmerman, "Airlift bioreactor for biological applications with microbubble mediated transport processes," *Chemical Engineering Science*, vol. 137, pp. 243 – 253, 2015.

[145] K. Terasaka, A. Hirabayashi, T. Nishino, S. Fujioka, and D. Kobayashi, "Development of microbubble aerator for waste water treatment using aerobic activated sludge," *Chemical engineering science*, vol. 66, no. 14, pp. 3172–3179, 2011.

[146] P. Dahiya, M. Caggioni, and P. Spicer, "Arrested coalescence of viscoelastic droplets: polydisperse doublets," *Phil. Trans. R. Soc. A*, vol. 374, no. 2072, p. 20150132, 2016.

[147] J. Paulsen, J. Burton, and S. Nagel, "Viscous to inertial crossover in liquid drop coalescence," *Physical Review Letters*, vol. 106, no. 11, p. 114501, 2011.

[148] R. Chen, H. Yu, and L. Zhu, "Effects of initial conditions on the coalescence of microbubbles," *Proceedings of the Institution of Mechanical Engineers, Part C: Journal of Mechanical Engineering Science*, vol. 232, no. 3, pp. 457–465, 2018.

[149] C. Anthony, P. Kamat, S. Thete, J. Munro, J. Lister, M. Harris, and O. Basaran, "Scaling laws and dynamics of bubble coalescence," *Physical Review Fluids*, vol. 2, no. 8, p. 083601, 2017.

[150] R. Chen, J. Zeng, and H. Yu, "Mechanism of damped oscillation in microbubble coalescence," *Computers & Fluids*, vol. 183, pp. 38–42, 2019.

[151] A. Agarwal, W. Ng, and Y. Liu, "Principle and applications of microbubble and nanobubble technology for water treatment," *Chemosphere*, vol. 84, no. 9, pp. 1175 – 1180, 2011.

[152] Y. Qian, "Fractional propagation and the elimination of staggered invariants in lattice-BGK models," *International Journal of Modern Physics C*, vol. 08, no. 04, pp. 753–761, 1997.

[153] J. Munro, C. Anthony, O. Basaran, and J. Lister, "Thin-sheet flow between coalescing bubbles," *Journal of Fluid Mechanics*, vol. 773, 2015.

[154] A. Leenheer and H. Atwater, "Water-splitting photoelectrolysis reaction rate via microscopic imaging of evolved oxygen bubbles," *Journal of The Electrochemical Society*, vol. 157, no. 9, pp. B1290–B1294, 2010.

[155] S. Garimella, T. Persoons, J. Weibel, and V. Gektin, "Electronics thermal management in information and communications technologies: Challenges and future directions," *IEEE Transactions on Components, Packaging and Manufacturing Technology*, vol. 7, no. 8, pp. 1191–1205, 2017.

[156] C. Hidrovo, T. Kramer, E. Wang, S. Vigneron, J. Steinbrenner, J. Koo, F. Wang, D. Fogg, R. Flynn, E. Lee *et al.*, "Two-phase microfluidics for semiconductor circuits and fuel cells," *Heat transfer engineering*, vol. 27, no. 4, pp. 53–63, 2006.

[157] H. Flemming, "Biofouling in water systems–cases, causes and countermeasures," *Applied microbiology and biotechnology*, vol. 59, no. 6, pp. 629–640, 2002.

[158] A. Agarwal, W. Ng, and Y. Liu, "Cleaning of biologically fouled membranes with self-collapsing microbubbles," *Biofouling*, vol. 29, no. 1, pp. 69–76, 2013.

[159] P. Sharma, M. Gibcus, H. C. Van DM, and H. Busscher, "Microbubble-induced detachment of coadhering oral bacteria from salivary pellicles," *European journal of oral sciences*, vol. 113, no. 4, pp. 326–332, 2005.

[160] K. Forster and R. Greif, "Heat transfer to a boiling liquid mechanism and correlations. progress report no. 7 (58-40)," California. Univ., Los Angeles, CA (United States). Dept. of Engineering, Tech. Rep., 1958.

[161] A. Georgoulas, M. Andredaki, and M. Marengo, "An enhanced vof method coupled with heat transfer and phase change to characterise bubble detachment in saturated pool boiling," *Energies*, vol. 10, no. 3, p. 272, 2017.

[162] Z. Douglas, T. Boziuk, M. Smith, and A. Glezer, "Acoustically enhanced boiling heat transfer," *Physics of Fluids*, vol. 24, no. 5, p. 052105, 2012.

[163] J. Chen, L. Guo, X. Hu, Z. Cao, and Y. Wang, "Dynamics of single bubble departure from TiO2 nanorod-array photoelectrode," *Electrochimica Acta*, vol. 274, pp. 57–66, 2018.

[164] E. Wang, S. Devasenathipathy, C. Hidrovo, D. Fogg, J. Koo, J. Santiago, K. Goodson, and T. Kenny, "Liquid velocity field measurements in two-phase microchannel convection," in *Proc. 3rd International Symposium on Two-Phase Flow Modeling and Experimentation*, Pisa, Italy, 9 2004.

[165] J. Xu, B. Chen, and T. Xie, "Experimental and theoretical analysis of bubble departure behavior in narrow rectangular channel," *Progress in Nuclear Energy*, vol. 77, pp. 1–10, 2014.

[166] Á. Soto, T. Maddalena, A. Fraters, D. Van Der Meer, and D. Lohse, "Coalescence of diffusively growing gas bubbles," *Journal of fluid mechanics*, vol. 846, pp. 143–165, 2018.

[167] B. Peng, S. Wang, Z. Lan, W. Xu, R. Wen, and X. Ma, "Analysis of droplet jumping phenomenon with lattice boltzmann simulation of droplet coalescence," *Applied Physics Letters*, vol. 102, no. 15, p. 151601, 2013.

[168] S. Farokhirad, J. Morris, and T. Lee, "Coalescence-induced jumping of droplet: Inertia and viscosity effects," *Physics of Fluids*, vol. 27, no. 10, p. 102102, 2015.

[169] F. Wang, F. Yang, and Y. Zhao, "Size effect on the coalescence-induced self-propelled droplet," *Applied Physics Letters*, vol. 98, no. 5, p. 053112, 2011.

[170] F. Liu, G. Ghigliotti, J. Feng, and C. Chen, "Self-propelled jumping upon drop coalescence on leidenfrost surfaces," *Journal of Fluid Mechanics*, vol. 752, pp. 22–38, 2014.

[171] K. Wang, Q. Liang, R. Jiang, Y. Zheng, Z. Lan, and X. Ma, "Numerical simulation of coalescence-induced jumping of multidroplets on superhydrophobic surfaces: Initial droplet arrangement effect," *Langmuir*, vol. 33, no. 25, pp. 6258–6268, 2017.

[172] Y. Cao, J. Bontrager-Singer, and L. Zhu, "A 3D microfluidic device fabrication method using thermopress bonding with multiple layers of polystyrene film," *Journal of Micromechanics and Microengineering*, vol. 25, no. 6, p. 065005, 2015.

[173] S. Zhou, Y. Cao, R. Chen, T. Sun, K. Fezzaa, H. Yu, and L. Zhu, "Study on coalescence dynamics of unequal-sized microbubbles captive on solid substrate," *Experimental Thermal and Fluid Science*, vol. 98, pp. 362–368, 2018.

[174] D. Chen, L. Pan, and S. Ren, "Prediction of bubble detachment diameter in flow boiling based on force analysis," *Nuclear Engineering and Design*, vol. 243, pp. 263–271, 2012.

[175] D. Aarts, H. Lekkerkerker, H. Guo, G. Wegdam, and D. Bonn, "Hydrodynamics of droplet coalescence," *Physical review letters*, vol. 95, no. 16, p. 164503, 2005.

[176] N. Bremond, H. Doméjean, and J. Bibette, "Propagation of drop coalescence in a two-dimensional emulsion: A route towards phase inversion," *Physical review letters*, vol. 106, no. 21, p. 214502, 2011.

[177] L. Baroudi, M. Kawaji, and T. Lee, "Effects of initial conditions on the simulation of inertial coalescence of two drops," *Computers & Mathematics with Applications*, vol. 67, no. 2, pp. 282–289, 2014.

[178] R. Tabor, F. Grieser, R. Dagastine, and D. Chan, "Measurement and analysis of forces in bubble and droplet systems using afm," *Journal of colloid and interface science*, vol. 371, no. 1, pp. 1–14, 2012.

[179] M. Wu, T. Cubaud, and C. Ho, "Scaling law in liquid drop coalescence driven by surface tension," *Physics of Fluids*, vol. 16, no. 7, pp. L51–L54, 2004.

VITA

VITA

Rou Chen

EDUCATION

- Doctor of Philosophy, August 2019
  Purdue University
  Department of Mechanical Engineering
- Master of Science, June 2013
  Zhejiang Normal University
  Department of Physics
- Bachelor of Science, June 2013
  Zhejiang Normal University
  Chuyang Honors College

TEACHING EXPERIENCE

- Lab instructor for mechanical lab (fluid lab) of undergraduate student.
- Co-instructor for the undergraduate course: ME200 (Thermodynamics)
- Co-instructor for the graduate courses: ME 509 (Fluid Dynamics) and ME500 (Advanced Thermodynamics)

PUBLICATIONS

1. **R. Chen**, J. Zeng, H. Yu, "Mechanism of damped oscillation in microbubble coalescence", Computers & Fluids, 2019, 183: 38-42.
2. **R. Chen**, H.Yu, Y. Xu. L. Zhu. "Scalings of Inverse Energy Transfer and Energy Decay in 3-D Decaying isotropic Turbulence with Non-rotating or Rotating Frame of Reference", Journal of Applied and Computational Mechanics, 2019, 5:639-646.

3. **R. Chen**, H. Yu, L. Zhu, “Effects of initial conditions on the coalescence of micro-bubbles”, Proceedings of the Institution of Mechanical Engineers, Part C: Journal of Mechanical Engineering Science, 2018, 232: 457-465.

4. S. Zhou, Y. Cao, **R. Chen**, T. Sun, F. Carlo, H.Yu, L. Zhu, “Study on coalescence dynamics of unequal-sized microbubbles captive on solid substrate”, Experimental thermal and fluid science, 2018, 98: 362-368.

5. B. Gelfand, J. Ambati, S. An, **R. Chen**, H. Y. Whitney, J. Yao, “Hemodynamic shear stress in the inner choroid primes endothelium for complement damage”, Investigative Ophthalmology & Visual Science, 2018, 59(9), 3473-3473.

6. **R. Chen**, H. Yu, L. Zhu, et al., “Spatial and temporal scaling of unequal microbubble coalescence”, The AIChE Journal, 2017, 63(4): 1441-1450.2.

7. B. Gelfand, S. An, H. Y. Whitney, **R. Chen**, J. Yao, J. Ambati, “Shear stress governs choroidal endothelial cell proliferation and homeostasis”, Investigative Ophthalmology & Visual Science, 2017, 58(8), 1102-11023473.

8. H.W. Yu, A. Deb, X. Chen, **R. Chen**, D. Wang, I.W. Wang, “Integration of Patient-specific Computational Hemodynamics and Vessel Wall Shear Stress Into MRI Diagnosis of Vascular Diseases”, Circulation Research, 2017, 119, A235-A235.

9. H. Yu, X. Chen, Z. Wang, **R. Chen**, C. Lin, S. F. Kralik, P. Raveena, “Integration of patient-specific computational hemodynamics and vessel wall shear stress into MRI diagnosis of vascular diseases”, Circulation Research, 2016, 119: A235.

10. H. Yu, **R. Chen**, H. Wang, et al., “GPU accelerated lattice Boltzmann simulation for rotational turbulence”, Computers & Mathematics with Applications, 2014, 67(2): 445-451.

11. **R. Chen**, Shao J, Y.Xu, “Lattice Boltzmann simulation for complex flow in a solar wall”, Communications in Theoretical Physics, 2013, 59(3): 370.

12. **R. Chen**, H. Yu, J. Zeng, L. Zhu, “General power-law temporal scaling for unequal microbubble coalescence”, Physical Review E, 2019, in revision

13. **R. Chen**, H. Yu, S. Zhou, L. Zhu, "Numerical and experimental study for 3D coalescence-induced detachment of microbubble", in preparation.

PRESENTATIONS AT PROFESSIONAL MEETINGS

Oral Presentations

1. **R. Chen**, L. Zhu, H. Yu, Detachment Dynamics Induced by Unequal Microbubble Coalescence, The 71th Annual APS-DFD meeting, Atlanta, Georgia, Nov. 2018
2. **R. Chen**, H. W. Yu, L. Zhu, Dynamics of Microbubble Coalescence Analysis Based on GPU Accelerated Lattice Boltzmann Method, The 30th International Conference on Parallel Computational Fluid Dynamics, Indianapolis, Indiana, USA, May 2018
3. **R. Chen**, H. W. Yu, L. Zhu, T. Lee, Numerical Simulation and Analysis of Size Inequality on Microbubble Coalescence, The 28th International Conference on Parallel Computational Fluid Dynamics, Kobe, Japan, May 2016
4. **R. Chen**, H. Yu, Bubble Dynamic in Micro-Channel Using Lattice Boltzmann Method, An inviting talk in Biomath Seminar in IUPUI in Nov. 2016 (invited talk)
5. **R. Chen**, W. Diao, Y. Cheng, L. Zhu, H. Yu, Lattice Boltzmann Simulation of Self-driven Bubble Transport in a Micro-channel with a Virtual Check Valve, The 68th Annual APS-DFD meeting, Boston, Massachusetts, Nov. 2015

Posters

1. H.Yu, **R. Chen**, S.An, B. Gelfand, J. Yao, "Computational Modeling and Quantification of Wall Shear Stress in Human Choriocapillaries-A Preliminary Study", CTSI 2016 Annual Meeting, Sep. 2016
2. **R. Chen** , H. Yu, L. Zhu, T. Lee, and R.M. Patil, "Unequality effects on the Microbubble Coalescence, IUPUI Research Day, April 2016
3. S. Zhou, Y. Cao, **R. Chen**, C. Chen, H. Yu, L. Zhu, T. Sun, "Understanding Microbubble Coalescence Using High-Speed Imaging and Lattice Boltzmann Method Simulation", IUPUI Research Day, April 2016

4. **R. Chen**, W. Diao, Y. Cheng, L. Zhu, H. Yu, “Lattice Boltzmann simulation of self-driven bubble transport in a micro-channel with a virtual check valve”, The 67th Annual APS-DFD meeting, Nov. 2014

PROFESSIONAL MEMBERSHIP

American Physical Society (APS)